Ensemble Based Quantum Memory and Adiabatic Phase Gates in Electron Spins



Hua Wu

St Anne's College

A thesis submitted for the degree of Doctor of Philosophy

at the University of Oxford

Michaelmas Term 2011

© Hua Wu

St Anne's College, 2012.

Typeset in LaTeX 2$_\varepsilon$.

Ensemble Based Quantum Memory and Adiabatic Phase Gates in Electron Spins

Hua Wu

St Anne's College

Michaelmas Term 2011

Abstract of a thesis submitted for the degree of Doctor of Philosophy

Quantum computing has been a new and challenging area of research since the concept was put forward in 1980s. A quantum computer is a computer that processes information encoded in systems that exhibit quantum properties and is proved in theory to be more powerful than classical computers. Various approaches to the implementation of the quantum computers have been studied over the decades, each of them having their own advantages and disadvantages in terms of the lifetime of the quantum information, processing time, and scalability of the implementation. Proposals for hybrid quantum processors are interesting because they benefit from the advantages of each comprising system, and thus providing a promising approach to a practical quantum computer.

In this thesis, I demonstrate experimentally the principle of utilizing electron spin ensembles as a quantum memory for hybrid quantum processors. I demonstrate the storage and on-demand retrieval of multiple bits of quantum information into and from a single electron spin ensemble by applying magnetic field gradient pulses. I then study the coupling between an electron spin ensemble and a three-dimensional microwave cavity, in the aim of discussing the condition for the coherent information transfer between the excitations in solid-state matter and photons. As an alternative to the high power pulses in electron paramagnetic resonance (EPR), I study the possibility of controlling the electron spin states via adiabatic processes. I demonstrate the implementation of adiabatic geometric phase gates in electron spins and compare their performances to other phase gates achieved with microwave pulses in both simulation and experiment, verifying the robustness of the adiabatic gates against certain type of noises. Finally I present the simulation method developed for simulating the pulsed EPR experiments in this thesis, using a model more general than some currently-existing simulation packages.

Acknowledgements

First and foremost, I would like to thank all my supervisors, Dr. John Morton, Dr. Arzhang Ardavan and Prof. Andrew Briggs. I am most grateful to John for his wealth of ideas and guidance in the experiments, to Arzhang for the discussions and instructions through clearly explained concepts of physics, and to Andrew for the inspirational discussions and the encouragements.

I would also like to thank Dr. Richard George for sharing his rich experience and helping me solve many practical problems in the experiments; Dr. Eisuke Abe for teaching me useful skills in low temperature experiments and for his very dedicated work during our collaboration; Dr. Erik Gauger and Dr. Mikko Möttönen for the very helpful discussions on the theory of adiabatic phase gate as well as the advices on the experiment; Miss Stephanie Simmons for her help in the instrumentation of the experiment of the adiabatic phase gate; Dr. Janus Wesenberg for the discussions helping me understand some theoretical problems on the multimode memory; Dr. Yasuhiro Ito for the help in the electrochemical preparation of the LiPc sample; and many engineers and technicians in the Central Electronics group and Mechanical group of the Department of Physics without whose help my experiments would have been impossible. I would also like to thank all the members of the QSD group, who have been a great inspiration for me through the three years, a source of good advice as well as collaboration.

I would like to thank all the friends that make my time in Oxford enjoyable. I appreciate

very much the companionship of Miss Rong Hu, her high spirits and good humor have always been the most delightful. Miss Juan Liu, Mr. Yimin Wu, Mr. Guoquan Liu and many others have also given me great joy over the time.

In regards to the funding for my DPhil study, I thank the K. C. Wong Education Foundation for the full sponsorship over the three years. I also thank the Hitachi Cambridge Laboratory for the additional support on the living expense. Also many thanks to St Anne's College for providing the travel fund to support my attendance at academic conferences.

Lastly, I thank my parents for their love and encouragements. Their support has been the most important to the accomplishment of this thesis.

Contents

Acknowledgements **v**

1 Introduction **1**

1.1 Quantum information processing (QIP) 2

1.2 Physical implementation of QIP 3

1.2.1 DiVincenzo Criteria for qubit 3

1.2.2 Implementations for quantum computing 4

1.3 Light-matter quantum interface 5

1.3.1 Single atoms 6

1.3.2 Atomic ensembles 8

Raman and EIT approaches 8

Photon echo approach (CRIB and AFC) 13

1.4 Hybrid quantum computing 19

1.4.1 Progress in circuit QED 19

1.4.2 Hybrid quantum processor 20

2 Electron paramagnetic resonance **23**

2.1 Electron spin qubits 24

2.2 Pauli matrices 25

2.3 Spin Hamiltonian 27
2.4 Dynamics of the spin system 28
2.5 Rotating frame 29
2.6 Relaxation processes 30
2.7 Microwave pulses 32

3 Multimode memory in electron spin ensembles 35
3.1 Model for multimode storage 36
3.1.1 Collective state 36
3.1.2 Collective coupling and Hamiltonian 37
3.1.3 Collective mode 38
3.2 Holographic storage using magnetic field gradient 39
3.2.1 Magnetic field gradient 39
3.2.2 Collective phase mode 41
3.2.3 k-Space and holographic quantum memory 42
3.3 Characterizing field gradient coil 43
3.3.1 Experimental characterization 45
3.3.2 Creating orthogonal k-modes 46
3.4 Storage of microwave pulses in electron spins 48
3.4.1 Storage of single microwave pulses 49
3.4.2 Storage of multiple microwave pulses 52
3.4.3 Crosstalk between stored microwave pulses 55
3.4.4 Capacity of the multimode memory 60
3.5 Collective coherence transfer to nuclear spins 64
3.6 Conclusions 67

4 Coupling electron spins to a microwave cavity 69
4.1 Interaction between electron spins and photons 70
4.1.1 Kramers-Kronig relation 70

4.1.2 Vacuum Rabi splitting . . . 71
4.1.3 Collective enhancement . . . 72
4.2 Spins and cavities . . . 73
4.2.1 Electron spin ensembles . . . 74
4.2.2 Microwave cavities . . . 76
4.3 Weak coupling . . . 76
4.4 Strong coupling . . . 78
4.4.1 Observation of an anticrossing . . . 78
4.4.2 $\sqrt{N}$-dependence of collective coupling . . . 79
4.4.3 Effect of cavity volume . . . 81
4.4.4 Effect of microwave power . . . 83
4.5 Condition for observing anticrossing . . . 84
4.6 Conclusions . . . 86

5 Adiabatic geometric phase gates 87
5.1 Model . . . 88
5.1.1 Geometric phase . . . 88
5.1.2 Hamiltonian in the rotating frame . . . 90
5.1.3 Driving microwave field . . . 91
5.1.4 Adiabatic conditions . . . 94
5.2 Numerical simulations . . . 95
5.2.1 Continuity of the driving field . . . 96
5.2.2 Inhomogeneities in microwave field . . . 97
5.2.3 Fast fluctuations in static field . . . 98
5.2.4 Comparison with phase gates using dynamic pulses . . . 99
5.3 Experimental demonstration . . . 103
5.3.1 Implementation of adiabatic geometric phase gate . . . 103
5.3.2 Exploring various parameters . . . 106

5.3.3 Comparison with dynamic phase gates . . . 111
5.3.4 Comparison with geometric phase gates with dynamic pulses . . . 113
5.4 Conclusions . . . 114

6 Simulation of pulsed EPR experiments 117
6.1 Motivation for a new simulation toolbox . . . 118
6.2 Realization . . . 119
6.2.1 Pauli matrices for coupled spins . . . 119
6.2.2 Hamiltonians and pulses . . . 120
6.2.3 Time evolution . . . 121
6.2.4 Spin packets and inhomogeneities . . . 123
6.2.5 Measurement of transients . . . 123
6.3 Examples of application . . . 124
6.3.1 Storage of two microwave pulses . . . 124
6.3.2 Adiabatic geometric phase gate . . . 124
6.3.3 Strongly driven two-level system . . . 126
6.4 Prospects . . . 127

7 Conclusions 129

References 133

1

Introduction

The computer has made great impacts on the development of the modern world ever since its invention. To achieve higher computing efficiency, the volume of the computing processor has decreased from the magnitude of meter to below the order of a micrometer. Moore's Law, put forward by Gordon Moore in 1965, said that the number of the transistors integrated on the chip processor would double in every 18 months while its cost would halve, and this has largely held true until now. Over decades of development, as the number of transistors in integrated circuits has increased, the volume of each transistor has rapidly decreased. When the volume of the transistor approaches the order of nanometer, its working principles become dominated by the effect of quantum mechanics instead of the original classical mechanics. At the same time, people started to seek the possibility of utilizing quantum mechanics in building a new generation of information processors. The concept of **quantum computer** was thus born as a computer working according to the principles of quantum mechanics.

1.1 Quantum information processing (QIP)

In the early 1980s, Benioff [Ben80] first proposed the concept of quantum computing and put forward a design of an executable quantum computer that had a counterpart in classical Turing machines. Shortly after this, Feynman [Fey82] developed the design of Benioff and proposed that a quantum computer could be used to simulate other quantum systems. In 1985, Deutsch [Deu85] proposed a model of quantum computing based on quantum interference, and introduced the idea of a quantum logic gate. He also discussed the generalization of the quantum computer, as well as the generation and correction of errors. However, from the mid 1980s until the early 1990s, the concept of quantum computing had attracted only limited interest, firstly because all the models of quantum computer that had been put forward by then required isolated systems, independent from their environment. In any real physical systems there are many limiting factors from the environment that must be considered and affect the performance of the quantum computer, such as quantum decoherence, thermal noise, etc. In addition, at that time there were only limited algorithms to show

how a quantum computer would be superior to conventional computers in solving certain mathematical problems.

In mid 1990s the appearance of two famous quantum algorithms changed this situation. In 1994, Shor proposed what is now known as the Shor quantum algorithm [Sho94] which is very efficient at factorizing large numbers into their constituent prime numbers. In classical computation, the time complexity for factorizing a number of N digits increases exponentially with N, while in Shor's algorithm the time complexity increases polynomially with $O(N^3)$. In 1996, Grover [Gro96, Gro97] put forward a quantum algorithm for database search which reduced the time complexity of searching a random database of size N from the original $O(N)$ in classical algorithm to $O(\sqrt{N})$. These quantum algorithms showed that a quantum computer does have higher computing efficiency in solving certain mathematical problems. Stimulated by the developments in quantum algorithms, many other scientists around the world have joined in the research in quantum computing. The field of quantum information processing (QIP) has developed greatly ever since.

1.2 Physical implementation of QIP

1.2.1 DiVincenzo Criteria for qubit

Analogous to classical information processing, the basic unit of quantum information is the quantum bit — *qubit*. The physical realization of a qubit is one of the central subjects in the QIP research. DiVincenzo [DiV00] put forward a list of requirements for a physical system to be a possible realization of a qubit, which were later named the *DiVincenzo criteria*:

1. A scalable system with well characterized qubits;

2. The ability to initialize the state of the qubits;

3. Long relevant decoherence times, much longer than the gate operation time;

4. A universal set of quantum gates;

5. A qubit-specific measurement capability.

Two supplementary criteria, known as *DiVincenzo desiderata*, were added to the list regarding the transmission of quantum information:

6. The ability to interconvert stationary and flying qubits;

7. The ability to faithfully transmit flying qubits between specified locations.

Here, the flying qubits usually mean photons that travel through channels or free space carrying information in its polarization, phase, or other degree of freedom, and the stationary qubits usually mean matter systems that have a specified location and are capable of reliable local computation. Therefore the two additional criteria actually raise the requirements for the interface between light and matter for possible implementations of QIP.

Today, qubits have been proposed and experimentally realized in many different physical systems, including nuclear spin [Cor97, Jon01, Kan98], electron spin [Los98, Har02], photon polarization [Chu95, DAr00], electronic configuration of trapped ions [Cir95], superconducting qubits [Mak01, Cla08], etc. Each of these candidates has its own advantages and disadvantages. For example, the nuclear spin has a long lifetime which favours the storage of the quantum state, but it also has fairly weak interactions between different spins; electron spin, another promising candidate, has a shorter lifetime than the nuclear spin, as well as stronger coupling to the environment which makes the qubit operations faster and easier.

1.2.2 Implementations for quantum computing

As predited by Lloyd [Llo93], many different physical systems could be used to realize qubits, and it is possible to overcome the problems brought by quantum decoherence and noise by error correction. Many different schemes for quantum computing have proposed and tested based on the various qubit systems mentioned above.

Some of the examples are: cold atoms trapped in an optical cavity [Cir95, Mon95], which is based on the interaction between the optical field inside the cavity and the cold atom;

NMR-based [Ger97] or electron spin based [Vri00] quantum computing with materials such as fullerenes [Har02] or spin implanted silicon [Kan98, Vri00]; quantum computing schemes based solely on linear optical elements [Kni01, OBr03]; quantum gate operations and algorithms realized with superconducting circuits [Yam03, Pla07], etc. Although the difficulties associated with the detection of single qubits can be avoided by using bulk materials (or ensembles), there arises the question of initializing the system into a highly pure state and the possible reduction of the lifetime due to the inhomogeneity within the ensemble. All kinds of physical realizations of quantum computer must compromise between two restraints: a strong interaction between qubits and the environment, and a long decoherence time.

1.3 Light-matter quantum interface

Among the different physical qubit systems mentioned in Sec.1.2.1, photons have the highest travelling speed, and are very robust in the sense that they usually have weak interactions with the environment. However, these properties also mean that they are difficult to localize and store. An intuitive idea is to store or manipulate the qubit via the quantum states of matter, and to map those quantum states onto photons for communication or measurement. In any quantum computing scheme, part of the information, i.e. qubits, will need to be stored for a period of time and retrieved later to continue with the computation. The storage of quantum information is also necessary for long distance quantum communication and building quantum repeaters [Bri98a, San11], on whose basis a quantum network [Cir97, Kim08] can be constructed. A physical qubit system with a long decoherence time would be favorable for the storage of photon states. The spin state of atoms, for example, is one such system. Therefore, the challenge lies in developing techniques for coherently mapping quantum states of photons into atoms or any other solid-state qubit systems, and retrieving them back. Many different approaches have been proposed, either based on single absorbers or emitters in a high quality factor cavity, or utilizing optically dense atomic or molecular ensembles.

1.3.1 Single atoms

One approach to quantum memory is to store the single photon states in individual atoms. Since the development of quantum optics in 1960s, the quantum features of the light-atom interaction have been studied intensively in the field of quantum electrodynamics (QED), comprising an essential part of optical and atomic physics [Kim98, Mil05, Wal06]. In the quantum memory scheme based on cavity QED, single photons are coherently absorbed and emitted by individual atoms placed in a high Q cavity, and the interaction between the photons and atoms is enhanced by the number of reflections of the photons within the cavity. A schematic figure of the cavity system is shown in Figure 1.1. In order to study the coherent evolution of the system, it is necessary to satisfy the condition for strong coupling: $g/(\gamma, \kappa, T^{-1}) \gg 1$, where g is the rate of coherent coupling between the atoms and the optical field, γ is the rate at which the atoms radiate into the modes other than the cavity field mode, κ is the decay rate of the cavity field, T is the time of interaction between the atoms and the cavity mode [Mil05]. In particular, T is relevant only for the setups where the particles studied are possible to escape from the cavity, whereas in case of a solid-state sample T becomes infinitely long and is no longer a characterizing parameter of the setup.

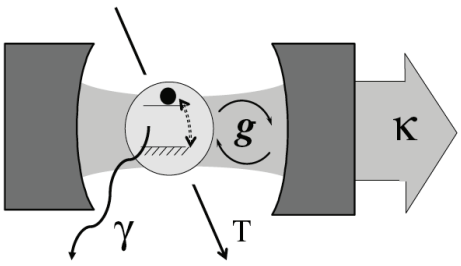

FIGURE 1.1: Characteristic parameters of the cavity QED system consisting an atom, the cavity, and environment: κ, the rate of decay of the cavity field; γ , the rate at which the atomic dipole radiates into modes other than the cavity field mode; T, the transit time of an atom through the cavity mode; and g, the rate of coherent atom-field coupling [Mil05].

There has been significant experimental progress in this area. Ye *et al.* [Ye99] realized the first experimental demonstration of trapped Cs atoms within the mode of a high finesse optical cavity in a regime of strong coupling. The observed lifetime of the single atoms

trapped within the cavity mode is 28 ms. This lifetime was later extended to 2–3 s by McKeever *et al.* [McK03] by using far off-resonance trap. Based on the atom-light interaction, Hood *et al.* [Hoo00] demonstrated a scheme for the continuous measurement of the position of the atom in a cavity by recording the variations in the transmission of a probing laser, named an atom-cavity microscope. In their experiment they realized a spatial resolution of 2 μm in a time interval of 10 μs.

Alongside the progress in techniques using high finesse optical cavities, Hennrich *et al.* [Hen00] reported the first observation of stimulated Raman scattering from a Λ-type three level atom (Rb). Similar to stimulated Raman adiabatic passage (STIRAP) [Kuk89, Gau90], the scheme uses strong coupling between the atom and the cavity mode in place of a second coupling laser to stimulate photon emission, such that the emitted photons have a narrow bandwidth and a well-determined direction. Shortly afterwards, Kuhn *et al.* [Kuh02] used the same principle to demonstrate the emission of a sequence of single photons from one Cs atom, all of which have the same radiation mode. These photons are indistinguishable and hence can be used for all-optical quantum computation schemes. In addition, the photon generation process is reversible, so it is possible to map the photon state to an atom in cavity at another location, which is the key for quantum teleportation and quantum networks. This scheme was later improved by McKeever *et al.* [McK04] to increase the number of photons generated from each trapped atom to 1.4×10^4. Also, continuous single photon generation from a $^{40}Ca^+$ ion trapped in an optical cavity was demonstrated [Kel04, Pir11]. The reversible mapping of a coherent photon state to and from the hyperfine states of an atom was demonstrated in different experiments [Boo07, Wil07], and recently an average fidelity of 93% and a lifetime of 180 ms have been reported [Spe11]. Meanwhile, quantum teleportation between two distant trapped Yb^+ ions has been demonstrated [Olm09] with a fidelity of 90% over a distance of 1 m, and a probabilistic two-qubit gate was demonstrated with two trapped Yb^+ ions with a fidelity of 89% [Mau09].

The technical complexity in the implementation of the cavity potential [Bla09], as well as in building entanglement between qubits [Moe07, Lee08] have been the main challenges

that limit the scalability of quantum computing with cavity QED [Hom09].

1.3.2 Atomic ensembles

It is usually difficult to achieve strong coupling and to manipulate the state of the individual atoms confined in the small volume of the cavity. Ensembles of atoms or molecules, by contrast, present a more favorable light-matter interface thanks to the collective enhancement of the light-matter coupling strength [Kuz97, Dua00]. In this case the strong coupling condition requires only a large resonant optical depth $d \gg 1$ of the ensemble. Several different approaches have been developed for the transfer of information between light and an atomic ensemble, including protocols based on the Raman interaction in a Λ-type three-level configuration [Koz00, Dua01], electromagnetically induced transparency (EIT) [Har97, Luk00], quantum non-demolition (QND) interaction [Ham04], and photon echo techniques [Moi01, Kra06].

Raman and EIT approaches

Both Raman and EIT [Luk01, Luk03] processes are realized in three-level configuration of atoms and the difference lies in that in the Raman scheme the signal field and the control field are off-resonant with the atomic energy levels whereas in EIT the two fields are on resonance. Figure 1.2 shows a generic Λ-type structure for light-matter coupling using three-level atoms and detuned lasers, and there are other two variations, ladder-type and V-type level structures, which are less used for EIT applications. As shown in Figure 1.2, the two states $|1\rangle$ and $|2\rangle$ of lower energy can be chosen as the spin states of the atom that have a long lifetime, and the state $|3\rangle$ of higher energy can be chosen as an electronically excited state. The probe field of frequency ω_p is coupled with the $|1\rangle - |3\rangle$ transition and is also usually named as the signal field, whereas the control field of frequency ω_c is coupled with the $|2\rangle - |3\rangle$ transition.

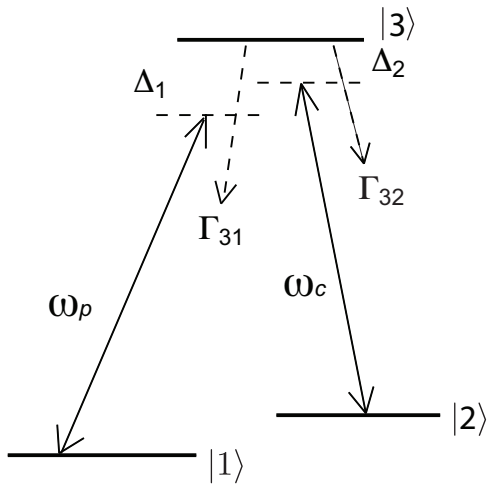

Figure 1.2: Generic system for EIT: Λ-type scheme with probe field of frequency ω_p and coupling field of frequency ω_c. $\Delta_1 = \omega_{31} - \omega_p$ and $\Delta_2 = \omega_{32} - \omega_c$ denote field detunings from atomic resonances, and Γ_{ik} denote the radiative decay rates from state $|i\rangle$ to state $|k\rangle$ [Fle05].

EIT approach

For the on-resonant EIT, the detunings Δ_1, Δ_2 as defined in Figure 1.2 are zero. The combined effect of the two resonant fields is to establish a destructive quantum interference between the two transitions $|1\rangle - |3\rangle$ and $|2\rangle - |3\rangle$, such that there is no population in the excited state $|3\rangle$. The quantum state of the atom is then a "dark" superposition of the state $|1\rangle$ and $|2\rangle$, called a *dark state* [Har97, Fle00]. Since the allowed transition ($|1\rangle - |2\rangle$ transition) is decoupled with the signal field, there will be no absorption of the incoming signal, and a peak will appear at $\Delta = 0$ in the transmission spectrum of the signal field. This is the principle of EIT. The group velocity of the signal field in the atomic ensemble is shown to be [Har92]

$$v_g = \frac{c}{1 + g^2 N/|\Omega|^2}, \tag{1.1}$$

where g is the coupling constant between a single atom and the signal field, N is the number of the atoms in the ensemble, Ω is the Rabi frequency of the control field. v_g can be much smaller than the group velocity of the signal field in vacuum c when the atomic density is high and the intensity of the control field is low.

After the signal field enters the medium, the photon-atom interaction will create a coupled excitation of light and atoms, and the combined system of photon state and atomic coherence is called a *dark state polariton* [Luk00, Fle00]. The photonic component of the dark state polariton will reduce to zero when the control field is turned off ($\Omega \to 0$), and the group velocity of the polariton will be zero. The state of the polariton will only have the matter component, which means that the photon state is transferred to an atomic coherence between the two atomic spin states, creating a single collective excitation in the atomic ensemble [Mol99, Luk01]. During this process, the length of the signal pulse is compressed because the edge of the pulse that first enters the medium will be slowed down while the rest of the pulse still propagates at the original velocity. The reverse process is realized by turning on the control field and reaccelerating the stopped dark state polariton.

If the turning off and on of the control field are carried out in an adiabatic process [Kuk89, Gau90], the state transfer between the atomic ensemble and the photon will be coherent [Fle05]. The adiabatic condition is met as long as the medium has large optical density, i.e. a large number of atoms interact with the photon, and the quantum state transfer will be efficient and robust. From another point of view, this also explains the collective enhancement: the coupling between the atomic ensemble and the photons increases with the total number of the atoms N.

When the quantum state of a photon is transferred to an ensemble of atoms, it is impossible to determine which particular atom will have its spin state flipped as each atom in the ensemble has the same probability of absorbing the photon. In other words, the excitation of the atomic ensemble is delocalized over the whole ensemble. Assuming that the initial state of the ensemble is the ground state

$$|g\rangle = |g_1 g_2 \dots g_N\rangle, \tag{1.2}$$

After the interaction with the photon, the ensemble will be in a symmetric collective state with single excitation

$$|e\rangle_1 = \sum_{i=1}^{N} \frac{1}{\sqrt{N}} |g_1 \dots s_i \dots g_N\rangle. \tag{1.3}$$

This type of multi-particle state is also named as W state [Dur00]. It is robust against decoherence and particle loss.

Early experiments in EIT demonstrated the slowing down [Kas95, Xia95, Hau99, Kas99, Bud99] and trapping [Liu01, Phi01, Koc01] of light pulses in both cold atomic gases and warm atomic vapors. In the experiment by Hau *et al.* [Hau99], the light speed was slowed down to 17 m/s in an ultracold Na atom gas; similar slow light speed was also realized in a warm Rb vapor [Kas99, Bud99]. Liu *et al.* [Liu01] demonstrated for the first time the complete trapping of a weak light pulse in a cold Na atom gas, with a trapping interval of up to 1 ms. Meanwhile, trapping was also demonstrated in warm Rb vapor for a duration of approximately 0.5 ms [Phi01]. In this experiment the Zeeman sublevels of an electronic ground state were used to store the coherence of the light pulse by applying an external magnetic field, coupled to an electronically excited state. The coherence properties of the storage process was also studied by Mair *et al.* [Mai02]. They applied a pulsed magnetic field during the storage interval to control the phase evolution of the excitation stored in the Zeeman coherence of the Rb atoms, and then observed the corresponding phase change in the retrieved light pulse. The EIT effect and trapping of light pulse were also demonstrated in solid materials using a rare-earth ion doped crystal (REIC) [Ham97, Tur01].

Thereafter, many experiments have demonstrated that quantum characteristics of light such as entanglement can be preserved during the storage using EIT [Kuz03, Cha05, Eis05] and a storage time of over a second has been reported in a REIC [Lon05]. The on-demand mapping of single excitations of the atomic ensemble to photons enables a source for single photon generation [Cho04, Che06, Mat06]. In addition, the angular redirection of the retrieved light pulse was shown to be controllable by imprinting a spacial phase gradient across the atomic gas [Sch09]. In the experiment by Choi *et al.* [Cho08], they demonstrated a coherent mapping of an entangled state of two photons onto two corresponding atomic ensembles, thus creating entanglement between two remote quantum memories. The storage time of this experiment is 1 μs with a retrieval efficiency of 17%, though for further application this efficiency needs to be improved [Nov07, Nov08]. This is an important step towards

quantum networks using light-matter teleportation [She06, Sim07b, Che08].

Off-resonant Raman approach

The off-resonant Raman configuration [Ray81] was considered for a quantum memory by Kozhekin *et al.* [Koz00] and further developed by Nunn *et al.* [Nun07] to realize deterministic, controllable, and unitary transfer of the temporal profile of single photons to spin polarized atomic ensembles in the adiabatic regime. It has been proposed that the off-resonance Raman scheme can be used for a spatially resolved multimode quantum memory [Sur08], and there have also been some other improved proposals [Gou09, Mis08, Ham09]. Experimental demonstrations include the first report on the storage of quantum states of light [Sch02], realization of an atomic memory for correlated photon states [Wal03], demonstration of a memory for quantum state of light with an efficiency of 70% [Jul04], and many other [Chu08, Het08b]. In more recent experiments, quantum memories for single photons with a lifetime of milliseconds were demonstrated with an ensemble of cold Rb atoms [Zha09a, Zha09b], or in a warm Cs atomic vapor at room temperature [Rei10, Rei11].

Another important application of the non-linearity of Raman scattering is in creating entanglement between remote atomic ensembles with the aim of long-distance quantum communication. The DLCZ-proposal [Dua01] is a widely studied proposal for a quantum repeater based on this principle. The entanglement of the two ensembles is generated by interfering the Stokes photons from both ensembles at the beam splitter and then performing single photon detection at two separate detectors. This process of entanglement generation is probabilistic. There have been many subsequent improvements in the proposal [Zha07, Che07, Sim07a] and experimental demonstrations [Cho05, Cho07]. Heralded storage of photon polarization states based on spontaneous Raman scattering has been achieved [Tan09], where a photon with arbitrary polarization is stored in the form of a superposition of the single collective excitation of two atomic ensembles. The stored polarization states are retrieved later with fidelity of 90% for a storage time of approximately 0.5 μs. The heralded quantum memory has the advantage that the detection of the heralding photon can announce the success of

the storage without necessarily revealing or destroying the stored quantum state [Lau09].

Photon echo approach

The photon echo technique [Abe66] has been used to store classical light pulses since 1980s [Mos82, Mit92]. Later it was shown that a light pulse absorbed by an atomic ensemble can preserve its quantum mechanical properties [Hal99]. Therefore, by applying this technique it is possible to build a quantum memory for QIP.

The key to this approach is to use an ensemble of atoms that have inhomogeneously broadened absorbing frequencies. In order that the medium could be used as a quantum memory, the storage time of the light pulse, which is limited by the coherence time of the optical transition, must exceed the duration of the light pulse itself. In other words, the bandwidth of the coherent interaction must be narrower than the bandwidth of the light pulse, which will prevent the light pulse from being entirely stored in the medium. However, if the medium contains an ensemble of atoms with inhomogeneous broadening, the light pulse will be entirely stored in the ensemble because different frequency components of the light pulse can be stored in different sub-groups of the ensemble. The dephasing between different frequency components of the light pulse caused by the inhomogeneous broadening is then corrected by a photon echo which reverses the inhomogeneous broadening. The application of the photon echo also provides a way to control the timing of retrieving the stored light pulse.

The process of the photon echo approach can be understood intuitively by imagining each component of the light pulse to have a frequency ω_i. After the broadened optical transition, the optical coherence from each sub-group of the atomic ensemble will precess at its own frequency ω_i. These different precession frequencies cause the dephasing of the atomic polarization. The interference of the radiations from different sub-groups of the ensemble becomes destructive, so that there is no radiation of the optical polarization. At this stage, the light pulse is stored in the atomic ensemble. To retrieve it, the simplest way is to apply a strong π pulse, which reverses the phase of the optical coherence by inverting

the population of the ground state and excited state, so that the optical coherence from each sub-group of the ensemble will refocus in the following precession. After the same period of time the atomic polarization will be in phase again and cause the emission of a photon echo.

Controlled reversible inhomogeneous broadening (CRIB)

A modified version of the photon echo technique, called controlled reversible inhomogeneous broadening (CRIB) was put forward by Moiseev and Kröll [Moi01]. They used a three-level configuration (Λ configuration, shown in Figure 1.3 (a)) of the atoms. Here the state $|s\rangle$ is a metastable state which has a long decoherence time, and the transitions between state $|g\rangle - |e\rangle$ and $|s\rangle - |e\rangle$ are allowed electric dipole transitions. The $|g\rangle - |e\rangle$ transition is broadened by the Stark shift produced by an applied electric field. As shown in Figure 1.3 (b), the atoms are initialized into the ground state $|g\rangle$, then a light pulse of a single photon in resonance with the $|g\rangle - |e\rangle$ transition is incident along the extension of the medium and is absorbed by the atoms. After a delay τ (shorter than the relaxation time of the $|g\rangle - |e\rangle$ transition) a π pulse is applied along the same direction (forward) to transfer the population from the excited state $|e\rangle$ into the metastable state $|s\rangle$ where the excitation can be stored for a longer time. After a storage time T a second π pulse is applied in the opposite (backward) direction which transfers the population back from state $|s\rangle$ to state $|e\rangle$. During the following evolution time τ the atomic coherence will rephase, thus the excitation will be retrieved at $T + 2\tau$ after the input of the single photon light pulse. The reemitted echo signal has a reversed temporal profile because the retrieving π pulse was travelling in the backward direction.

Apart from an atomic gas, a scheme using paramagnetic ions doped in dielectric crystals was also proposed later for quantum memory using CRIB [Moi03]. REIC has been commonly used for classical photon echoes. In this new proposal, the impurity ions have a twofold degenerate ground state which is lifted by an external magnetic field, thus forming a Λ system. The interactions between the impurity ions and environmental host atoms determine the resonant frequency of the impurity ions and therefore generate inhomogeneous broadening.

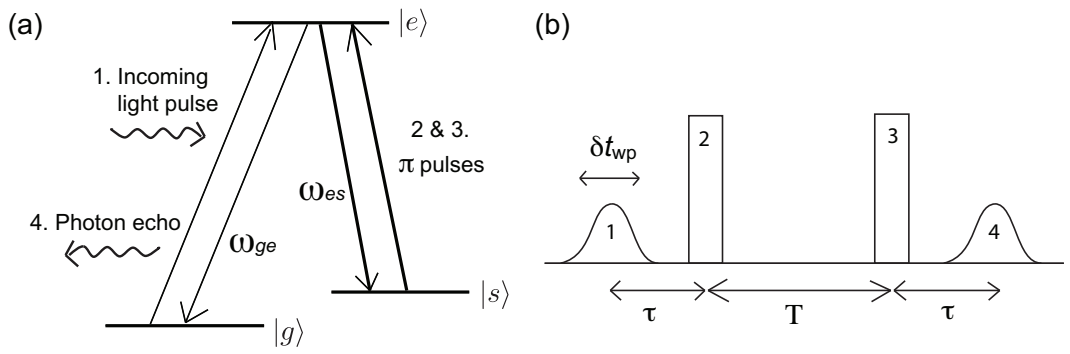

Figure 1.3: (a) Energy level diagram of the λ structure. (b) Signal and control pulse sequence for the quantum memory scheme using CRIB [Nil05].

The rephasing is achieved by applying a radio-frequency π pulse inverting the state of the crystal atoms and the sign of the level shift induced by the interatomic interactions.

The scheme of photon echo with CRIB was further developed by Kraus *et al.* [Kra06]. Instead of utilizing some natural, randomly distributed level shift of the medium particles (e.g. the interatomic interactions for the impurity ions in REIC, or the Doppler broadening of the atoms in the atom gas), they proposed to use an external field to induce artificial broadening of the intrinsic absorption line. The principle of this scheme is based on the time-reversal symmetry of the optical Bloch equations that describe the storage and retrieval of the quantum state of the light pulse. Depending on the interactions between the medium and the external field gradient, the controlled reversible broadening can be implemented with either the Zeeman shift (magnetic field gradient) or Stark shift (electric field gradient) which leads to a position-dependent detuning. The rephasing process is achieved by reversing the external field thus reversing the detuning. The resulting photon echo is called a gradient photon echo or a Stark echo which is analogous to the echoes obtained in field gradient NMR.

The efficiencies of different quantum memory schemes with CRIB have also been studied [Lon08, San07, Moi08]. In the case of the two-level systems where the broadening of the absorption line does not correlate with the spatial position of the atoms along the optical path, this type of inhomogeneous broadening is also named as transverse broadening [Lon08].

The problem with transverse broadening is that its efficiency is limited by the re-absorption of the Stark echo propagating forwards through the medium. In order to have a strong absorption of the input light pulse, the medium needs a high optical density. However, this means that the reemitted echo will also be partially re-absorbed as it propagates through the medium. Sangouard *et al.* [San07] has analyzed theoretically the efficiency of this scheme and showed that an upper bound of 54% could be achieved. The problem of re-absorption can be avoided by using so-called longitudinal broadening [Moi08], where the broadening is correlated with the position of the atoms along the optical path. In this case, the efficiency of the recalled echo can potentially reach 100% [Ale06, Sta07b] if all the decoherences are negligible in the whole process. Another way to avoid re-absorption is to use three-level systems (Λ-type system for example) for the memory medium [Moi01, Nil05]. This involves optically coupling two hyperfine ground states to one excited state where the quantum state of the light pulse is stored in one of the hyperfine ground states. When the phase matching condition is achieved the recalled echo is a time-reversal of the input light pulse and therefore undergoes no re-absorption [Ale07].

A universal approach to optimize the light storage in three-level type media was proposed by Gorshkov *et al.* [Gor07a]. Using this universal optimal approach, different schemes for light storage including EIT, Raman and photon echo approaches can have the same maximum efficiency. In their following theoretical and numerical comparisons between different light storage schemes, they found that in the case of single mode storage, the CRIB approach has few advantages compared to other storage schemes with optimal control [Gor07b, Gor08]. However, the CRIB approach has been shown to be beneficial for multimode quantum memory by Nunn *et al.* [Nun08]. The capacity of the multimode memory based on CRIB scales linearly with the optical depth d, $N \sim d$, while in the case of standard EIT and Raman memory protocols where homogeneous broadened media are used, the capacity of the multimode memory exhibits only a square-root scaling with the optical depth, $N \sim \sqrt{d}$.

In 2005 Nilsson and Kröll [Nil05] suggested a possible implementation of CRIB using REIC and gave a detailed example of the implementation in Pr^{3+}:Y_2SiO_5. They proposed

to use an electric field gradient to generate inhomogeneous broadening associated with the spatial distribution of the impurity ions. By switching the polarity of the gradient at a certain time τ after the light pulse is incident, the rephasing can be realized and after another time interval τ the stored light pulse will be reemitted. The first experimental demonstration of photon echoes with CRIB was carried out in Eu^{3+}:Y_2SiO_5 using its two-level configuration [Ale06], where they showed the storage of optical pulses of 3 μs long for a duration up to 40 μs. The inhomogeneous broadening and rephasing are realized by applying an controllable external electric field gradient. Later, the storage of light pulses of arbitrary waveform was demonstrated, and the storage of multiple pulses in time sequence was shown to be possible [Ale07]. In an experiment by Hétet *et al.* [Het08a], they demonstrated a scheme of electro-optic quantum memory for light using a linear Stark shift. The advantage of the electro-optic approach is that it does not require auxiliary optical pulses for the imprint and recall process and therefore can avoid the errors brought by these optical pulses. Lately, CRIB at the single photon level has been demonstrated in Er^{3+}:Y_2SiO_5 at telecommunication wavelength [Lau10], which shows the potential usage of CRIB in building a quantum network.

Meanwhile, Staudt *et al.* [Sta07b, Sta07a] demonstrated the storage of more than one classical coherent pulse representing time-bin qubits in Er^{3+}:$LiNbO_3$ using the three-pulse echo. This showed the prospect of storing multiple time-bin qubits in the CRIB based quantum memory.

Atomic frequency comb (AFC)

More recently, a new scheme of the photon echo approach is developed by using atomic frequency combs (AFC) [Afz09]. This scheme takes the advantage of inhomogeneous broadening of the atomic ensemble to achieve higher multimode capacity, which is shown to be independent of the optical depth. The principle of this scheme is shown in Figure 1.4. The spectrum of the optical transition $|g\rangle - |e\rangle$ is shaped into a frequency comb with a series of narrow peaks γ spanning a large frequency range Γ. The AFC has a special property that an incident single photon having a bandwidth γ_p larger than the peak separation Δ, but

narrower than the total width Γ, will be absorbed by the atoms uniformly over the photon bandwidth. This ensures the total absorption of the single photon on the condition that the atomic density is high enough at the peaks. The photon is thus stored into a collective excited state of the atoms that has different frequency components corresponding to different detunings. The evolution of these different frequency components will lead to a dephasing of the collective state, and after a time $2\pi/\Delta$ the collective state will be reestablished causing a photon echo to be emitted. Furthermore, in order to realize on-demand readout of the stored photon, a third state $|s\rangle$ can be used. After the absorption of the photon the collective excitation can be transferred to the state $|s\rangle$ by a controlling optical pulse. The readout is realized by applying a second control pulse propagating in the backward direction. $|g\rangle, |s\rangle$ can be the hyperfine or Zeeman ground states so that the storage time is extended to the spin decoherence time. The multimode capacity of AFC is shown to be only dependent on the number of peaks in the comb.

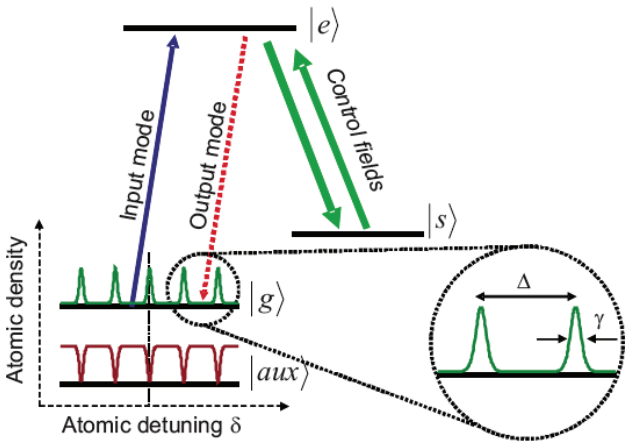

FIGURE 1.4: An inhomogeneously broadened optical transition $|g\rangle - |e\rangle$ is shaped into an AFC by frequency-selective optical pumping to the auxiliary level $|aux\rangle$. The peaks in the AFC have width γ and are separated by Δ [Afz09].

The experimental demonstrations of the AFC scheme have been realized in different REIC, including the storage of coherent light pulse at single photon level [Rie08], on-demand readout of the stored light pulses [Afz10], storage of multiple time-bin qubits in the form of temporal optical modes [Usm10]. Most recently Clausen *et al.* [Cla11] showed that the

entanglement between two photons can be preserved after the storage and retrieval from the crystal by testing the CHSH inequality. This represents an important progress towards quantum communication based on quantum repeaters of solid-state memory and linear optical devices. The use of REIC in these experiments is crucial as the impurity ions in these crystals have narrow homogeneous linewidth and a broad inhomogeneous linewidth, which is especially suitable for the AFC.

1.4 Hybrid quantum computing

1.4.1 Progress in circuit QED

Along with the progress in the research on light-matter interfaces, there have also been great developments in the techniques for QIP in solid state systems. In particular, superconducting qubits realized with Josephson junction devices [Mak01, Cla08] are of great interest for QIP because the coupling between these artificial qubits can be more easily controlled compared to other physical qubits, and each of the superconducting qubits can be designed to a set of chosen parameters, such that their quantum states can be manipulated with more flexibility.

According to the parameter by which the energy levels are defined, there are three types of superconducting qubit: flux qubit [Wal00, Fri00], charge qubit [Vio02] and phase qubit [Mar02]. Based on these systems, controllable couplings between two superconducting qubits [Ber03, Pas03] and two-qubit gates [Yam03, Pla07] have been realized. In addition, the strong coupling of the superconducting qubit to a cavity bus has been demonstrated [Wal04, Maj07], which lays the basis of circuit QED [Bla04]. Today, much progress has been made in circuit QED [Sch07, Sil07, Hof09, Wan11], and especially the implementation of two-qubit Grover and Deutsch-Jozsa quantum algorithms [DiC09] as well as the demonstration of three-qubit entanglement [Nee10, DiC10] showed the prospect of achieving scalable quantum computing with circuit QED.

The strong coupling between the photons and superconducting qubits allows the gate

operations to be carried out fast, typically in a few tens of nanoseconds [DiC09]. However, as macroscopic structures (dimension of a superconducting qubit usually as large as 100 μm), superconducting qubits suffer from short decoherence time — the longest T_1 and T_2 reported for all types of superconducting qubits are only a few microseconds [Ste10].

1.4.2 Hybrid quantum processor

The short gate time of superconducting qubits makes them favorable for realizing qubit operations and state transfer between flying and stationary qubits, but their short decoherence time limits their application in quantum state storage. On the other hand, the decoherence time of an atomic qubit can reach the range of seconds or even longer [Lad10]. Therefore, a more robust quantum system can be built by combining different physical systems that allows the interface between photons and solid-state qubits, and benefits from the advantage of both systems [Mor11].

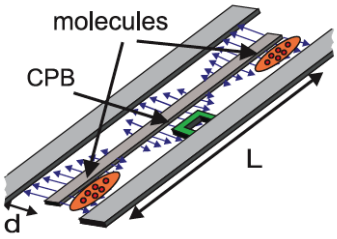

FIGURE 1.5: Schematic of a hybrid quantum computer consisting of Cooper pair boxes representing a solid state quantum processor and atomic ensemble qubits acting as long-lived quantum memories. Quantum information is shuttled between the two systems via the superconducting stripline cavity [Rab06].

Early ideas of hybrid quantum systems proposed to use a cavity bus or a transmission line to couple with two separated atoms or trapped ions [Sor04, Tia04]. It was also understood that the hybrid system composed of two drastically different systems would introduce technical questions of compatibility, for example the ion trap is realized with strong electric or magnetic fields while a strong field will normally suppress superconductivity. Later Rabl *et al.* [Rab06] proposed a more advanced model of hybrid quantum processor. Instead of single

atoms or trapped ions, they proposed to use an ensemble of polar molecules as the quantum memory, a superconducting qubit, Cooper pair box (CPB) as the operating qubit, and a stripline cavity as a quantum bus that couples to both systems (Figure 1.5). The cavity photons are stored in the hyperfine sublevels of the vibrational ground state of the molecular ensemble via Raman transition [And06], benefiting from the collective enhancement of the coherent coupling strength $g_c = g_s\sqrt{N}$, while basic one- and two-qubit operations are realized via strong coupling between the cavity and the CPB. A similar proposal was put forward for ultracold atoms trapped near the surface of a coplanar waveguide [Pet09], where the coherent state transfer between the superconducting qubit and the atomic ensemble is realized via optically excited Rydberg transitions [Pet08]. The memory time of this hybrid quantum computing scheme can be further extended by using the electron spin states of atoms or molecules for storing qubits [Wes09]. In this situation, the states of the electron spin ensemble are controlled by microwave pulses in electron paramagnetic resonance.

The large number of atoms or spins in the ensemble used for the quantum memory provides a large resource for qubit storage, as long as different qubits can be stored in a distinguishable way, i.e. into different collective states of the ensemble. These different collective states can be created in an atomic ensemble either by different two-photon Raman detunings [Bri07, Tor08a], or by different wave vectors of the control field in the Raman transition [Tor08b]; in an electron spin ensemble, they can be created by different magnetic field gradient across the sample profile [Wes09].

For the hybrid quantum processor to perform coherently, it is necessary to guarantee a strong coupling between the solid-state spin ensemble and the intermediate superconducting cavity. There have been experimental studies that demonstrate a strong coupling of the NV centers in diamond and other impurity spins in crystals to a stripline cavity at single photon level [Sch10, Kub10, Bus11]. The limiting factor for these spins is that the strains existing in the crystal will raise the inhomogeneous broadening therefore the coherence decay rate is usually quite fast, which is not ideal for quantum computing.

There are different potential source of errors in the hybrid quantum computing scheme

using electron spin ensembles. The interactions between the qubits during the storage period or during the writing (or reading) processes can be prevented if the system operates at a low temperature so that the probability of thermal excitations is low enough [Wes09]. The decoherence of the spins due to inhomogeneity of the external field can be compensated by applying a Hahn echo sequence [Hah50] or other more sophisticated dynamic decoupling (DD) sequences such as CPMG sequence [Car54, Mei58], bang-bang control [Vio99], concatenated DD sequences [Kho05] and Knill DD sequence [Sou11]. However, this raises the problem of whether the high power pulses in the DD sequences would introduce extra excitations in the spin ensembles. Meanwhile, the errors in the microwave pulses limit the performance of the DD sequences as well [Mor05b, Tyr10]. An alternative approach is to replace the microwave pulses with adiabatic passages, because adiabatic processes have been shown to be robust against errors in the microwave amplitude and high frequency noises [Chi01].

2

Electron paramagnetic resonance

Electron paramagnetic resonance (EPR) is a broadly applied technique to investigate the internal structure and spin dynamics of materials containing paramagnetic species: radicals with at least one unpaired electron. EPR spectroscopy provides information about the electronic structure as well as the geometric distribution of these species by analyzing the interactions between the species and their neighboring nuclei. Pulsed EPR, working in the same principle as traditional continuous wave (CW) EPR, has a much higher temporal and spectral resolution and can therefore provide more detailed dynamical and structural information about the material. It also provides more varieties in the design of experiments such as pulsed electron nuclear double resonance (ENDOR) or electron spin echo envelope modulation (ESEEM) to address specific problems.

2.1 Electron spin qubits

Individual unpaired electrons have a spin of 1/2. The intrinsic spin magnetic dipole moment of an electron is

$$\boldsymbol{\mu} = -g_e \mu_B \frac{\boldsymbol{S}}{\hbar}, \tag{2.1}$$

where g_e is the dimensionless *g-factor* for electron spin, $\boldsymbol{S}$ is the electron spin angular momentum, $\mu_B = \frac{e\hbar}{2m_e}$ is the Bohr magneton. When the electron spin is placed in a magnetic field $\boldsymbol{B}$, the potential energy of the system is

$$E(m_S) = \boldsymbol{\mu} \cdot \boldsymbol{B} = -g_e \mu_B m_S B, \tag{2.2}$$

with $m_S = \pm 1/2$ depending on the orientation of the electron spin magnetic dipole moment with respect to the magnetic field. The splitting between the two energy levels

$$\Delta E = E(m_S = +1/2) - E(m_S = -1/2) = -g_e \mu_B B \tag{2.3}$$

is called the *electron Zeeman splitting*. When the photons of an electromagnetic field have the same energy as the level splitting of the electron spin, i.e. $h\nu = \Delta E$, transitions between the two spin eigenstates will be induced and the electromagnetic field is called *on resonance* with the spin.

The two-level structure of an electron spin in magnetic field is a convenient physical representation of a qubit. The two spin eigenstates $|m_S = \pm 1/2\rangle$ represent the two computational basis states of the qubit $|0\rangle$ and $|1\rangle$. Any qubit that is a superposition of the two computation bases

$$|\psi\rangle = \alpha|0\rangle + \beta|1\rangle \tag{2.4}$$

can be written in the form of a spin superposition state of the two spin eigenstates

$$|\psi\rangle = \cos(\theta/2)|m_S = -1/2\rangle + \sin(\theta/2)e^{i\varphi}|m_S = +1/2\rangle. \tag{2.5}$$

The angles θ, φ are defined in Figure 2.1. The sphere in Figure 2.1 is called a *Bloch sphere*. Any point on the surface of the Bloch sphere represents a pure state of a single qubit, i.e. $|\alpha|^2 + |\beta|^2 = 1$. A mixed state is represented by a point inside the Bloch sphere.

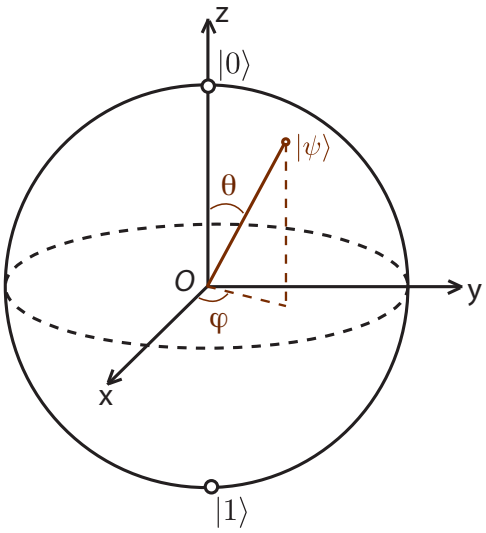

Figure 2.1: A qubit $|\psi\rangle$ represented in the Bloch sphere. The north and south poles of the Bloch sphere represent the two basis states $|0\rangle$ and $|1\rangle$ respectively.

2.2 Pauli matrices

Another representation of the state of a qubit, equivalent to the vector representation, is the *density matrix* representation. For any qubit state, the most general definition of its density

matrix is

$$\rho = \sum_j p_j |\psi_j\rangle\langle\psi_j| = \sum_j p_j \begin{pmatrix} \alpha_j\alpha_j^* & \alpha_j\beta_j^* \\ \beta_j\alpha_j^* & \beta_j\beta_j^* \end{pmatrix}, \tag{2.6}$$

where p_j is the probability of the qubit being in the pure state $|\psi_j\rangle$, and $\sum_j p_j = 1$. By this definition, the trace of ρ is always 1. Removing the 2×2 unit matrix component from ρ, the remainder can be written in the general form

$$\rho - \frac{I_2}{2} = \begin{pmatrix} x & \gamma \\ \gamma^* & -x \end{pmatrix}, \tag{2.7}$$

where $x \in \mathbb{R}, \gamma \in \mathbb{C}$. A 2×2 matrix in the form of Equation 2.7 has three degrees of freedom, and can be decomposed into the following three basis matrices:

$$\sigma_1 = \begin{pmatrix} 0 & 1 \\ 1 & 0 \end{pmatrix}, \quad \sigma_2 = \begin{pmatrix} 0 & -i \\ i & 0 \end{pmatrix}, \quad \sigma_3 = \begin{pmatrix} 1 & 0 \\ 0 & -1 \end{pmatrix}. \tag{2.8}$$

The above three matrices are the *Pauli matrices*.

Each of the three Pauli matrices is an observable along the x, y, or z axis, therefore they are also denoted as $\sigma_x, \sigma_y, \sigma_z$. By introducing a vector $\boldsymbol{\sigma} = \sigma_x\hat{x} + \sigma_y\hat{y} + \sigma_z\hat{z}$, the expectation value of the spin along any axis $\hat{n}$ can be obtained from

$$\langle \boldsymbol{\sigma} \cdot \hat{n} \rangle = \mathrm{Tr}[\rho\, \boldsymbol{\sigma} \cdot \hat{n}]. \tag{2.9}$$

Because the (transformed) Pauli matrices form a set of basis of the $SO(3)$ rotation group, any rotation operator for a spin 1/2 system in $\mathbb{R}^3$ is related to the Pauli matrices in the following way

$$R(\hat{n}) = e^{-i\frac{\theta}{2}\boldsymbol{\sigma}\cdot\hat{n}}. \tag{2.10}$$

Here $R(\hat{n})$ represents a rotation of the spin by an angle θ about axis $\hat{n}$.

2.3 Spin Hamiltonian

A spin system of multiple electron spins $\boldsymbol{S}$ and nuclear spins $\boldsymbol{I}$ is described by the complete spin Hamiltonian

$$\begin{aligned} H_0 &= H_{EZ} + H_{NZ} + H_{ZF} + H_{NQ} + H_{HF} + H_{EE} + H_{NN} \\ &= \sum_i \mu_B \boldsymbol{B}_0^{\mathrm{T}} \boldsymbol{g}_i \boldsymbol{S}_i - \sum_i \mu_{\mathrm{n}} \boldsymbol{B}_0^{\mathrm{T}} \boldsymbol{g}_{\mathrm{n},i} \boldsymbol{I}_i \\ &\quad + \sum_{\boldsymbol{S}_i > 1/2} h \boldsymbol{S}_i^{\mathrm{T}} \boldsymbol{D}_i \boldsymbol{S}_i + \sum_{\boldsymbol{I}_i > 1/2} h \boldsymbol{I}_i^{\mathrm{T}} \boldsymbol{Q}_i \boldsymbol{I}_i + \sum_{i,j} h \boldsymbol{S}_i^{\mathrm{T}} \boldsymbol{A}_{i,j} \boldsymbol{I}_j \\ &\quad + \sum_{i \neq j} h \boldsymbol{S}_i^{\mathrm{T}} \boldsymbol{J}_{i,j} \boldsymbol{S}_j + \sum_{i \neq j} h \boldsymbol{I}_i^{\mathrm{T}} \boldsymbol{J}_{\mathrm{n},(i,j)} \boldsymbol{I}_j. \end{aligned} \tag{2.11}$$

In the above equation, H_{EZ} (H_{NZ}) is the *electron* (*nuclear*) *Zeeman interaction* between the electron spins and the external magnetic field $\boldsymbol{B}_0$, $\boldsymbol{g}$ ($\boldsymbol{g}_{\mathrm{n}}$) is the tensor describing the orientation dependence of the electron (nuclear) Zeeman interaction; H_{ZF} is the *zero-field interaction* due to the strong dipole-dipole coupling between the electron spins in systems with spin $S > 1/2$ and non-cubic symmetry, $\boldsymbol{D}$ is traceless and is called the zero-field interaction or the fine structure tensor; H_{NQ} is the *nuclear quadrupole interaction* between the non-spherical charge distribution in systems with nuclear spin $I > 1/2$ and the electric field gradient caused by nearby electrons and nuclei, $\boldsymbol{Q}$ is called the nuclear quadrupole tensor; H_{HF} is the *hyperfine interaction* between an electron spin and a nuclear spin which is the combining effect of the anisotropic dipole-dipole interaction and the isotropic Fermi contact interaction, $\boldsymbol{A}$ is called the hyperfine tensor; H_{EE} (H_{NN}) is the *electron* (*nuclear*) *spin-spin interaction* describing the dipole-dipole interaction between two different electron (nuclear) spins, $\boldsymbol{J}$ ($\boldsymbol{J}_{\mathrm{n}}$) is called the electron (nuclear) dipole-dipole tensor.

In most situations H_{NZ}, H_{NQ} and H_{NN} are too weak to be observed directly in EPR spectra, whereas they are usually observed in nuclear frequency spectra measured in ESEEM and ENDOR experiments.

2.4 Dynamics of the spin system

An external electromagnetic field applied on resonance (or near resonance) with two levels can induce the corresponding (allowed) transition. The time-dependent Hamiltonian describing the interaction between the applied field and the spins is

$$\begin{aligned} H_1(t) &= H_1^{(\boldsymbol{S})}(t) + H_1^{(\boldsymbol{I})}(t) \\ &= \mu_B \boldsymbol{B}_{\mathrm{mw}}^{\mathrm{T}}(t)\boldsymbol{g}\boldsymbol{S} - \mu_n \boldsymbol{B}_{\mathrm{rf}}^{\mathrm{T}}(t)\boldsymbol{g}_{\mathrm{n}}\boldsymbol{I}, \end{aligned} \tag{2.12}$$

where $\boldsymbol{B}_{\mathrm{mw}}(t)$ is the microwave field coupled with the electron spin, $\boldsymbol{B}_{\mathrm{rf}}(t)$ is the radiofrequency field coupled with the nuclear spin. As the amplitude of $\boldsymbol{B}_{\mathrm{mw}}(t)$ and $\boldsymbol{B}_{\mathrm{rf}}(t)$ is usually small compared to the external static field $\boldsymbol{B}_0$, H_1 is usually considered as a perturbation of the spin Hamiltonian H_0 in Equation 2.11.

The time evolution of the spin system under the total Hamiltonian $H(t) = H_0 + H_1(t)$ is described by the *Schrödinger equation*

$$\frac{d}{dt}|\psi(t)\rangle = \frac{-i}{\hbar} H|\psi(t)\rangle, \tag{2.13}$$

where $|\psi(t)\rangle$ is the wave function describing the quantum state of the spin system.

In the density operator formalism, considering only the coherent dynamics and neglecting any relaxation will result in a unitary and deterministic evolution of the spin system, which can be described by the *von Neumann equation*:

$$\frac{d}{dt}\rho(t) = \frac{-i}{\hbar}[H(t), \rho(t)]. \tag{2.14}$$

The time integral of the above equation is complicated when the Hamiltonian $H(t)$ is explicitly time-dependent. In this case the time evolution propagator is defined as

$$U(t) = \mathcal{T}\exp\Big\{-\frac{i}{\hbar}\int_0^t H(t')\ dt'\Big\}, \tag{2.15}$$

where $\mathcal{T}$ is called the time-ordering operator. Therefore the time evolution of the density operator of the system can be formally written as

$$\rho(t) = U(t)\rho(0)U^{\dagger}(t). \tag{2.16}$$

In a more general picture, relaxation process needs to be considered to give a complete description of the dynamics of the spin system. Generally, the relaxation can be modelled by a time-homogeneous Markovian process, i.e. the relaxation rates are considered as time-independent and that system is considered as memoryless. Thus the non-unitary, stochastic evolution of an open system is described by the *Lindblad equation*

$$\frac{d}{dt}\rho(t) = \frac{-i}{\hbar}[H(t), \rho(t)] + \sum_k \big[L_k \rho(t) L_k^\dagger - \frac{1}{2}\big\{\rho(t), L_k^\dagger L_k\big\}\big], \tag{2.17}$$

where L_k are Lindblad operators, $\{A, B\}$ is the anti-commutator. The right hand side of the above equation is a linear functional of $\rho(t)$, defined as the *Lindblad superoperator* $\mathcal{L}[\rho(t)]$. If the Lindblad operators are all zero, the above equation goes back to the von Neumann equation and $H(t)$ is the Hamiltonian of the closed system.

2.5 Rotating frame

An electron spin with magnetic dipole moment $\boldsymbol{\mu}$ placed in a magnetic field $\boldsymbol{B}_0$ will experience a Hamiltonian

$$H_0 = -\boldsymbol{\mu} \cdot \boldsymbol{B}_0 = \gamma \boldsymbol{S} \cdot \boldsymbol{B}_0, \tag{2.18}$$

where $\gamma = g_e|e|/2m_e = g_e\mu_B/\hbar$ is the gyromagnetic ratio for an isolated electron. For a time-independent magnetic field along the z-axis, i.e. $\boldsymbol{B}_0 = B_0\hat{z}$, the time-evolution operator will be

$$U_0(t) = e^{i\frac{\gamma\sigma_z B_0}{2}t} = \begin{pmatrix} e^{i\omega_0 t/2} & 0 \\ 0 & e^{-i\omega_0 t/2} \end{pmatrix}, \tag{2.19}$$

where $\omega_0 = \gamma B_0$. This implies that the electron spin will *precess* at a frequency ω_0 about the z-axis, the direction of the static magnetic field.

When another weak magnetic field with an angular frequency ω and amplitude B_1 in the xy plane is added to the static field B_0, according to Equation 2.12, the total Hamiltonian will be

$$H = -\gamma\frac{\hbar}{2}(B_0\sigma_z + 2B_1\cos\omega t\sigma_x). \tag{2.20}$$

Here the microwave field is taken to be along the x-axis. The factor 2 in front of B_1 comes from the fact that $\boldsymbol{B}_1(t) = \boldsymbol{B}_1 e^{-i\omega t} + \boldsymbol{B}_1^* e^{i\omega t} = 2B_1 \cos\omega t \cdot \hat{x}$.

Since in most cases the frequency of the microwave field B_1 is constant, it will be convenient to transform Equation 2.20 into a *rotating frame* of reference that has the same frequency as B_1 and remove the time dependence of the Hamiltonian. Using the transformation operator

$$U(t) = e^{i\frac{\omega t}{2}\sigma_z}, \tag{2.21}$$

the new state vector in the rotating frame will be

$$|\psi_R(t)\rangle = U(t)|\psi(t)\rangle. \tag{2.22}$$

Substituting Equation 2.22 for the $|\psi(t)\rangle$ in the Schrödinger equation (Equation 2.13), we obtain

$$\frac{\partial}{\partial t}U(t)|\psi(t)\rangle = \frac{-i}{\hbar}H_R(t)U(t)|\psi(t)\rangle, \tag{2.23}$$

which gives the Hamiltonian in the rotating frame

$$\begin{aligned} H_R &= U^{-1}(t)\left(H(t) - \frac{\hbar\omega}{2}\sigma_z\right)U(t) \\ &= -\frac{\hbar}{2}\Big[(\omega_0 - \omega)\sigma_z + 2\gamma B_1\big(\frac{1-\cos 2\omega t}{2}\sigma_x + \frac{\sin 2\omega t}{2}\sigma_y\big)\Big]. \end{aligned} \tag{2.24}$$

After applying the *rotating wave approximation*, the rapidly oscillating terms $\cos 2\omega t, \sin 2\omega t$ are neglected, Equation 2.24 becomes

$$H_R = -\frac{\hbar}{2}\big(\Delta\sigma_z + \gamma B_1\sigma_x\big), \tag{2.25}$$

where $\Delta = \omega_0 - \omega$ is the detuning of the microwave field from the resonance frequency. This is the time-independent Hamiltonian in the rotating frame.

2.6 Relaxation processes

If we visualize the dynamics of the spin state by the evolution of the spin magnetization, then the relaxation processes are the processes that bring spin magnetization back to equilibrium.

In spin-lattice relaxation, the longitudinal, or z component of the spin magnetization recovers towards its thermodynamic equilibrium. The process is described by an exponential equation

$$M_z(t) = M_{z0}(1 - e^{-t/T_1}), \tag{2.26}$$

where M_{z0} is the magnetization of the spin at equilibrium, and T_1 is the *spin-lattice relaxation time*. The rate of spin-lattice relaxation is determined by the energy dissipation of the spin via the vibration or rotation of the surrounding lattice.

In the spin-spin relaxation, the transversal, or the x, y component of the spin magnetization loses its coherence in phase and decays to zero. This process is also described by an exponential equation

$$M_{xy}(t) = M_{xy}(0)e^{-t/T_2}, \tag{2.27}$$

where T_2 is often called the *spin-spin relaxation time*. T_2 is often affected by spin-spin dipolar and exchange interactions, and therefore by the concentration of the spins in the sample. This effect of T_2 on the decay of transversal magnetization is also called the *homogeneous* T_2. Another contribution to the decay of the transversal magnetization is from the inhomogeneities in B_0 (such as environmental nuclear spins), called the *inhomogeneous* T_2. The B_0 inhomogeneity induces different precession frequencies in the spin packet, which lead to a dephasing of the spin magnetizations. The combined effect of these two mechanisms is a relaxation time denoted as T_2^*,

$$\frac{1}{T_2^*} = \frac{1}{T_2} + \frac{1}{T_{2,\text{inhomo}}}. \tag{2.28}$$

T_2^* is the time constant that characterize the duration of the free induction decay (see next section).

2.7 Microwave pulses

According to Section 2.5, when the microwave field B_1 is on resonance with the spin splitting, i.e. $\omega = \omega_0$, the Hamiltonian in Equation 2.25 becomes

$$H_R = -\gamma \frac{\hbar}{2} B_1 \sigma_x. \tag{2.29}$$

In the rotating frame, this applies a rotation to the electron spin magnetization about the x-axis, and if the length of the microwave pulse is τ_p, the rotation angle will be (see Equation 2.10)

$$\theta = \gamma B_1 \tau_p. \tag{2.30}$$

Meanwhile, the phase of the microwave pulse can be varied, by which the rotation axis of the spin magnetization is determined.

In pulsed EPR, the non-zero magnetization precessing in the xy plane induces an oscillating current in the detection coil located around the sample, which gives the time-domain signal. Therefore, any microwave pulse with rotation angle $\theta \neq 0, \pi, 2\pi \cdots$ will generate a signal in EPR spectrometer.

One example of a simple time-domain signal is the *free induction decay* (FID). After a pulse of rotation angle $\pi/2$, the spin magnetization is rotated into the xy plane. As the spin-spin relaxation processes dominate the evolution, the transversal magnetization of the spins dephases along time and finally the total transversal magnetization of all spins decays to zero (Figure 2.2). The decay rate of FID is T_2^*.

As discussed in the previous section, the dephasing of the spin magnetization due to the inhomogeneity in B_0 is a major contribution to T_2^*. This dephasing, however, can be reversed if all the magnetizations are rotated by applying a π pulse along an axis in the xy plane. Suppose the π pulse is applied at a time τ after the $\pi/2$ pulse, then at the time 2τ the magnetizations will rephase and a signal called *spin echo* will be observed (Figure 2.2).

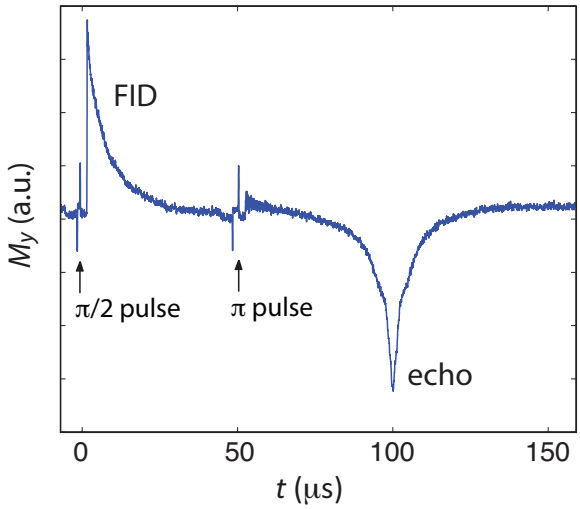

Figure 2.2: An example of time domain EPR spectrum of a Hahn echo experiment. The spectrum was measured for a N@C_{60} powder sample at 40 K.

3

Multimode memory in electron spin ensembles

In the proposed scheme of a hybrid quantum processor [Wal09, Loo10], a long-lived memory for quantum information can be achieved by storing the qubits into some physical systems with long decoherence times, such as electron spins [Wes09, Ima09], cold atoms [Nun08, Het08a, Hos09], polar molecules [Rab06, And06, Tor08a], ion-doped cystal [Ale06, Kra06, Rie08], etc. In this chapter, I describe the method and experimental realization for storing multiple microwave excitations in a single electron spin ensemble and how this constitutes a multimode random-access memory for quantum information processing.

3.1 Model for multimode storage

When the information carried by a photon is transferred into a solid-state qubit, it creates a certain type of excitation in the solid-state system. An ensemble of the same solid-state qubits therefore provides a potentially large resource for storing multiple flying qubits into a solid-state quantum memory. However, in order to make sure that all the stored qubits are not affecting each other, it is necessary to store each qubit into an independent parametric subspace of the ensemble, i.e. each qubit is stored in an orthogonal state of the ensemble. For this reason, we will need the concept of a collective state.

3.1.1 Collective state

An ensemble of N particles that have the same internal two-level structure is initially in its ground state and can be written in the following product state

$$|g\rangle_{\text{ens}} \equiv |g_1 \cdots g_N\rangle. \tag{3.1}$$

After interaction with a photon a single excitation is created in the ensemble in the form of symmetric Dicke state [Dic54]

$$|e\rangle_{\text{ens}} \equiv \frac{1}{\sqrt{N}} \sum_j |g_1 \cdots e_j \cdots g_N\rangle. \tag{3.2}$$

It is also possible to introduce a collective operator $\hat{a}^\dagger = \frac{1}{\sqrt{N}} \sum_j \hat{a}_j^\dagger$ to denote the creating operation as $|e\rangle_{\text{ens}} = \hat{a}^\dagger |g\rangle_{\text{ens}}$. When the number of the particles N in the ensemble is large enough, the collective operator will obey the commutator relation $[\hat{a}, \hat{a}^\dagger] = 1$.

3.1.2 Collective coupling and Hamiltonian

A single atom interacting with a single photon experiences a coupling between the eigenstates of the two systems, with its strength described by the vacuum Rabi frequency g_s. This coupling can be enhanced by a factor of $\sqrt{N}$ if the single atom is replaced with an ensemble of N atoms, where N is the number of atoms in the ensemble [Tav68]. Therefore, the Hamiltonian describing the interaction between an ensemble and photons in a frame rotating with the frequency of the photon ω_c is

$$\begin{aligned} \hat{H} &= \hbar \sum_j g_{s,j} (\hat{a}_j^\dagger \hat{c} + \hat{a}_j \hat{c}^\dagger) - \delta_c \hat{c}^\dagger \hat{c} \\ &\approx \hbar \sqrt{N} g (\hat{a}^\dagger \hat{c} + \hat{a} \hat{c}^\dagger) - \delta_c \hat{c}^\dagger \hat{c}, \end{aligned} \tag{3.3}$$

where $g_{s,j}$ is the coupling strength of the jth atom to the photons, $g = \sqrt{\sum_j |g_{s,j}|^2 / N}$ is defined as the average coupling strength of the ensemble of atoms, $\hat{c}, \hat{c}^\dagger$ are the annihilation and creation operator for the photons, $\delta_c = \omega_c - \omega_a$ is the detuning of the photon from the transition frequency ω_a of the atom, $\hat{a}, \hat{a}^\dagger$ are collective operators of the ensemble defined in the last section.

It can be seen that the two lowest eigenstates of the above Hamiltonian are $|g, 1\rangle$ and $|e, 0\rangle$, and these two levels can be used as the two-level system for storing qubits. When the photon number reduces from 1 to 0, a single collective excitation is created in the ensemble, and this indicates that the information embedded in the photon has been transferred — or "stored" — in the ensemble; in the reverse process where the ensemble returns to its ground state and the number of photon increases from 0 to 1, the stored information is transferred back to the photon — the process can also be called "read out".

3.1.3 Collective mode

When there is more than one qubit to store in one ensemble of atoms, it is required that each qubit is stored in different collective state of the ensemble, and the evolution of these different collective states must not create crosstalk between themselves.

As shown in Equation 3.2, when all the atoms in the ensemble have the same phase factor, it gives the symmetric Dicke state. If we can introduce an additional phase factor ϕ_j to each atom that depends on certain parameters of that atom, we will be able to create a global phase distribution over the ensemble, and the single collective excited state becomes

$$|e\rangle'_{\text{ens}} = \frac{1}{\sqrt{N}} \sum_j e^{i\phi_j} |g_1 \cdots e_j \cdots g_N\rangle. \tag{3.4}$$

We call such a single collective excited state with a specific phase distribution a *collective mode*.

If we denote the phase distribution of the ensemble with a parameter k, a single collective excited state with a certain phase distribution is then written as $|e, k\rangle$. Two different modes are orthogonal if they satisfy the following orthogonality relation

$$\langle e, k_1 | e, k_2 \rangle = 0. \tag{3.5}$$

Based on these definitions, we say that multimode storage of quantum information can be achieved by storing different qubits in different collective modes of the ensemble which are orthogonal to each other. The qubits are stored independently in the modes — they can evolve without causing any crosstalk between each other and can be addressed separately during the readout process. On the other hand, although N orthogonal collective modes can be created in an ensemble of N spins, the number of qubits that can be simultaneously stored in the ensemble is in principle limited by $\sqrt{N}$. This large storage capacity is another important advantage of the ensemble based quantum memories apart from the collective enhancement of the coupling strength.

3.2 Holographic storage using magnetic field gradient

There are different ways to introduce the phase factor ϕ_j. Typically, one way is to choose the position of the atom $\vec{r}_j$ as the parameter, and create a phase distribution that is a function of $\vec{r}_j$. This kind of collective mode is also called spatial mode [Tor08b]. Another way is to choose the transition frequency of the atom $\omega_{a,j}$ as the parameter and create a phase distribution as a function of the detuning $\delta_{c,j} = \omega_c - \omega_{a,j}$. Since in this case the phase distribution is created over time, this kind of collective mode is also called temporal mode [Afz09].

Usually the spatial modes can be created by applying a control field that is position dependent [Hos09], whereas in order to create temporal modes, a population distribution which depends on transition frequency can be generated by using hole-burning techniques [Afz10].

In our experimental implementation of the multimode quantum memory, the material we used for the memory is ensembles of electron spins, and the manipulation of the electron spin state is achieved by microwave pulses. It is convenient to generate spatial modes by applying a magnetic field which is inhomogeneous over the volume of the ensemble. A good example of such inhomogeneous field is a magnetic field gradient whose intensity and duration are both controllable.

3.2.1 Magnetic field gradient

The electron spins are placed in the static magnetic field B_0 of the spectrometer, with the direction of B_0 along the z-axis. An additional gradient magnetic field along the same direction is created by an anti-Helmholtz coil placed near the sample. Figure 3.1 shows the configuration of the coil, the sample and the static magnetic field. The magnetic field generated by this coil $\vec{B}_{\text{coil}}$ can be calculated using the Biot-Savart Law

$$d\vec{B}_{\text{coil}} = \frac{\mu_0}{4\pi} \frac{I \cdot d\vec{l} \times \hat{r}}{r^2} \tag{3.6}$$

where I is the current through the coil, $d\vec{l}$ is a section of the coil to be integrated. At positions close to the origin O, the variation in $\vec{B}_{\text{coil}}$ in the plane $z = z_0$ depends on the

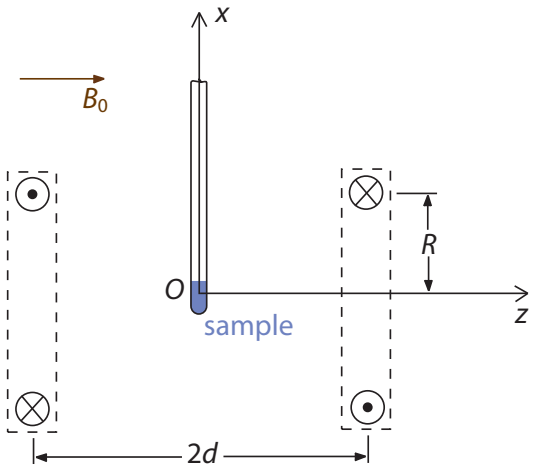

FIGURE 3.1: Lateral view of the field gradient coil and the sample tube. The static field B_0 is along z direction. x is the vertical direction, and y-axis is pointing out the paper.

second order of x and y,

$$\delta\vec{B}_{\text{coil}} \sim O(\frac{x^2+y^2}{r^2}). \tag{3.7}$$

Therefore, for a small volume around the origin, i.e. $x, y, z \ll R, d$, where R, d are the radius of the coil and the distance from the center of the sample tube to the coil, respectively, up to the first order approximation we can assume $\vec{B}_{\text{coil}}$ to be dependent only on z. Besides, because of the geometry of the coil, $\vec{B}_{\text{coil}}(x = 0, y = 0, z)$ will only have a z-component, which is

$$B_{\text{coil},z}(z) = \mu_0 I \cdot \frac{3R^2}{d(R^2+d^2)^{\frac{3}{2}}} \cdot z. \tag{3.8}$$

From Equation 3.8 we can calculate the gradient of this field with respect to z,

$$G_z = \frac{\partial B_{\text{coil},z}}{\partial z} = \mu_0 I \cdot \frac{3R^2}{d(R^2+d^2)^{\frac{3}{2}}}. \tag{3.9}$$

We see that G_z is independent of any coordinate, i.e. it is uniform over the small volume around the origin. Moreover, since $B_{\text{coil},x} = B_{\text{coil},y} = 0$ and the field gradient with respect to x, y coordinate are $G_x = G_y = 0$, it will not cause any confusion to use B_{coil} and G instead of $\vec{B}_{\text{coil}}$ and G_z. We will keep using these notations in the following text.

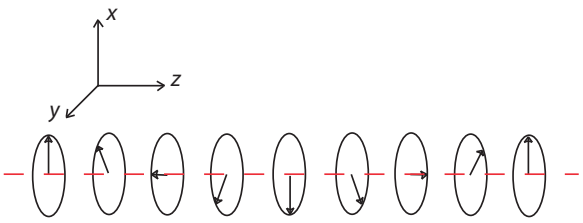

FIGURE 3.2: Illustration of the phase distribution of the spins aligning along z-axis with the presence of a field gradient G_z.

3.2.2 Collective phase mode

Since G is generated by the only non-zero component (the z-component) of B_{coil}, which is along the same direction as the external static field B_0, it will affect the Larmor frequency of the electron spins in the sample. Suppose the Larmor frequency of the spins without the gradient is $\omega_0 = \frac{\mu_0 g_e}{\hbar} B_0$, the variation in the Larmor frequency after applying the gradient G will be

$$\delta\omega = \frac{\mu_0 g_e}{\hbar} \cdot \delta B = \frac{\mu_0 g_e}{\hbar} G \cdot \delta z. \tag{3.10}$$

This will lead to a variation in the phase of the spins

$$\delta\phi = \int \delta\omega dt = \frac{\mu_0 g_e}{\hbar} \int G dt \cdot \delta z. \tag{3.11}$$

When G is time-independent and uniform in space, the accumulated phase variation ϕ will have a linear relationship with z. A figure illustrating the phase distribution along z-axis of the spins is shown in Figure 3.2. This is equivalent to introducing a plane wave to the ensemble of electron spins with the wave vector $\vec{k}$ where

$$k_x = k_y = 0, \quad k_z = \frac{\partial\phi}{\partial z} = \frac{\mu_0 g_e}{\hbar} \int G dt. \tag{3.12}$$

For simplicity, we will use k to denote the wave vector $\vec{k}$ in the following.

Using this definition, the additional phase factor introduced by the gradient to the jth spin in the ensemble will be $e^{i\phi_j} = e^{i\vec{k}\cdot\vec{r}_j} = e^{ikz_j}$. Therefore the single collective excited state (Equation 3.2) now becomes

$$|e\rangle'_{\text{ens}} = \frac{1}{\sqrt{N}} \sum_j e^{ikz_j} |g_1 \cdots e_j \cdots g_N\rangle. \tag{3.13}$$

Since the phase of each component depends on the spatial coordinate of the spin, this collective mode is also called a *spatially distributed collective phase mode*. Each mode described by Equation 3.13 is characterized by a specific wave vector k, so it is also possible to define the spatially distributed phase mode by its wave vector k. We can name such a phase mode as a ***k-mode***.

3.2.3 k-Space and holographic quantum memory

Obviously, the wave vector k constitutes a parametric space in which each collective phase mode corresponds to a specific value of k. Although in our situation only k_z is non-zero — the k-space is one dimensional — it is nevertheless possible to generalize it to a two or three dimensional k-space by introducing magnetic field gradient along other directions, i.e. creating non-zero G_x and G_y [Gos10]. In the following discussion we will consider a one dimensional k-space as this corresponds to what we used in the experiment.

As discussed in Section 3.1.3, to store multiple qubits in a single ensemble requires the same number of different collective modes that are mutually orthogonal. Here, with the definition of k, the orthogonality relation Equation 3.5 becomes

$$\langle e, k_1 | e, k_2 \rangle = \frac{1}{N} \sum_j e^{i(k_2 - k_1) z_j} = \frac{1}{N} \int_{-r}^{r} e^{i(k_2 - k_1) z} n(z) dz = 0, \tag{3.14}$$

where $n(z)$ is the density of spin along the z-axis. It can be seen that for electron spin ensembles with different density profiles the orthogonality relation can be different. However, when the number of spins in the ensemble N is large enough, and when the the two k-modes are sufficiently different, i.e. $|k_1 - k_2|$ is large enough, the orthogonality relation is nearly always satisfied. Equation 3.14 therefore becomes

$$\langle e, k_1 | e, k_2 \rangle \approx \delta_{k_1, k_2}. \tag{3.15}$$

According to the previous discussion, these orthogonal k-modes can be used to store multiple qubits in the ensemble of spins, and the qubits stored in these modes can be addressed separately without causing crosstalk between them. Since in this quantum memory

scheme the qubits are encoded in the spatially distributed collective phase mode of the ensemble, which is the same as in holography, this memory scheme is also called *holographic quantum memory*.

A uniform and unidirectional field gradient is not a necessary condition for building the multimode memory. With a more complex field gradient, it is still possible to create a collective phase mode over the spin ensemble, except that now the parameter k designating each phase mode becomes a function of the spatial coordinate of the spin, $\vec{k}(\vec{r})$, instead of a simple vector $\vec{k}$. However, as long as the gradient is reversible and the orthogonality between different modes is satisfied, the principle of the multimode memory described in the rest of this chapter still works in the same way.

3.3 Characterizing field gradient coil

The field gradient coil is designed to fit the dimension of the microwave resonator. The distance between the two coils is $2d = 4$ cm, and the radius of the coils is $R = 2$ cm. The coils are placed outside the resonator. A top viewed picture of the coil is shown in Figure 3.3. The sample is placed at the origin O of the frame in a quartz tube, and its typical dimension is less than 3 mm radius in the yz plane and 5 mm in x direction (perpendicular to the paper plane). Since the sample volume is small, according to previous discussion, the only significant component of the field gradient is along the z-axis.

The magnitude of the field gradient depends on the current in the coil, I, as well as the number of windings N on each side of the coil. Therefore, the actual field gradient generated by the coil is (see Equation 3.9)

$$G = \frac{3\mu_0 R^2}{d(R^2 + d^2)^{\frac{3}{2}}} \cdot IN. \tag{3.16}$$

Using the above values for R and d, this gives an estimation of $G \approx 1.66\times10^{-2}\cdot N$ (G/mm·A).

Another consideration in the design of the coil is that the self-inductance of the coil increases as N^2. In order to limit the rise time of the field gradient pulse, i.e. the rise time

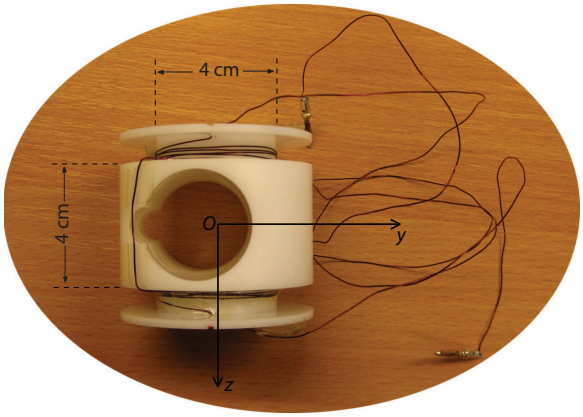

FIGURE 3.3: Top viewed photo of the field gradient coil. The coil has 5 turns and the wire is wound in opposite direction on the two sides. It generates a nearly homogeneous gradient along z around the origin point O, where the sample resides in the resonator.

of the current pulse through the coil, to within a microsecond, N should be small. An estimation of the inductance of the gradient coil gives $L \approx 0.15N^2$ μH.

In our experiment, we use field gradient pulses to create different k-modes in the sample. It is necessary to find out the appropriate current I and number of windings N to create the smallest $k \neq 0$ mode that is orthogonal to the $k = 0$ mode. In this k-mode the phase variation of all the spins in the sample should be a minimum of π along the z-axis. This gives the following condition

$$\Delta\phi = \int \gamma \Delta B dt = \int \gamma G \Delta z t \geq 2\pi, \tag{3.17}$$

where Δz is the z dimension of the sample. As an estimation we can assume the gradient G to be constant during the pulse, so that Equation 3.17 becomes

$$\gamma G \Delta z \Delta t \geq 2\pi. \tag{3.18}$$

Taking $\Delta z \approx 3$ mm, $\Delta t \approx 1$ μs, we have $G \approx 0.1$ G/mm. Therefore, when the current is about 1 A, $N = 5$ will be a good estimation for the number of windings, and the resulting inductance will be $L \approx 4$ μH.

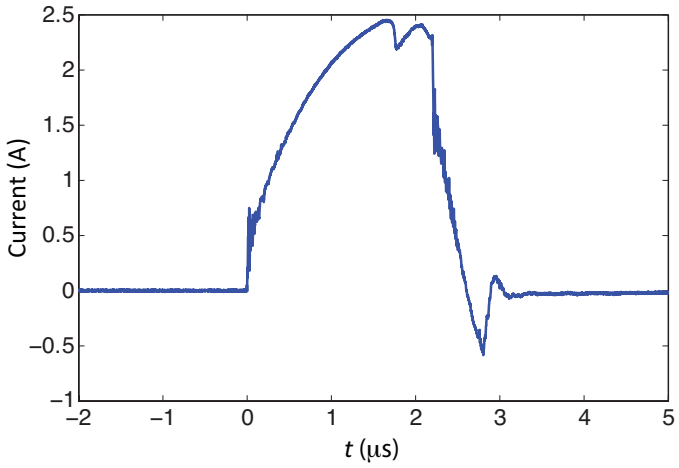

Figure 3.4: Current response of the field gradient coil to a 2.2 μs square voltage pulse of 2.5 V, measured by the voltage drop across a 1 Ohm resistor in series with the coil.

3.3.1 Experimental characterization

In a CW EPR measurement, applying a field gradient to a sample with a narrow intrinsic EPR linewidth will make the observed linewidth, Δl_{pp}, broader, as given by $\Delta l_{\mathrm{pp}} = G\Delta z$. By measuring CW EPR linewidth as a function of coil current and comparing inferred gradient with the theoretical estimation, we get $G_{exp} \approx 0.84 G_{th}$.

The response of the gradient coil to a voltage pulse is also measured by recording the voltage across a 1 Ohm resistor in series with the coil. Figure 3.4 shows the response to a voltage pulse of 2.5 V and duration of 2.2 μs. The rise time is about 1.8 μs, and the maximum current is close to 2.5 A. Although the current through the coil during each gradient pulse is not constant, according to Equation 3.12 the k-mode created by the gradient pulse in fact depends only on the integral of the gradient over time, i.e. the integral of the current over time, the electric charge, through the coil during each pulse:

$$k = \frac{\mu_0 g_e}{\hbar} \int G dt \propto \int I dt. \tag{3.19}$$

Therefore, by adjusting either the length or the amplitude of the current pulse, we can create any k-mode fairly precisely.

3.3.2 Creating orthogonal k-modes

Section 3.2.3 gave the theoretical condition for an orthogonal k-mode. Here I will describe how to interpret this condition into experimental parameters.

A microwave pulse with tipping angle $0 < \theta < \pi$ creates coherence in the spins which are initially polarized by B_0 along the z-axis, and leaves the spins with a non-zero magnetization component in the xy plane. Precession of this magnetization causes it to radiate into the resonator and can be detected. The spins are therefore in the radiative $k = 0$ mode. However, if each of the spins has different phase such that their magnetizations cancel each other out, the total magnetization of the spins is in a subradiative state and the phase distribution constitutes an orthogonal k-mode.

In our experiment, in addition to the controlled field inhomogeneity introduced by the gradient pulses, there is a random inhomogeneity caused by variations in the environment of the individual spins of the ensemble and some residual gradients in the static field B_0. The effect of this uncontrolled but static inhomogeneity can be refocussed using a Hahn echo sequence ($\pi/2$ — π — echo).

In order to look for orthogonal k-modes, we insert a field gradient pulse between the first $\pi/2$ pulse and the refocusing π pulse in the Hahn echo sequence. The spin echo signal is measured with the length of the field gradient pulse t_g gradually increased from 0 to 2.4 μs (Figure 3.5 (a)). Figure 3.5 (b) shows the transient signals for several different t_g, in comparison to the standard Hahn echo sequence. The the variation of echo intensity as a function of the time integral of the gradient G (which is equivalent to k) is shown in Figure 3.6.

Together, Figures 3.5 and 3.6 show that between $t_g = 0$ and 1.2 μs the echo intensity decreases as t_g increases. This indicates that in this regime the spins are getting more and more dephased with the increase of k. For a certain value of t_g the echo intensity gets to zero, which means that the spin magnetization is completely cancelled out due to the dephasing effect of the field gradient, therefore the k-mode created by this gradient pulse is orthogonal

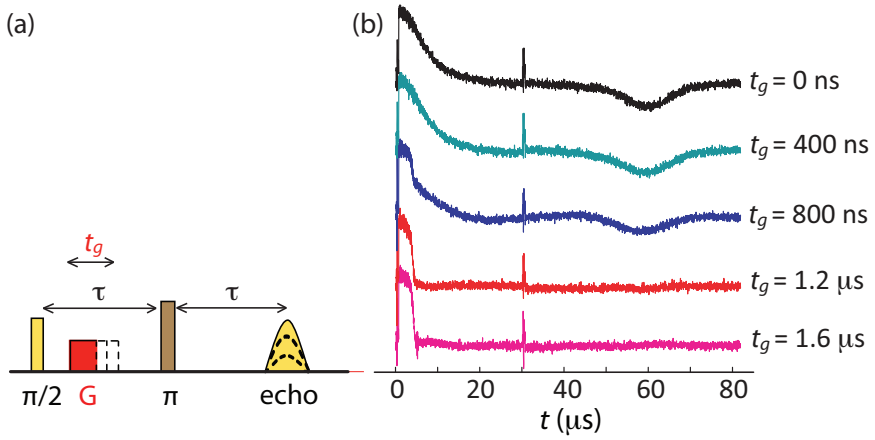

FIGURE 3.5: (a) Pulse sequence used for demonstrating the effect of a field gradient pulse. As the length of the gradient pulse is changed, the intensity of the echo signal also changes (dashed lines). (b) Transient spectra for different lengths of the gradient pulse. t_g denotes the length of the voltage pulses applied. These experiments were done with the ^{14}N@C$_{60}$ sample in CS_2 solution at room temperature.

to the $k = 0$ mode. Here we take $t_g = 1.3$ μs as the length of the gradient pulse that creates the first orthogonal k-mode (indicated by the green circle in Figure 3.6). This t_g is used for all the gradient pulses in the following experiments using pulsed field gradient.

The blue curve in Figure 3.6 is the theoretical calculation of the spin echo intensity as a function of k, while the echo intensity is proportional to the total magnetization of the spin ensemble in xy plane. After a $\pi/2$ pulse and a gradient pulse that creates a phase mode k, if we ignore the dephasing effect due to the random and static inhomogeneity, the total magnetization of all spins will be (see Equation 3.14)

$$M \propto \mathbb{R}. \int_{-r_0}^{r_o} e^{ikz} n(z) dz \propto \int_{-r_0}^{r_0} \cos(kz) \sqrt{r_0^2 - z^2} dz. \tag{3.20}$$

Here $n(z) \propto \sqrt{r_0^2 - z^2}$ is because the N@C$_{60}$ solution sample is in a tube and therefore has a non-uniform cross-sections along z. Integrating the right-hand side of Equation 3.20 gives

$$M \propto \frac{J_1(kr_0)}{kr_0} \tag{3.21}$$

where $J_1(x)$ is the 1st order Bessel function of the first kind. In addition, the microwave field B_1 has a second order radial inhomogeneity over the sample volume, i.e. $B_1(r) =$

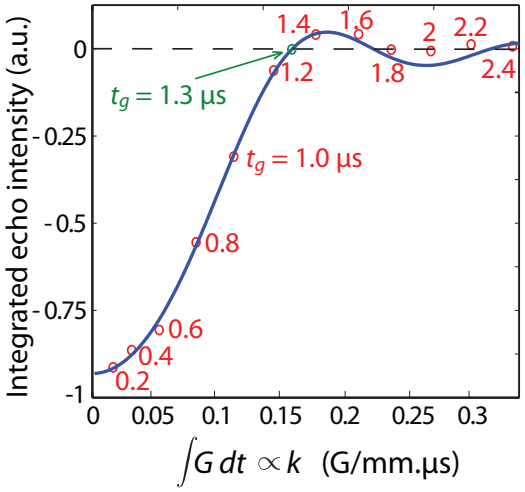

FIGURE 3.6: Echo intensity as a function of the time integral of the field gradient, which is also proportional to the wave number k. The numbers in red are the length of the voltage pulse in μs for each data point (red circle), the green circle is the point we take as an orthogonal k-mode from the theoretical calculation (blue curve).

$B_{10}(1 - ar - br^2)$ where a, b are correcting coefficients. By taking this into consideration, we obtain the theoretical calculation which reproduces very well the variation of the measured echo intensities.

3.4 Storage of microwave pulses in electron spins

In this section I discuss how to achieve the storage of microwave excitations in the electron spin ensemble. As a first step I will demonstrate the storage of a single microwave pulse achieved by applying a field gradient pulse after the microwave pulse, and the retrieval achieved by reversing the field gradient and refocusing the spin coherence. Then I will continue to demonstrate the storage of multiple microwave pulses and their retrieval in arbitrary order.

In this experiment, $^{14}N@C_{60}$ sample in liquid carbon disulfide (CS_2) solution is used. Its center EPR line ($m_I = 0$) has a spin relaxation time $T_1 = 120$ μs and decoherence time $T_2 = 80$ μs at room temperature [Mor06].

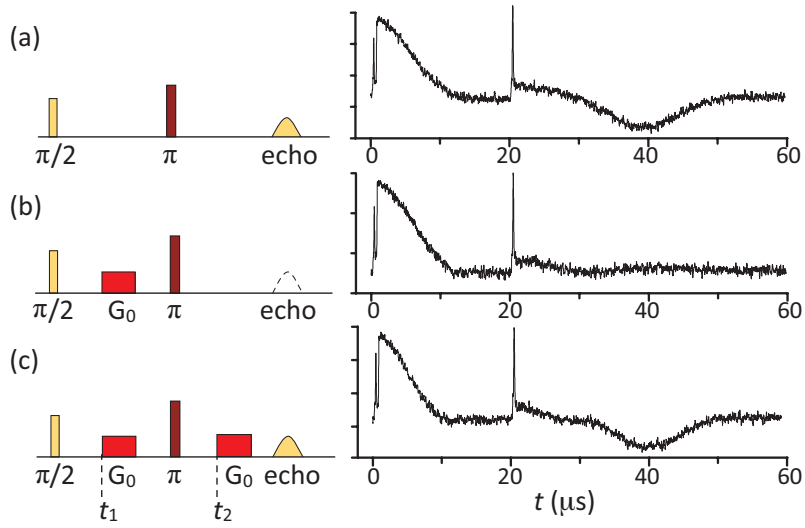

Figure 3.7: Pulse sequences and spectra for storing single microwave pulses: (a) Hahn echo. (b) Storing the first $\pi/2$ microwave pulse in the ensemble by applying a gradient pulse G_0 between the $\pi/2$ pulse and the refocusing pulse. (c) Retrieving the stored microwave pulse by applying a second identical gradient pulse G_0 after the refocusing pulse.

3.4.1 Storage of single microwave pulses

In the previous section it was already seen that a field gradient pulse of $t_g = 1.3$ μs (denoted as G_0) can create an orthogonal k-mode (denoted as k_0) in the spin ensemble. We utilize this mode for the storage of single microwave pulses.

As in the Hahn echo sequence (Figure 3.7 (a)), a π pulse is used to refocus the inhomogeneities from environmental spins and the static field. The effect of the refocusing pulse on the k-modes is that it inverts all the k vectors in the k-space, so that a $+k$ mode becomes $-k$ mode. Meanwhile, the gradient pulses will affect all the existing k-modes. A gradient pulse G' corresponding to a wave vector k' will simultaneously shift all the k-modes to a new position in the k-space with a new wave vector $k + k'$.

Therefore, when a gradient pulse G_0 is applied after the $\pi/2$ pulse in the Hahn echo sequence, the spin coherence generated in the ensemble by the microwave pulse is translated from $k = 0$ mode to k_0 mode (orthogonal to $k = 0$). At time τ the refocusing π pulse flips all the electron spins so that they experience reversed environmental inhomogeneities in the second period of evolution. However, since the inhomogeneity created by the gradient pulse

is not compensated for because there is no gradient pulse after the refocusing pulse, the spin coherence stays in the $-k_0$ mode and we will not observe an spin echo at time 2τ as in the Hahn echo experiment. This indicates that the spin ensemble is in a subradiative state. In other words, we can say that the spin coherence is *stored* into the k_0 mode created by the gradient pulse G_0.

Since only the $k = 0$ mode is radiative, in order to recover the stored spin coherence it is necessary to bring it from the k_0 mode back to $k = 0$ mode. There are two ways of achieving this translation. One is to apply an inverse gradient pulse $-G_0$ which shifts all the modes by an amount of $-k_0$, so that the k_0 mode goes back to $k = 0$ mode; the other is to apply the same gradient pulse G_0 but after the refocusing pulse: the refocusing pulse moves the k_0 mode to $-k_0$, then the positive gradient pulse G_0 shifts the $-k_0$ mode back to $k = 0$ mode. As the circuit used for generating current pulses for the gradient coil is more reliable when its voltage polarity is kept unchanged, we choose the second method to return the k_0 mode to $k = 0$ mode, as shown in Figure 3.7 (c). Since the spin coherence is now in the radiative $k = 0$ mode, a spin echo will be detected at time 2τ. We say that the spin coherence created by the microwave pulse is now *retrieved* from the spin ensemble.

Figure 3.7 (b) and (c) show the pulse sequence for storing and retrieving a single microwave pulse. In the transient spectra, it is shown that when there is only one gradient pulse G_0 before the π pulse but none after the π pulse the echo disappears, whereas when there is a gradient pulse on both side of the π pulse, the echo reappears at the same position as in the Hahn echo sequence shown in (a). In Figure 3.7 (b) and (c) the gradient pulses are applied at $t_1 = 10$ μs and $t_2 = 30$ μs (only one gradient pulse at t_1 for (b)). Since $t_1 \approx T_2^*$ ($T_2^* \approx 10$ μs), the FID is not affected by the first gradient pulse in both (b) and (c); similarly, since $2\tau - t_2 \approx T_2^*$, the echo signal is also unaffected by the second gradient pulse in (c).

From its definition, the effect of a gradient pulse is to introduce a phase distribution to the spin ensemble, which should not depend on the time at which the gradient pulse is applied. Therefore it is useful to demonstrate that changing the position of the gradient pulse

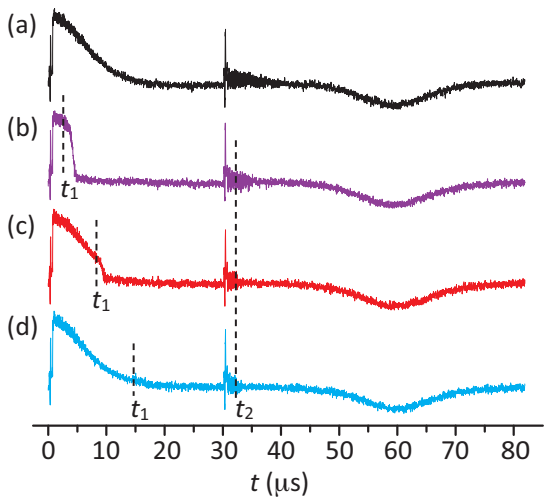

Figure 3.8: Spectra for storing single microwave pulses with the gradient pulse applied at different time: (a) Hahn echo. (b) $t_1 = 1$ μs. (c) $t_1 = 8$ μs. (d) $t_1 = 15$ μs. For (b)-(d), $t_2 = 31$ μs.

does not affect the storage and retrieval of the microwave pulse. Figure 3.8 (b)-(d) show the transients for storing single microwave pulse with different t_1, where t_2 is kept the same. It can be seen that the recovered spin echo signal appears at the same position $t_{\text{echo}} = 2\tau$ as in the Hahn echo sequence (Figure 3.8 (a)) for all different t_1. Moreover, the intensity of the recovered echo is not affected by the position of the gradient pulse. By comparing the integrated echo intensity in the Hahn echo experiment and the microwave pulse storage experiment, we obtain a retrieval efficiency of 92%. The imperfect retrieval could be due to two reasons: the current pulses may not be perfectly reproducible, so that the dephasing effect of the two field gradient pulses on both sides of the π pulse do not exactly compensate each other; there may be some additional decoherence caused by the gradient pulses to the electron spins which are not reversible by the π pulse, for example the interaction between the spins and the eddy currents induced by the current pulses in the resonator.

The only difference in Figure 3.8 (b)-(d) is the cut-off of FID at different t_1 when t_1 is shorter than T_2^* (which can be seen in (b) and (c)). This is because the strong field inhomogeneity created by the gradient pulse accelerates the dephasing process of the spin magnetization in xy plane, which causes a faster decay of the spin signal. In all three cases $2\tau - t_2 = 29$ μs $> T_2^*$, so the retrieved echo signals are complete.

3.4.2 Storage of multiple microwave pulses

Based on similar principle to single microwave pulse storage, multiple microwave pulses can be stored in one electron spin ensemble by putting each microwave pulse into a different orthogonal k-mode.

Random-access memory

In order to create these orthogonal k-modes, it is necessary to apply the gradient pulses corresponding to different zeros of Equation 3.21. But the zeros of $J_1(x)$ are not equidistant, so it will be inconvenient to create different modes with wavevector k that correspond to the zeros of Equation 3.21 only by adjusting the length of the gradient pulse t_g, considering the relatively long rise time of the current pulse. However, according to Equation 3.15, when k' is sufficiently large the $k = k'$ mode is always approximately orthogonal to the $k = 0$ mode. Therefore we can make the approximation that if $k_1 = k_0$ is orthogonal to $k = 0$ mode, $k_2 = 2k_0, \ldots, k_n = nk_0$ are all orthogonal to $k = 0$ mode as well. Moreover, this approximation will become an exact relation if the sample (ensemble of spins) has a constant cross-section along z, for in this situation Equation 3.20 becomes

$$M \propto \mathbb{R}. \int_{-r_0}^{r_0} e^{ikz} n(z) dz \propto \int_{-r_0}^{r_0} \cos(kz) dz \propto \frac{\sin(kr_0)}{kr_0}. \tag{3.22}$$

As the sinc function has a series of equidistant zeros, all the $k_n = nk_0$ modes will be orthogonal to $k = 0$ mode.

Now that the orthogonal nk_0 modes are equidistant in the k-space, we can create them by repeating the same gradient pulse G_0 for n times and shift the wave vector by k_0 step by step. And as discussed in the previous section, taking a nk_0 mode back to the $k = 0$ mode can be realized by applying the same number of G_0 of the same polarity after a π pulse. This provides us with a scheme for navigating through all the orthogonal nk_0 modes, and therefore a scheme for storing and retrieving multiple microwave pulses:

Each microwave pulse can be stored in a specific orthogonal mode by applying the corresponding number of gradient pulses after the microwave pulse, and its retrieval can be

achieved by taking this particular mode back to the radiative $k = 0$ mode.

In addition, since the access to any nk_0 mode can be realized by a certain combination of gradient pulses and π pulses, this enables the non-sequential access to any of the stored microwave pulses. In this sense, this type of multi-mode memory can also be thought of as a ***quantum RAM***.

Experimental demonstration

In our experiment, we show the storage and retrieval of two microwave pulses. Two different ways of retrieval are used to demonstrate the principle of random-access: retrieving in the same (Figure 3.9 (a)) and reverse (Figure 3.9 (b)) order as that in which the two pulses are stored. Figure 3.9 (a) and (b) also show the evolution of the two collective modes used to store the two microwave pulses by showing the translation of the wave vector k_1 and k_2 in the k-space.

In order to distinguish the microwave pulses, we apply them with different phases. In the quadrature detection, we are able to distinguish the echoes of the two different microwave pulses by determining the phase of the echo signal. In Figure 3.9 (a'), (b') the two microwave pulses P_1 and P_2 are along $-y$ and $+y$ axis respectively (180° out of phase), such that the spin coherence they created (FID) are detected in σ_x (in +X and −X respectively). Since the refocusing pulse along x does not affect the signal in σ_x, the spin echo will have the same sign as the FID. Therefore in Figure 3.9 (a') the first echo should be from the first pulse P_1 (noted as E_1) because it is in +X, with the second echo corresponding to P_2 because it is in −X (noted as E_2); similarly, the first and second echoes in (b') are from P_2 and P_1, respectively. Figure 3.9 (a') and (b') together demonstrate that by applying an appropriate combination of gradient pulse and refocusing pulse, we are able to move the stored microwave pulses in the k-space in a controlled manner, and can choose which microwave pulse to retrieve at which moment.

This random accessibility is also demonstrated for microwave pulses with different phase relations. Figure 3.9 (a") and (b") show the storage and retrieval of two microwave pulses

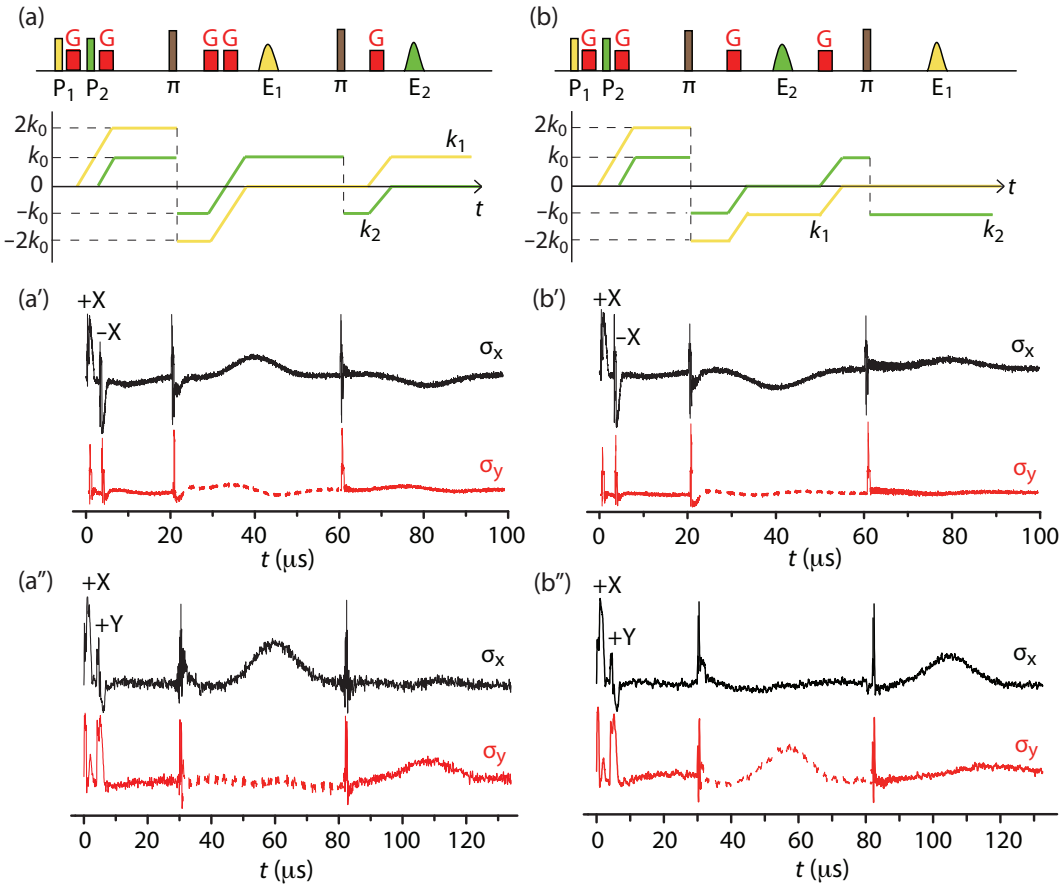

FIGURE 3.9: (a) Pulse sequence and the translation of the wave number k_1, k_2 in the k-space, (a')–(a") Spectra for storing two microwave pulses and retrieving them in the **same** order as they are stored. (b) Pulse sequence and the translation of the wave number k_1, k_2 in the k-space, (b')–(b") Spectra for storing two microwave pulses and retrieving them in the **reverse** order as they are stored. In both (a) and (b), all the refocusing pulses are along y-axis, therefore they only invert the sign of the signals in σ_y and those in σ_x is left unchanged. The dashed traces in (a'), (a"), (b'), (b") indicate an inversion of the signal, such that all the echoes appear with a positive sign.

using the same pulse sequence, but with P_1 and P_2 along $-y$ and $-x$, respectively (FID in +X and +Y, respectively). In addition, we also verified that two microwave pulses with the same phase can be stored and retrieved using the same pulse sequence. These experiments imply that independent storage and retrieval can be carried out for microwave pulses of any phase.

In QIP, the information is usually encoded in the phase of a photon. Here, the phase of the microwave pulse can be considered as the information, although a microwave pulse contains

a large number of photons. Therefore the spin ensemble that stores multiple microwave pulses constitutes a multimode memory.

Although the principle of independent storage and retrieval is demonstrated for two microwave pulses, it can be generalized to $n > 2$ microwave pulses with no difficulty: it is only necessary to create n orthogonal k-modes $k_0, \cdots, nk_0$ by applying the corresponding number of gradient pulses, and take them back to $k = 0$ mode at required moment by applying the appropriate sequence of π pulses and gradient pulses.

3.4.3 Crosstalk between stored microwave pulses

Equation 3.15 is correct on two conditions: one is that the two k-modes are sufficiently different, which has been discussed; the other is what we have assumed to be automatically satisfied when using an ensemble of spins, which is that the number of spins N is large enough [Tor08b]. Actually, the latter is true only when the excitation to be stored in the ensemble is very weak such that it is close to a single excitation as defined by Equation 3.2. In our case, this means that the microwave pulses we want to store in the electron spin ensemble should contain only a few photons or even only a single photon. However, this condition is not satisfied because the microwave pulses applied in our experiments are of high power, and the number of photons in the resonator during the pulses can be estimated to be $\sim 10^{18}$. In this case it is necessary to study the crosstalk between different k-modes in a classical picture.

Operator formalism calculation

Since any crosstalk among many k-modes can be considered as a superposition of crosstalk between different pairs of k-modes, it suffices to study the crosstalk between two general k-modes k_1 and k_2. The designed pulse sequence is shown in Figure 3.10, where G_1, G_2 represent the gradient pulses that can create the k_1, k_2 mode. Assume the spin is initially in S_z state, its final state after the sequence can be calculated using the operator formalism of pulsed EPR.

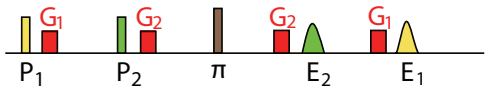

FIGURE 3.10: Pulse sequence for measuring crosstalk between two k-modes. The two gradient pulses are labelled as G_1, G_2 for generality in the analytical calculation, while in the experiments the gradient pulses are kept the same, $G_1 = G_2 = G_0$.

In the operator formalism [Abr85, Sor84], a general operator θS_ϕ represents a microwave pulse which flips the spin by an angle θ along the axis ϕ. Therefore the sequence in Figure 3.10 can be written as

$$S_z \xrightarrow{\gamma S_x} \xrightarrow{(k_1 z)S_z} \xrightarrow{\delta S_x} \xrightarrow{(k_2 z)S_z} \xrightarrow{\pi S_x} \xrightarrow{(k_2 z)S_z} E_2 \xrightarrow{(k_1 z)S_z} E_1 \tag{3.23}$$

where $\gamma S_x, \delta S_x$ are the operators of the two microwave pulses, $(k_i z)S_z$ are the operators for the gradient pulses as they are equivalent to introducing a phase along the z-axis with $k_i z$ the phase depending on the coordinate z, πS_x represents the refocusing pulse.

Calculation of Equation 3.23 gives (terms with S_z are ignored as only S_x, S_y components are detected in the experiment)

$$\begin{aligned} E_1 &= -[\cos\gamma\sin\delta\cos k_1 z + \sin\gamma(\cos\delta\cos^2 k_1 z + \sin^2 k_1 z)]S_y \\ &\quad -[\sin\gamma(\cos\delta - 1)\sin k_1 z\cos k_1 z + \cos\gamma\sin\delta\sin k_1 z]S_x, \\ E_2 &= -(\cos\gamma\sin\delta + \sin\gamma\cos\delta\cos k_1 z)S_y - \sin\gamma\sin k_1 z S_x. \end{aligned} \tag{3.24}$$

For k_1 large enough, summing over the ensemble, i.e. integrating over z, leads to cancellation of all the terms containing $\sin k_1 z$, $\cos k_1 z$ and $\sin k_1 z \cos k_1 z$, and $\int \sin^2 k_1 z = \int \cos^2 k_1 z$. After renormalization to unity, Equation 3.24 simplifies to

$$E_1 = -\frac{1}{2}\sin\gamma(\cos\delta + 1)S_y, \quad E_2 = -\cos\gamma\sin\delta S_y. \tag{3.25}$$

Meanwhile, the spin echo created by a microwave pulse γS_x in a Hahn echo sequence is $-\sin\gamma S_y$. Comparing with Equation 3.25, the errors in the echo of each pulse caused by the

presence of the other pulse are

$$\begin{aligned} \epsilon_1 &= 1 - \frac{E_1}{\sin\gamma} = \frac{1}{2}(1 - \cos\delta), \\ \epsilon_2 &= 1 - \frac{E_2}{\sin\delta} = 1 - \cos\gamma. \end{aligned} \tag{3.26}$$

To be more general, the second microwave pulse can be of any phase so that the third operators in Equation 3.23 become δS_ϕ. Similar calculation gives

$$E_1 = -\frac{1}{2}\sin\gamma(\cos\delta + 1)S_y, \quad E_2 = -\cos\gamma\sin\delta(\sin\phi S_x + \cos\phi S_y). \tag{3.27}$$

This indicates that the phase of the second microwave pulse affects only the phase of E_2, which is what we expect, and has no effect on E_1. It reduces to Equation 3.26 when calculating ϵ_1 and ϵ_2. Therefore, Equations 3.25, 3.26 can be considered general for echo signals when two microwave pulses are stored in and retrieved from an ensemble.

Measurement of ϵ_1, ϵ_2

Using the pulse sequence given in Figure 3.10, the effect of the two microwave pulses on each other is studied. In our experiment, both E_1 and E_2 are measured as a function of the tipping angles γ and δ, allowing ϵ_1 and ϵ_2 to be calculated. The results in Figure 3.11 verified that ϵ_1 (ϵ_2) is independent of γ (δ) except that for very small γ and δ there are some scatterings in ϵ because the echoes are weak and signal-to-noise ratio is low. Figure 3.11 (a) shows the results for P_1 and P_2 with the same phase (described by Equation 3.25), while Figure 3.11 (b) shows the results for P_1 and P_2 90° out of phase (described by Equation 3.27 with $\phi = 90°$). The fact that Figure 3.11 (a) and (b) look similar to each other verifies the generality of Equation 3.26.

Therefore in Figure 3.12 ϵ_1 (ϵ_2) as a function of δ (γ) is plotted only for the case $\gamma = \pi/2$ ($\delta = \pi/2$) with $\phi = 0$. The data agrees well with the results from the operator formalism calculation, the discrepancy being within 0.005.

There is an intuitive way to understand Equation 3.25. In the classical picture of EPR theory, the intensity of the spin echo is a measure of the magnetization of the spin ensemble in

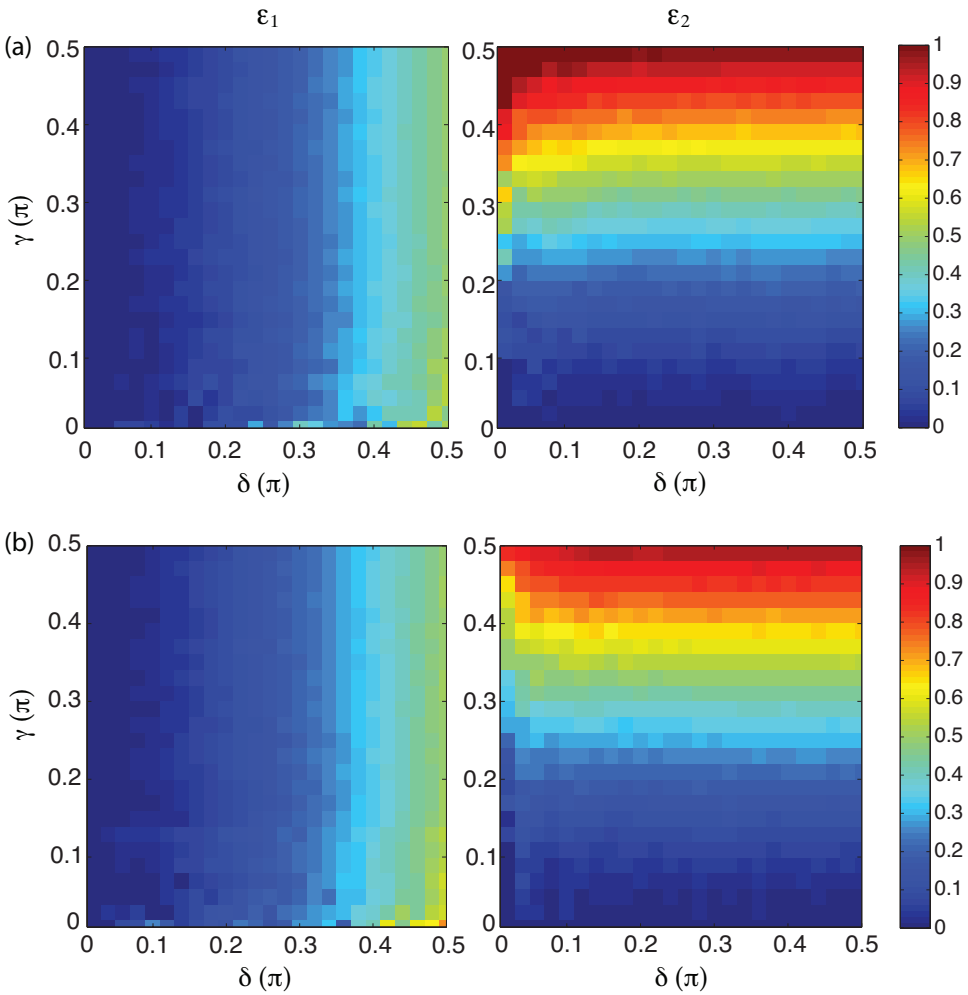

FIGURE 3.11: Relative errors ϵ_1, ϵ_2 in the retrieved echoes as a function of the tipping angles of P_1 and P_2, for (a) P_1 and P_2 in the same phase, (b) P_1 and P_2 90° out of phase.

the xy plane, which is proportional to the initial z magnetization M_z. When two microwave pulses P_1, P_2 are applied one after another, the echo of the second pulse would decrease with the increase of the tipping angle of the first pulse (γ) because M_z is partly consumed by P_1, i.e. $M_z' = (1 - \cos\gamma)M_z$, which will give the first line of Equation 3.25. On the other hand, the decrease of the echo of P_1 with the increase of the tipping angle of P_2 (δ) can be understood as due to the partial refocusing effect of P_2, even if P_2 is not a π pulse as required for optimal refocusing. This leads to the second expression of Equation 3.25.

For small tipping angles, the error ϵ_1, ϵ_2 have the second order dependence on γ and δ

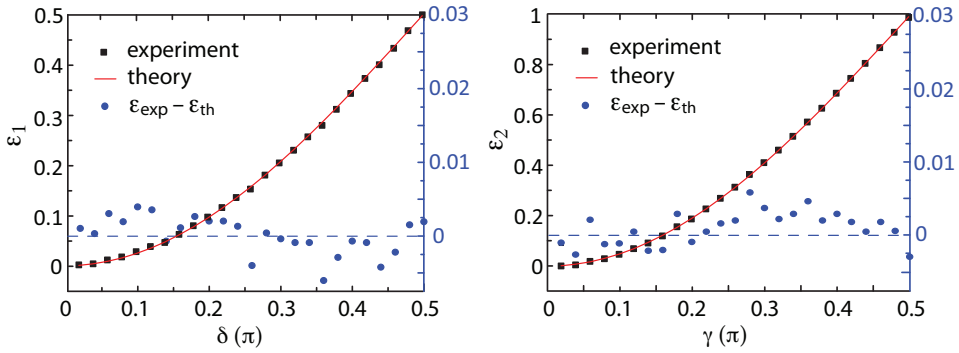

Figure 3.12: A slice spectrum taken from Figure 3.11 (a): ϵ_1 as a function of δ at $\gamma = \pi/2$ and ϵ_2 as a function of γ at $\delta = \pi/2$, with P_1 and P_2 in the same phase. Red curves are calculated from the theoretical model using Equation 3.26. Blue points are the differences between theoretical prediction and experimental data which gives $|\epsilon_{\text{exp}} - \epsilon_{\text{th}}| < 0.007$.

because $1-\cos\theta \approx \theta^2$ when $\theta \ll \pi$. So ϵ_1, ϵ_2 will quickly become negligible for small γ, δ. This means that the crosstalk becomes negligible for microwave pulses with small tipping angle, which is particularly true for weak microwave pulses containing few number of photons. Therefore this verifies the orthogonality relation given by Equation 3.15, and guarantees the validity of the principle of multimode storage at single photon level.

Interference of many microwave pulses

The effect of crosstalk between the multimodes can also be seen in the spectra where multiple microwave pulses are stored in the spin ensemble.

In the experiments shown in Figure 3.13, eight microwave pulses of the same length and phase are applied in sequence, stored and then retrieved in a reversed order. The tipping angles of the pulses in the four spectra are $0.02\pi, 0.04\pi, 0.06\pi, 0.08\pi$, respectively, corresponding to pulse length of 8 ns, 16 ns, 24 ns, 32 ns.

In Figure 3.13 (a) where the tipping angle is small, the echoes as well as the FIDs of the 8 microwave pulses are almost identical. This implies that the spin magnetization M_z of the ensemble is barely consumed by each of the microwave pulses, which agrees with the previous discussion that crosstalk between k-modes diminishes as the second order of the tipping angle. For larger tipping angles (Figure 3.13 (b)-(d)), we can observe distortions in

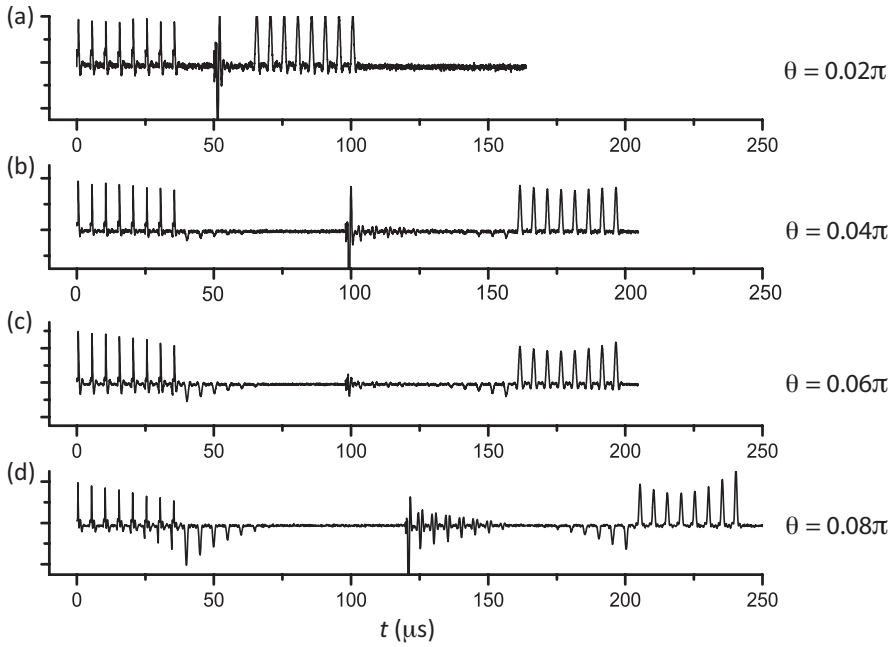

FIGURE 3.13: Crosstalk between different collective modes in the storage of eight microwave pulses. The lengths of each pulses are: (a) 8 ns, (b) 16 ns, (c) 24 ns, (d) 32 ns. The length of a π pulse in this case is 400 ns. This experiment was done with the phosphorous doped ^{28}Si sample at 9 K.

the echoes and a monotonic decrease in the FID. The decrease in the FID can be understood as the result of the decrease in M_z, whereas the distortion in the echoes is the combined effect of the decrease in M_z and the refocusing effect of the microwave pulses themselves. This refocusing effect is seen more obviously in the spikes with opposite sign just after the eight FIDs, which are the "echoes" of the pulses refocused by the other pulses in the sequence.

3.4.4 Capacity of the multimode memory

Having demonstrated that we are able to store multiple microwave pulses and that the crosstalk can be kept small for weak pulses, we address the question of how many pulses it is possible to store in the spin ensemble. In this section I demonstrate that this number is practically limited by the time needed to create the orthogonal k-modes and the decoherence time (T_2) of the spins.

Stack memory

In the experiments using $N@C_{60}$, e.g. Figure 3.9, the second echo is already much weaker than the first one. This is due to the decoherence time of the spins $T_2 \approx 80$ μs, and it limits the lifetime of the multimode memory. One way to get a longer lifetime of the multimode memory is to use a spin ensemble with longer T_2. For this reason, a phosphorous doped silicon sample is used for the capacity experiment. This sample has enriched ^{28}Si of high purity therefore has a long decoherence time at low temperature: $T_2 \approx 450$ μs at 9 K [Tyr06]. In addition, the shape of this sample is rectangular block that has a uniform cross-section along z which is the direction of field gradient. According to Equation 3.22 this means that the orthogonal k-modes are equidistant in k-space, and can be created by applying the same gradient pulses repeatedly.

In order to maximize the number of microwave pulses that can be coherently stored in the ensemble within the lifetime of the memory, it is necessary to use a sequence of storage and retrieval that requires the least number of gradient pulses as well as the refocusing pulses. This is equivalent to requiring the least translation of those orthogonal k-modes in the k-space. The simplest way to meet this requirement is to retrieve all the stored microwave pulses in the reversed order.

An example of the pulse sequence is shown in Figure 3.14. Suppose that n weak microwave pulses are applied in sequence, and each of them is followed by a gradient pulse G. At the moment of the refocusing pulse, each microwave pulse is stored in the k-mode created by all the gradient pulses after it, i.e. the ith microwave pulse P_i is stored in the $(n - i + 1)k_0$ mode. After the refocusing pulse, all k-modes are inverted in k-space. The gradient pulses symmetrically positioned with respect to the refocusing pulse will bring each stored microwave pulse back to $k = 0$ mode at the symmetric position. This manner of last-in-first-out retrieval makes this type of memory a ***quantum stack memory***.

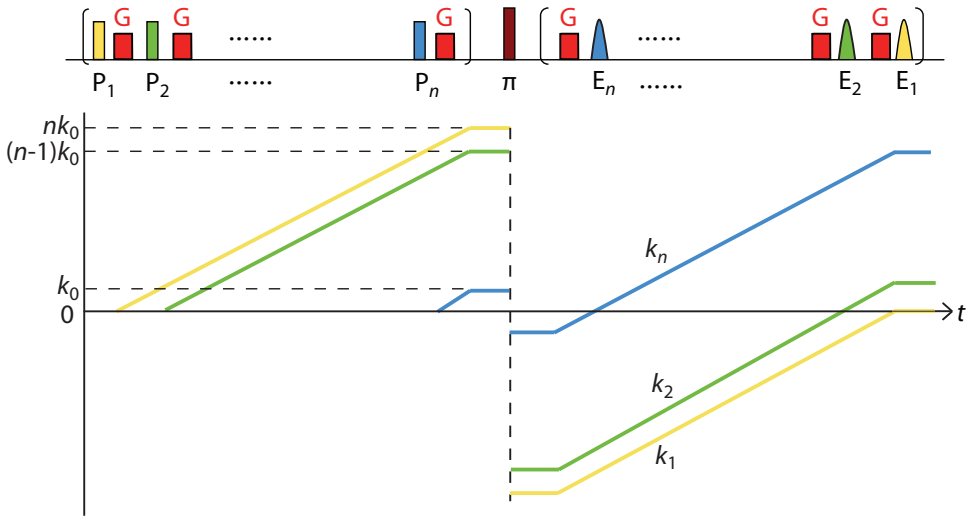

FIGURE 3.14: Pulse sequence and the translation of the wave numbers in the k-space when storing many microwave pulses. The fastest retrieval method is realized by applying the same field gradient at symmetric positions with respect to the refocusing pulse and thus retrieving in a last-in-first-out manner.

Memory capacity

In the actual experiment, the field gradient pulses are replaced by a constant field gradient which exists for all the time. As the orthogonal k-modes are equidistant, a k-mode created by this constant field gradient will be orthogonal to $k = 0$ mode if the separation between two adjacent microwave pulses Δt is tuned such that the field gradient applied during this Δt corresponds to an orthogonal k_0 mode. Besides, in order to be as close as possible to the small tipping angle limit ($\theta \ll \pi$), the microwave pulses applied need to be as short as possible. Since the rise time of the microwave pulses generated by the spectrometer is about 2 ns, the shortest microwave pulse we applied is 4 ns. With the length of a π pulse being 400 ns, this corresponds to a tipping angle of less than 0.01π. As discussed previously, a microwave pulse of very small tipping angle will have almost no effect on the z magnetization, and the microwave pulse after it will generate an FID of the same intensity.

To measure the capacity of the multimode memory, we apply n pulses and observe the retrieved spin echo signal. As long as the signal-to-noise ratio is still above a certain threshold that it is possible to distinguish the echoes, we can say that n is within the capacity of the

multimode memory.

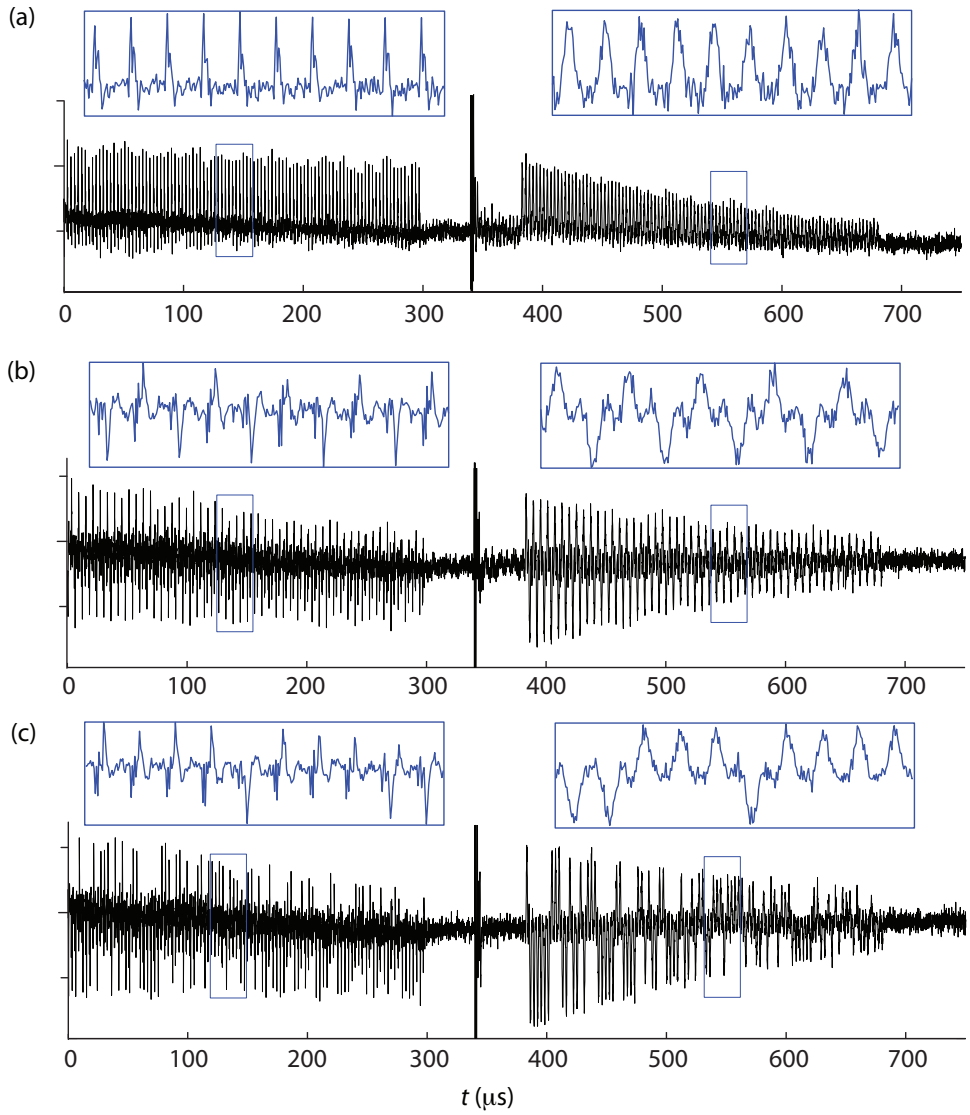

Figure 3.15: Demonstration of memory capacity. 100 weak microwave pulses of (a) the same phase $(+X)$, (b) alternating phase $(+X, -X)$ (c) random phase ($+X$ or $-X$) are stored and retrieved in last-in-first-out manner. The defense pulses of 500 ns long are subtracted from the spectra so that it is possible to observe the FIDs which are about 600 ns long.

Figure 3.15 shows that for $n = 100$ the spin echoes are still intense enough to read. The reduction in the echo intensity is mainly due to the T_2 limit of the sample itself, instead of the crosstalk between the microwave pulses stored in different k-modes. The information 0 and 1 are encoded in the phase of the microwave pulses as the FID observed in +X and −X. In the three subplots of Figure 3.15, the 100 microwave pulses represent 100 bits of

0, alternating 0 and 1, random 0 and 1, respectively. The echoes observed have the same sign as the pulses for the refocusing pulse is along the y-axis, except that they are in a reversed order. This implies that the capacity of the multimode memory composed of this spin ensemble is not less than 100.

In theory, the capacity of a multimode memory N_c is only limited by the number of spins in the ensemble [Wes09]. In practice, however, this number is limited firstly by the decoherence time T_2 of the electron spins, and secondly by the time spent on storing each bit of information. In our experiment, the latter is equivalent to the separation between two microwave pulses Δt, whose lower bound is set by the length of the field gradient needed to create the orthogonal k_0 mode. In the spectra shown in Figure 3.15 the separation is $\Delta t = 3$ μs. Shortening the field gradient pulse meanwhile augmenting its amplitude can help reduce Δt and in return improve the capacity of the memory.

This capacity is measured only for the stack memory that requires a minimum number of translations of the stored information in the k-space. Random access to the k-space requires applying more field gradient pulses and refocusing pulses, which means that the time spent on storing and retrieving each bit of information is longer. So for a random-access memory using the same electron spin ensemble and the same field gradient, the memory capacity N_c will be smaller than that of a stack memory. Nevertheless, the way to improve the capacity is similar: use materials with longer electron spin decoherence time as the medium of the memory; reduce the time needed for moving around in k-space.

3.5 Collective coherence transfer to nuclear spins

The lifetime of a multimode memory T_{m} in an electron spin ensemble is the limited by the electron spin decoherence time $T_{2\mathrm{e}}$. Apart from looking for new materials of longer $T_{2\mathrm{e}}$, it is also possible to extend T_{m} by transferring the information stored in the electron spin coherence to another degree of freedom that has a longer lifetime. One such long-lived degree of freedoms is nuclear spin coherence, and it is convenient to find a system with nuclear spins

present in the environment of electron spins [Tay03, Dut07, Mor08].

The experiment described in this section demonstrates that we are able to transfer multiple microwave excitations stored in the collective k-modes of the electron spin ensemble to nuclear spins, store the multimode coherence in the nuclear spins for a certain period of time, then transfer it back to the electron spins for retrieval.

Coherence transfer sequence

In the ^{31}P doped silicon sample, the donor has an electron spin $S = 1/2$ with a nuclear spin $I = 1/2$ coupled through a hyperfine coupling $A = 117$ MHz [Feh59]. Together they form a four-level system as shown in Figure 3.16 (a). The resonance frequencies between different levels are marked in the figure.

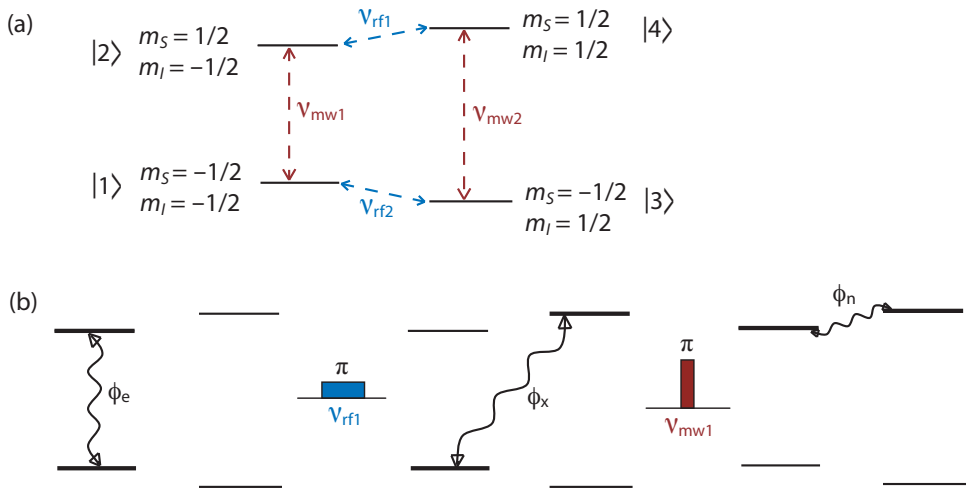

Figure 3.16: (a) Four-level structure used for coherent transfer between electron spins and nuclear spins. The phosphorous donors in the sample have an electron spin $S = 1/2$ and nuclear spin $I = 1/2$. (b) Pulse sequence used for coherence transfer. In each step the coherence exists between the two levels marked in thick black line and connected with the arrow [Mor08].

Figure 3.16 (b) explains the mechanism of coherence transfer from the electron spins to nuclear spins. Initially the electron coherence ϕ_e exists between levels $|1\rangle$ and $|2\rangle$. The radio-frequency π pulse resonant with the $|2\rangle - |4\rangle$ transition transfers ϕ_e to an intermediate state ϕ_x which is a double quantum coherence state. The microwave π pulse resonant with

the $|1\rangle - |2\rangle$ then transfers the double quantum coherence to the nuclear spin coherence ϕ_{n}. To transfer the spin coherence from nuclear spins to electron spins, the reverse pulse sequence, i.e. a microwave π pulse followed by a radio-frequency π pulse is applied.

All pulses here are selective, so that they only create coherence or population transfer between target levels.

Multimode coherence transfer

Figure 3.17 (a) shows the pulse sequence used for the collective coherence transfer. Instead of a microwave π pulse as used in the sequence shown in Figure 3.14, the refocusing pulse is applied in resonance with the nuclear spins (ν_{rf1}) where the collective coherence is stored. Suppose that the multimode coherence is stored in the nuclear spins for a time τ_{n}, in order that the random inhomogeneities experienced by the nuclei can cancel out and the spin coherence can rephase at the moment of transferring the coherence back to electron spins, the refocusing pulse needs to be applied $\tau_{\mathrm{n}}/2$ after the coherence is transferred to the nuclear spins.

We demonstrate the multimode coherence transfer with eight collective modes. The electron spin coherence is initialized by eight microwave pulses of 8 ns applied successively, each followed by a field gradient. Before the first coherence transfer sequence (at $t = \tau_1$), the eight microwave pulses are stored in eight different k-modes of the electron spin ensemble. After the whole transfer process (the two coherence transfer sequences and the refocusing RF pulse in between), if the same field gradients are applied at symmetric positions with respect to the refocusing pulse, we are able to observe eight echoes at $t = \tau_{\mathrm{n}} + 2\tau_1$. Figure 3.17 (b) shows the echo transients. They have the same separation as the microwave pulses, $\Delta t = 5\ \mu$s.

This implies that the multimode coherence can be transferred simultaneously between the electron spin and nuclear spin degree of freedom of the ensemble. This transfer is a transition between hyperfine states of each individual atom and it can be carried out on a time scale given by the hyperfine interaction strength, which is in the order of microseconds

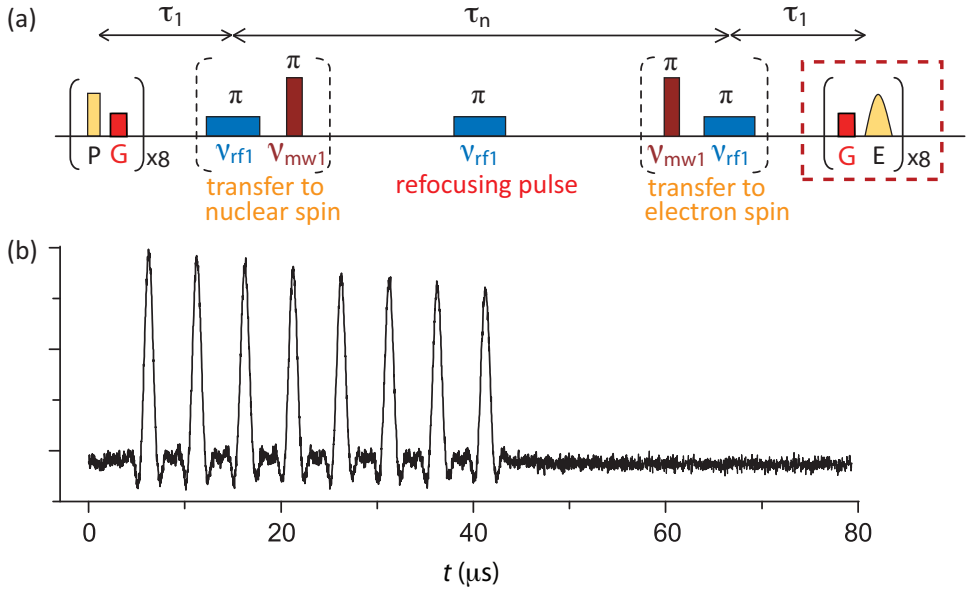

Figure 3.17: Collective coherence transfer between electron spins and nuclear spins. (a) Pulse sequence. The eight microwave pulses of 8 ns are separated by 5 μs from each other, which is short compared to the whole sequence. The length of an rf π pulse is 25 μs, and that of a mw π pulse is 400 ns. τ_1 is the time that all eight microwave pulses are stored in the electron spins, τ_n is the storage time in the nuclear spin. In this experiment, we used $\tau_1 = 10$ μs, $\tau_n = 200$ μs. (b) Echoes of the eight microwave pulses recovered from nuclear spin coherence (dashed red box in (a)).

in our system. Since the nuclear spin decoherence time T_{2n} is usually much longer than the electron T_{2e}, this offers a prospect of extending the storage time of the multimode memory.

3.6 Conclusions

Ensembles of electron spins are demonstrated to be a good candidate for multimode storage of microwave excitations. The collective multimodes are created by applying appropriate magnetic field gradients over the sample volume such that the electron spins in the ensemble form different global phase patterns. The orthogonal collective modes are used for the multimode storage. The retrieval is achieved by applying opposite magnetic field gradients and the stored microwave excitations are read out in the form of a spin echo. By arranging the field gradients and the microwave pulse sequence appropriately, it is possible to build a random access memory for microwave excitations with the electron spin ensembles. In

addition, the multimode coherence stored in the electron spins can be collectively transferred into nuclear spin degree of freedom to benefit a much longer decoherence time hence a longer memory lifetime. Meanwhile, further studies on achieving multimode storage at a single photon level remain necessary before the principle of holographic memory can become practical for quantum information processing [Kub11].

4

Coupling electron spins to a microwave cavity

In the previous chapter, the multimode memory of microwave excitations in an ensemble of electron spins has been discussed. In order that the information transfer between the microwave photons and the electron spins can be coherent, the coupling between the two needs to be strong enough. In this chapter, I discuss the coupling of an electron spin ensemble to a three-dimensional microwave cavity under different conditions, and show that it is possible to reach the strong coupling with the parameters that are obtainable in EPR experiments.

4.1 Interaction between electron spins and photons

4.1.1 Kramers-Kronig relation

When the coupling between the electron spins and the resonator is weak, we are in the same parameter regime as the conventional CW EPR experiment [Wei07]. The dispersion and absorption components of the EPR signal are related to the real and imaginary parts of the complex magnetic susceptibility of the sample $\chi = \chi' + i\chi''$. χ' and χ'' are mathematically connected to each other by the *Kramers-Kronig relation*

$$\begin{aligned} \chi'(\omega) &= \chi'(\infty) + \frac{2}{\pi}\int_0^\infty \frac{\omega'\chi''(\omega')}{\omega'^2 - \omega^2} d\omega' \\ \chi''(\omega) &= -\frac{2\omega}{\pi}\int_0^\infty \frac{\chi'(\omega') - \chi'(\infty)}{\omega'^2 - \omega^2} d\omega'. \end{aligned} \tag{4.1}$$

This means that in an EPR experiment, the absorption spectrum, measured by the change in the cavity quality factor Q, and the dispersion spectrum, measured by the change in the cavity frequency are not independent: one can be computed from the other.

The EPR signal S (absorption spectrum) is proportional to the change in the Q factor during a sweep across resonance, i.e.

$$S \propto \frac{Q_u - Q_r}{Q_r} = \frac{Q_u}{Q_\chi} = Q_u \chi'' \eta, \tag{4.2}$$

where Q_u, Q_r are the Q factors off-resonance (unloaded) and on-resonance, $Q_\chi = \frac{\mu_0 \int_c H_1^2 dV}{\mu_0 \int_s \chi'' H_1^2 dV}$ describes the loss due to the sample at resonance, and η is the filling factor. On the other

hand, the frequency variation Δf during a sweep is related to the variation in the real part of the magnetic susceptibility $\Delta\chi'$ via

$$\Delta f = \frac{1}{2\lambda\sqrt{\mu\epsilon}}\frac{\Delta\chi'}{1+\chi'}, \tag{4.3}$$

where ϵ, μ are the permittivity and permeability of the sample, λ is the wavelength of the microwave fixed by the dimension of the cavity.

4.1.2 Vacuum Rabi splitting

When two oscillators are strongly coupled, their eigenmodes will mix with each other and generate new eigenmodes of the coupled system. The degeneracy is lifted, and an anticrossing will be observed in the spectrum [Bru96, Boc04, Wal04]. If one of the oscillators is a single atom consisting of a two-level structure, and the other is a single-mode field, the system can be described by the Jaynes-Cummings model Hamiltonian (in the rotating wave approximation)

$$\hat{H}_{\mathrm{JC}} = \hbar\omega_c\hat{c}^\dagger\hat{c} + \hbar\omega_a\frac{\hat{\sigma}_z}{2} + \hbar g(\hat{c}\hat{\sigma}_+ + \hat{c}^\dagger\hat{\sigma}_-), \tag{4.4}$$

where ω_c, ω_a are the cavity and atom resonance frequency, $\hat{c}^\dagger, \hat{c}$ are the creation and annihilation operators of the cavity photon, $\hat{\sigma}_\pm$ are the raising and lowering operator of the atom, $\hat{\sigma}_z$ is the inversion operator, and g denotes the atom-field coupling.

Solving the above Hamiltonian gives us the eigenvalues of the coupled system,

$$E_\pm(n) = \hbar\omega_c(n+\frac{1}{2}) \pm \frac{\hbar\sqrt{\delta^2+4g^2(n+1)}}{2}, \tag{4.5}$$

where $\delta = \omega_a - \omega_c$ is the detuning, n is the number of photons in the cavity mode. When $n = 0$, the difference between the two eigenvalues $E_+(0) - E_-(0) = 2g$ is twice the atom-field coupling strength. The phenomenon of the two eigenstates being split is called the *vacuum Rabi splitting* [Scu97].

In the case of a single electron spin and a photon, the interaction is via the dipolar coupling between the magnetic dipole moment of the spin and the magnetic field of the photon. The magnitude of this coupling can be estimated from the zero-point magnetic field

of a microwave photon. Suppose a single microwave photon trapped in a cavity of volume V_c, its zero-point energy is

$$E_0 = \frac{1}{2}\hbar\omega_c, \tag{4.6}$$

where ω_c is the resonant frequency of the cavity mode. On the other hand, this energy is stored in the electromagnetic field in the cavity, and if we assume the distribution of the field is uniform, we can estimate the energy of the field to be

$$2 \times \int \frac{B_0^2}{2\mu_0} dV \approx \frac{B_0^2 V_c}{\mu_0}, \tag{4.7}$$

where B_0 is the zero-point magnetic field, the factor of 2 in front of the integral at the left-hand side of the equation comes from the fact that only half of the energy of an electromagnetic field is stored in the magnetic field. Equation 4.6 and 4.7 together give

$$B_0 = \sqrt{\frac{\mu_0 \hbar \omega_c}{2V_c}}. \tag{4.8}$$

Therefore, the dipolar coupling between a single electron spin and a single photon is

$$g_s = \frac{m_0 B_0}{\hbar} = m_0 \sqrt{\frac{\mu_0 \omega_c}{2\hbar V_c}}, \tag{4.9}$$

where $m_0 = \mu_B g_e/2$ is the magnetic dipole moment of the electron spin.

4.1.3 Collective enhancement

Since the magnetic dipole moment of a single electron spin is small, its coupling to a single photon g_s is usually too weak to cause any splitting in the energy diagram. However the coupling strength can be greatly increased by making use of the phenomenon of collective enhancement, which has been discussed in Section 3.1.2. When a single photon interacts with an ensemble containing N electron spins, the Hamiltonian is similar to the one given in Equation 3.3 except that the last term describing the internal dynamics of the cavity does not appear here,

$$\begin{aligned} \hat{H} &= \hbar \sum_j g_{s,j} (\hat{s}_j^+ \hat{c} + \hat{s}_j^- \hat{c}^\dagger) = \hbar\sqrt{N} g_s (\hat{S}^+ \hat{c} + \hat{S}^- \hat{c}^\dagger) \\ &\equiv \hbar g_c (\hat{S}^+ \hat{c} + \hat{S}^- \hat{c}^\dagger). \end{aligned} \tag{4.10}$$

Here, $\hat{S}^{\pm} = \frac{1}{\sqrt{N}} \sum_j \hat{s}_j^{\pm}$ are the spin raising and lowering operators of the whole spin ensemble; The coupling strength $g_{s,j} = g_s$ is identical for each spin, and $g_c = \sqrt{N} g_s$ is the collectively enhanced coupling strength of the spin ensemble to a single photon [Her09, Fin09].

When the collective coupling strength g_c is strong compared to the spin decoherence rate γ and the cavity decay rate κ ($g_c > \gamma, \kappa$), the anticrossing in the spectrum will appear and the splitting equals to $2g_c$.

Since g_s scales with $1/\sqrt{V_c}$, an important way to increase the coupling strength is to use cavities with small mode volume. Coplanar stripline resonators [Bla04, Fru05] usually have a typical cavity volume of $V_c \sim d^2\lambda \sim 10^{-12}$ m^3, where $d \sim 10$ μm is the width of the cavity, $\lambda \sim 1$ cm is the wavelength of the microwave. Moreover, the high quality factor of superconducting cavities also makes them favorable for obtaining strong coupling strength. Experiments demonstrating the strong coupling of an electron spin ensemble to a superconducting transmission-line cavity have been carried out in some spin systems with large zero-field splitting such as Cr^{3+} color centers in Al_2O_3 [Sch10], NV^- centers in diamond [Kub10, Ams11] and Er^{3+} ions in YSO crystal [Bus11].

For the same reason, it will be more difficult to reach the same coupling strength with a three-dimensional resonator because its cavity volume is $V_c \sim \lambda^3 \sim 10^{-6}$ m^3 and the coupling strength will be $\lambda/d \sim 1000$ times weaker than a coplanar stripline cavity. On the other hand, a larger cavity volume also allows the cavity mode to interact with more spins, therefore in the end it is the ratio $\sqrt{N}/\sqrt{V_c}$ that affects the value of g_c. In the following I will show how we manage to observe anticrossings in the spectra signifying strong couplings of an electron spin ensemble to a 3D microwave resonator, and discuss the results in different parameter regimes.

4.2 Spins and cavities

In this section, I will describe the materials we used to study the coupling effect between electron spins and a microwave cavity.

4.2.1 Electron spin ensembles

DPPH powder

In order to have a large number of spins, we choose a material of high electron spin density, 2,2-diphenyl-1-picrylhydrazyl (DPPH) powder, a radical commonly used for field calibration of EPR spectrometers. From CW EPR measurements, the peak-to-peak spin linewidth of this material at room temperature is 2.1 G, which corresponds to a Gaussian full width at half maximum (FWHM) of 6 MHz. Several samples of different number of spins are prepared with $N_{\text{tot}} = 1.0 \times 10^{18}, 4.0 \times 10^{18}, 1.58 \times 10^{19}, 2.4 \times 10^{19}$, respectively. The number of polarized spins, which is the relevant N for the expressions described in the previous sections, is calculated from the Boltzmann distribution as the spin ensemble is in thermal equilibrium at room temperature,

$$N = N_{\text{tot}} \times (1 - e^{-\frac{\hbar\omega_c}{2k_B T}}). \tag{4.11}$$

Using $\omega_c = 2\pi \times 9.8$ GHz, $T = 300$ K, we have the number of polarized spins $N \approx 7.8 \times 10^{-4} \times N_{\text{tot}}$ which are $7.8 \times 10^{14}, 3.1 \times 10^{15}, 1.2 \times 10^{16}, 1.9 \times 10^{16}$.

Figure 4.1 shows the room temperature CW spectrum of the DPPH sample with $N = 3.1 \times 10^{15}$.

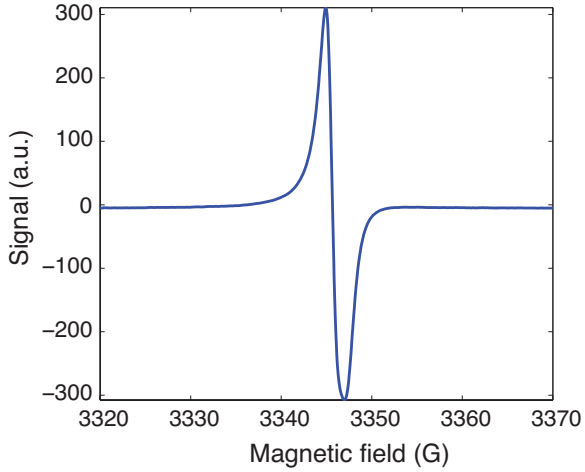

FIGURE 4.1: CW EPR spectrum of DPPH powder sample at room temperature. The peak-to-peak linewidth is 2.1 G.

x-form LiPc powder

The second material is x-form lithium phthalocyanine (LiPc) powder electrochemically prepared from dilithium phthalocyanine (Li_2Pc) [Ila00]. The EPR linewidth of this material is inversely related to the partial pressure of oxygen [Bri98b], therefore by evacuating the sample tube to 10^{-5} mbar, the peak-to-peak spin linewidth is reduced to about 83 mG at room temperature, which corresponds to a Gaussian FWHM of 0.24 MHz. The number of spins in different samples are $N_{\rm tot} = 1.0\times10^{17}, 1.3\times10^{17}, 1.9\times10^{17}, 2.85\times10^{18}$ and 9.5×10^{17}, corresponding to the number of polarized spins $N = 7.8\times10^{13}, 1.0\times10^{14}, 1.5\times10^{14}, 2.2\times10^{14}$ and 7.4×10^{14} at room temperature.

Figure 4.2 shows the room temperature CW spectrum of the LiPc sample with $N = 1.5\times10^{14}$.

All the spin counting measurements are carried out on an X-band CW EPR spectrometer (Bruker EMX), and are independent from the measurements of the spin-cavity coupling.

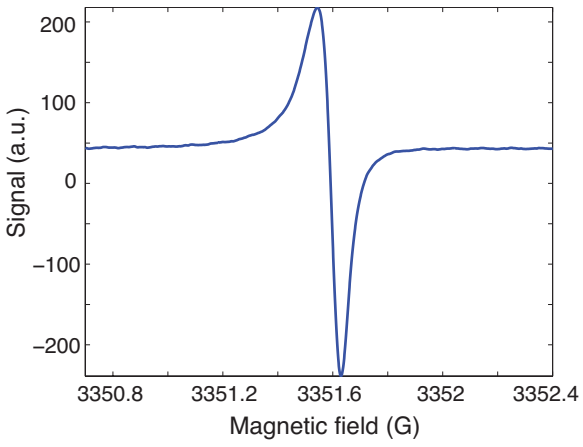

Figure 4.2: CW EPR spectrum of LiPc powder sample at room temperature. The peak-to-peak linewidth is 83 mG.

4.2.2 Microwave cavities

The microwave cavity we used in most of the following experiments is an X-band cylindrical dielectric ring resonator (Bruker, ER 4118X-MD5). This resonator has a wide range of unloaded Q factor from 200 to 6000 and is designed for both pulsed and CW EPR experiments. The cavity mode TE_{011} is confined within a cylindrical ring made of sapphire with diameter $d = 5$ mm and length of $l = 10$ mm. Therefore the cavity mode volume V_c of this resonator is about 0.2 cm^3. Although the microwave field distribution in the cavity is not uniform as assumed, we can still estimate the coupling strength of a single electron spin to the resonator using Equation 4.9, which gives $g_s \approx 0.06$ Hz.

To demonstrate the effect of the cavity volume on the coupling strength, we also used a second microwave cavity, an X-band standard rectangular resonator (Bruker, ER 4102ST). Its unloaded Q factor is about 6000 and is designed specially for CW experiment. The cavity operates in the TE_{102} mode, and its volume is about 1 cm $\times$ 3 cm $\times$ 4 cm $\approx$ 12 cm^3. A much larger V_c compared with the cylindrical resonator leads to a much weaker g_s, which means that with the same sample the collective coupling g_c will be much weaker in the rectangular resonator than in the cylindrical resonator. This is verified by our experiment shown later.

The reflection spectrum (S_{11}) from the resonator was measured with a network analyzer (HP 8722D), and only the magnitude of S_{11} ($|S_{11}|$) is discussed in the following. Note that there is about 8 dB loss on the coaxial cable connecting the VNA and the resonator, therefore all the spectra originally have a -16 dB baseline, which is subtracted before plotting them. As will be discussed later, in all the measurements the sample position inside the cavity was carefully adjusted to obtain a maximum coupling strength.

4.3 Weak coupling

In this section, I show that when the number of spins N is small, the coupling between the spin ensemble and the cavity is weak. Continuous variations in Q factor and cavity frequency ω as described in Section 4.1.1 are observed in the experiment.

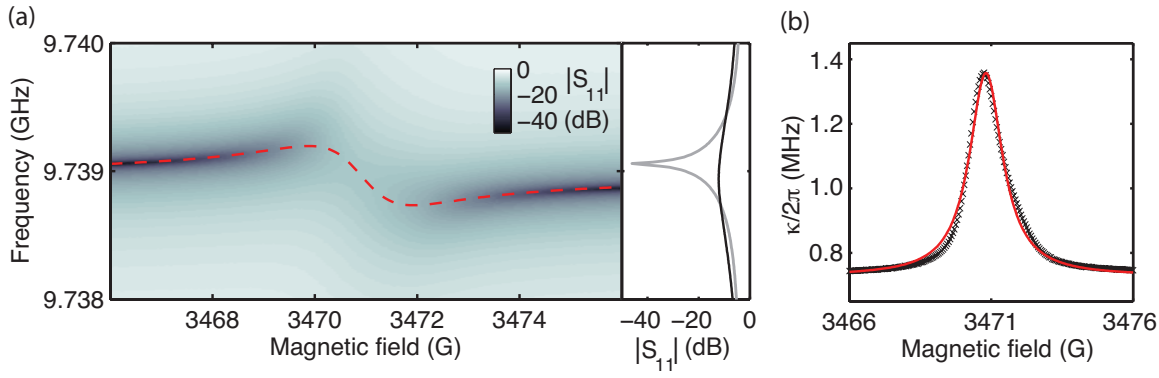

Figure 4.3: (a) Reflection spectrum for the DPPH powder sample with $N = 7.8 \times 10^{14}$ in the cylindrical resonator. The red dashed curve is the fit of the cavity frequency using Equation 4.12a. Right plot: off-resonance (grey, $B_0 = 3466$ G) and on-resonance (black, $B_0 = 3470.9$ G) spectra. (b) Cavity half linewidth as a function of magnetic field extracted from the spectrum (black cross), and the fit (red curve) using Equation 4.12b.

Figure 4.3 (a) shows the reflection spectrum for the DPPH sample with $N = 7.8 \times 10^{14}$ polarized spins in the cylindrical resonator. On the right of this figure two slices of the spectrum, at off-resonance (grey) and on-resonance (black), are shown. The cavity dip is much shallower and broader at the resonance due to the dissipation in the sample.

Modeling the spin ensemble and the resonator with two coupled oscillators, the changes in cavity frequency ω and cavity linewidth κ as a function of the magnetic field are described by the following equations [Her09]

$$\omega = \omega_c - \frac{g_c^2 \Delta}{\Delta^2 + \gamma_s^2}, \tag{4.12a}$$

$$\kappa = \kappa_c + \frac{g_c^2 \gamma_s}{\Delta^2 + \gamma_s^2}, \tag{4.12b}$$

where κ_c is the cavity half linewidth at far off-resonance, γ_s is the spin half linewidth, $\Delta = m_0(B - B_r)/\hbar$ is the field detuning. The red dashed line in Figure 4.3 (a) is a fit to the cavity dip positions using Equation 4.12a, which gives $g_c/2\pi = 1.15$ MHz and $\gamma_s/2\pi = 2.85$ MHz. A fit to the cavity linewidth using Equation 4.12b is shown in Figure 4.3 (b), which gives $g_c/2\pi = 1.12$ MHz, $\gamma_s/2\pi = 2.0$ MHz and $\kappa_c/2\pi = 0.73$ MHz. The value of g_c obtained from the two fits agree well. The two fitted γ_s slightly differ from each other, but both are consistent with the value from the CW measurement where the peak-to-peak linewidth of

2.1 G corresponds to $\gamma_s/2\pi = 3.0$ MHz.

It is apparent that in this parameter regime the coupling strength is small compared with the spin half linewidth ($g_c/\gamma_s \approx 0.32 < 1$), although on the other hand it is larger than the cavity half linewidth $g_c > \kappa_c$. This is the case that we often encounter in normal CW EPR experiments.

4.4 Strong coupling

With the cavity volume kept constant, the coupling strength increases as the number of spins in the ensemble is increased. In this section I show that when N is large enough, an anticrossing can be observed in the spectrum and the splitting scales as $\sqrt{N}$.

4.4.1 Observation of an anticrossing

As we increase N in the DPPH sample, the spectrum changes dramatically. When $N = 3.1 \times 10^{15}$ we start to observe two clearly separated dips at resonance. The splitting becomes larger as we keep increasing N. Figure 4.4 shows the spectrum for the sample with $N = 1.9 \times 10^{16}$ polarized spins. The dashed curves are the upper and lower branches of $\omega_\pm$, fitted using the equation for vacuum Rabi splitting

$$\omega_\pm = \omega_c + \frac{\Delta}{2} \pm \frac{\sqrt{\Delta^2 + 4g_c^2}}{2}. \tag{4.13}$$

The fit gives $g_c/2\pi = 5.9$ MHz, which is larger than the spin half linewidth $\gamma_s/2\pi = 3.0$ MHz.

The right panel of Figure 4.4 shows the sliced spectra at off-resonance (grey, $B_0 = 3465$ G) and on-resonance (black, $B_0 = 3470$ G). Two peaks are observed in the latter, which verifies that the sample is strongly coupled to the resonator.

Similar anticrossings are also observed in the spectra of the LiPc samples in the cylindrical resonator. An example with the sample of $N = 2.2 \times 10^{14}$ is shown in Figure 4.5. The fit using Equation 4.13 gives $g_c/2\pi = 0.71$ MHz, which is larger than the spin half linewidth of this sample, $\gamma_s/2\pi = 0.12$ MHz but smaller than the cavity half linewidth $\kappa_c/2\pi = 5.4$ MHz,

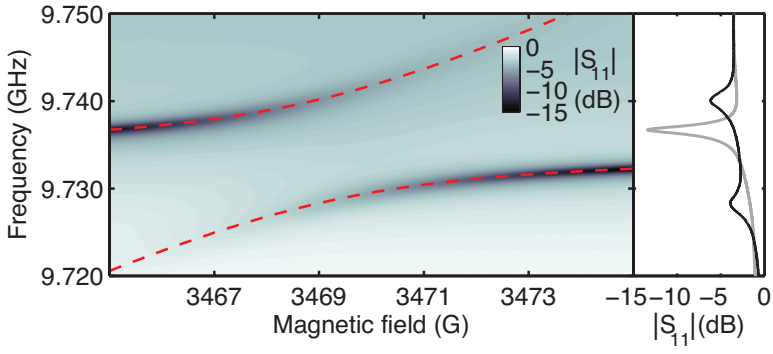

Figure 4.4: Reflection spectrum for the DPPH powder sample with $N = 1.9 \times 10^{16}$ in the cylindrical resonator. The red dashed curves are the fit of the eigen frequencies $\omega_{\pm}$ of the coupled cavity-spin system using Equation 4.13. Right plot: off-resonance (grey, $B_0 = 3465$ G) and on-resonance (black, $B_0 = 3469$ G) spectra.

experimentally obtained at far off-resonance. The right panel of Figure 4.5 shows the cavity spectra at off-resonance (grey, $B_0 = 3468$ G) and on-resonance (black, $B_0 = 3479.23$ G). The two dips are obvious in the on-resonance spectrum, although they are not fully separated due to the broad cavity linewidth.

Chiorescu *et al.* [Chi10] have recently made a similar observation on the strong coupling effect of an electron spin ensemble (DPPH) to a 3D microwave cavity, where they observed split peaks in the Fourier transformed ringing spectrum at resonance.

4.4.2 $\sqrt{N}$-dependence of collective coupling

The rule of collective enhancement as introduced in Section 4.1.3 is that the collective coupling g_c scales as the square-root of the number of polarized spins N in the ensemble. This is verified in our experiment by measuring the coupling strength for samples of different N.

In Figure 4.6, g_c is plotted against $\sqrt{N}$ for both DPPH and LiPc samples. Both plots show that the collective coupling follows the predicted relation $g_c = \sqrt{N} g_s$ quite well. From the linear fit we can also obtain g_s, the coupling strength of a single electron spin to the cavity, which is $g_s = 0.043$ Hz for DPPH and $g_s = 0.049$ Hz for LiPc. These results are consistent with the previous estimation using Equation 4.9, which was $g_s \approx 0.06$ Hz. The

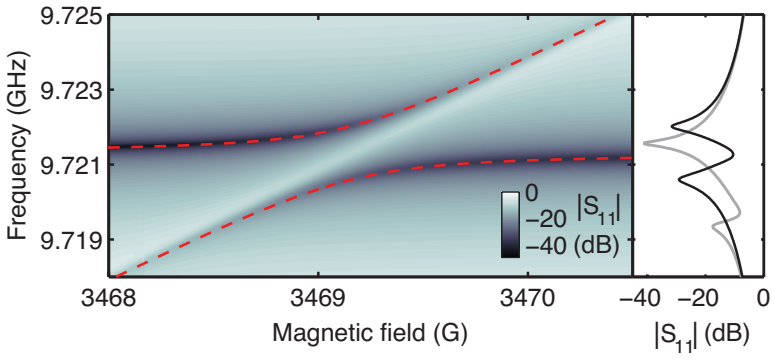

FIGURE 4.5: Reflection spectrum for the LiPc powder sample with $N = 2.2 \times 10^{14}$ in the cylindrical resonator. The red dashed curves are the fit of the eigen frequencies $\omega_{\pm}$ of the coupled cavity-spin system using Equation 4.13. Right plot: off-resonance (grey, $B_0 = 3468$ G) and on-resonance (black, $B_0 = 3469.15$ G) spectra.

discrepancy may arise from the inaccurate estimation of the filling effect of the sample.

In Figure 4.6 (a) the first data point ($\triangle$) corresponds to the DPPH sample with $N = 7.8 \times 10^{14}$ whose spectrum is shown in the Figure 4.3 and the coupling strength is calculated from Equation 4.12, and the other three data points ($\circ$) correspond to spectra containing an anticrossing and g_c are obtained from the fits using Equation 4.13. This means that although the sample for the first data point does not show splitting in its spectrum, its collective coupling strength extracted from Equation 4.12 still follows the $\sqrt{N}$-dependence.

In Figure 4.6 (b), the data point at $\sqrt{N} \approx 2.7 \times 10^7$ ($\square$) is for the LiPc sample with $N = 7.4 \times 10^{14}$ polarized spins. This point is not used for the fitting because in this case the sample volume V_s is very large compared with other samples, and the microwave field experienced by the sample is no longer uniform. If we estimate the distribution of the microwave field by measuring g_c of a sample with small V_s at different positions across the cavity, and fit the data with a sinusoidal function as is expected for the distribution of B_1 field in a cylindrical resonator (Figure 4.7), we can calculate the average coupling strength for the sample with $N = 7.4 \times 10^{14}$ to be $g_c/2\pi = 1.0$ MHz. This is reasonably close to the observed value of 0.9 MHz.

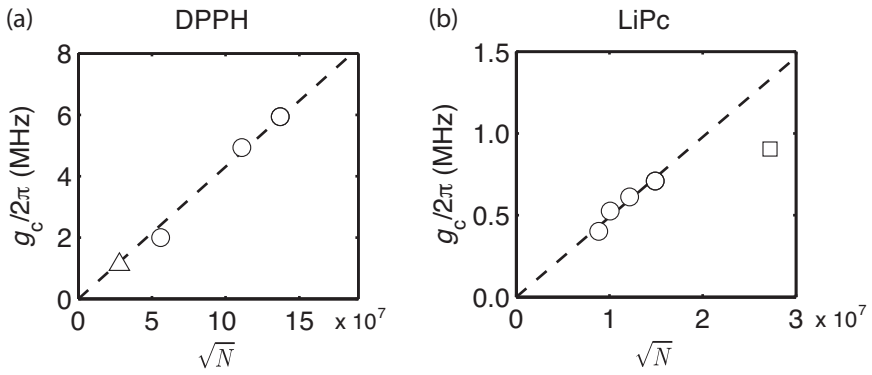

Figure 4.6: Collective coupling g_c as a function of $\sqrt{N}$ for (a) DPPH, (b) LiPc samples. The triangle ($\triangle$) in (a) represents the data for the DPPH sample with $N = 7.8 \times 10^{14}$ whose spectrum is shown in Figure 4.3. The square ($\square$) in (b) represents the data for the LiPc sample with $N = 7.4 \times 10^{14}$ whose volume is too large so that its coupling strength g_c deviates from the $\sqrt{N}$-dependence relation.

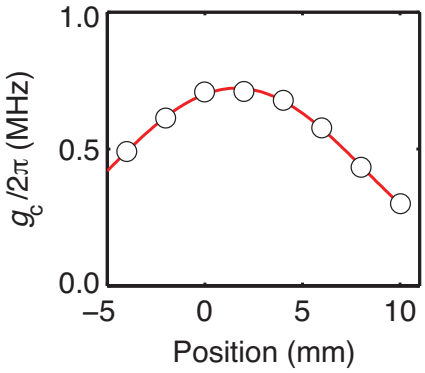

Figure 4.7: Coupling strength g_c as a function of the vertical position of the sample in the cylindrical resonator. The LiPc sample with $N = 2.2 \times 10^{14}$ is used in this measurement because its sample volume V_s is small enough that we can ignore the inhomogeneity of B_1 over V_s. The $x = 0$ reference point is taken for the maximum g_c. The red curve is a fit using a function of the form $g_c(x) \propto B_1(x) \propto \cos ax$.

4.4.3 Effect of cavity volume

When the number of spins of the sample is kept constant and the cavity volume is increased, the coupling strength decreases according to Equation 4.9. Figure 4.8 shows the spectrum of the DPPH sample with $N = 3.1 \times 10^{15}$ polarized spins in two different cavities, (a) the cylindrical resonator and (b) the rectangular resonator.

The fit in Figure 4.8 (a) using Equation 4.13 gives $g_c/2\pi = 2.4$ MHz. Even though the

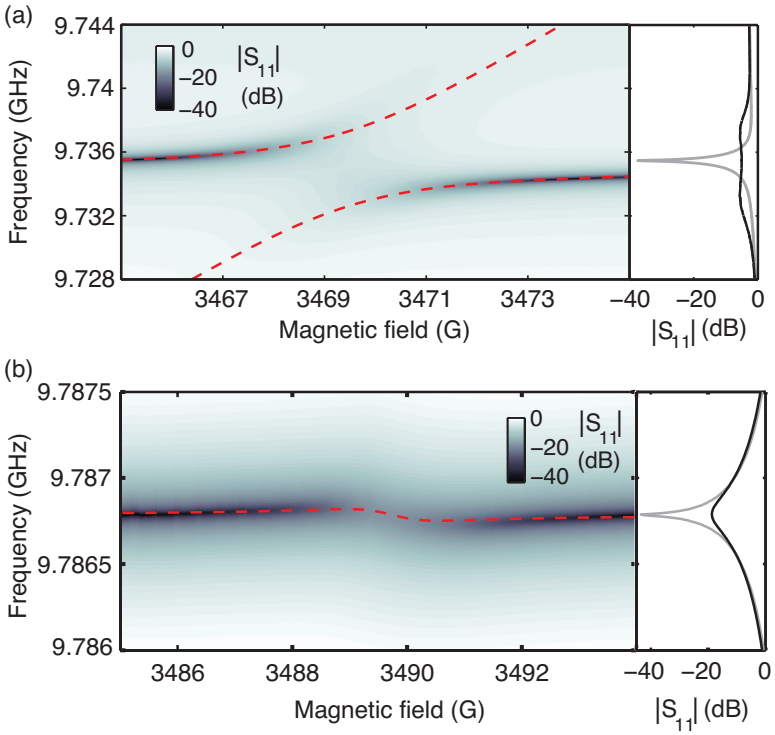

FIGURE 4.8: Reflection spectrum for the DPPH sample with $N = 3.1 \times 10^{15}$ in (a) cylindrical resonator ($V_c \approx 0.2$ cm^3), (b) rectangular resonator ($V_c \approx 12$ cm^3). The dashed red curves in (a) are fit using Equation 4.13, the one in (b) is the fit using Equation 4.12a. (a) Right plot: off-resonance (grey, $B_0 = 3465$ G) and on-resonance (black, $B_0 = 3469.5$ G) spectra. (b) Right plot: off-resonance (grey, $B_0 = 3485$ G) and on-resonance (black, $B_0 = 3489.6$ G) spectra.

coupling is less than the spin half linewidth $\gamma_s = 3.0$ MHz, we still observe a splitting in the spectrum at resonance (the condition for observing splittings is discussed later). Figure 4.8 (b) is fundamentally different to Figure 4.8 (a) that no splitting is observed in the spectrum, and the fit using Equation 4.12a gives $g_c/2\pi = 0.42$ MHz. The cylindrical and the rectangular resonators have similar unloaded Q_u that gives similar cavity half linewidth, $\kappa_{c,\mathrm{cyl}} = 1.0$ MHz, $\kappa_{c,\mathrm{rect}} = 1.4$ MHz. According to previous estimation on the cavity volume of the two resonators, $\sqrt{V_{c,\mathrm{rect}}/V_{c,\mathrm{cyl}}} \approx 7.7$, and this is approximately consistent with the experimentally measured coupling strength which gives $g_{c,\mathrm{cyl}}/g_{c,\mathrm{rect}} \approx 6$. This verifies that by varying the cavity volume V_c we can move from the strong coupling parameter regime to the weak coupling regime, and vice versa.

4.4.4 Effect of microwave power

The dependence of the collective coupling on the microwave power is also investigated. The output power level of the VNA is adjusted and the splitting of the spectrum at resonance is recorded for each power level. The experimental results show that the splitting, and therefore the collective coupling g_c, is independent of the microwave power as long as the sample is not saturated.

As an example, Figure 4.9 shows the on-resonance spectrum as a function of microwave power for the LiPc sample with $N = 7.8 \times 10^{13}$. It can be seen that for microwave power between -10 and -60 dBm the splitting between the dips is obvious and stays constant. For higher microwave power (between -5 and -10 dBm) the separation between the two dips gets shallower. This is because the sample becomes saturated in this power range, and the saturation will reduce the effective number of polarized spins N thus reduce the collective coupling g_c. The spectra for microwave power below -60 dBm became very scattered as the signal-to-noise ratios are low in this range, and it will be necessary to employ another experimental setup to measure at this or even lower power level.

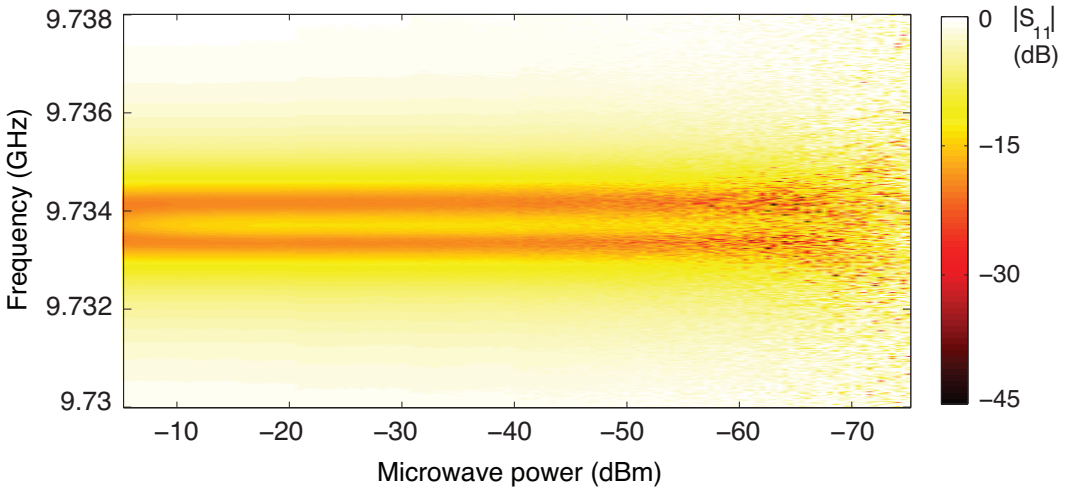

Figure 4.9: Reflection spectra at resonance as a function of the microwave power fed into the resonator. The sample used is the LiPc sample with $N = 7.8 \times 10^{13}$. The external field B_0 is kept constant and on-resonance during the power sweep.

4.5 Condition for observing anticrossing

We saw in Figure 4.8 (a) that with a collective coupling strength g_c smaller than the spin half linewidth γ_s, or in Figure 4.5 where g_c is larger than γ_s but much smaller than the cavity linewidth κ_c, it is still possible to observe the anticrossing in the spectrum. This is different from our expectation that anticrossing appears only in the strong coupling regime i.e. $g_c > \gamma_s, \kappa_c$. Therefore this leads us to an analytical study on the condition for observing anticrossing in the spectrum.

From a standard input-output formalism [Sch10], the reflection spectrum of a cavity loaded with electron spins can be calculated to be

$$|S_{11}|^2 = \left| 1 + \frac{\kappa_e}{i(\omega - \omega_c) - \kappa_c + g_c^2/(i\Delta - \gamma_s)} \right|^2 , \tag{4.14}$$

where κ_e is the external dissipation of the cavity. The validity of this equation is demonstrated by computing a spectrum with the following parameters, $g_c/2\pi = 0.71$ MHz, $\gamma_s/2\pi = 0.12$ MHz, $\kappa_c/2\pi = 5.4$ MHz and $\kappa_e = 0.99\ \kappa_c$ (Figure 4.10). The values for g_c, γ_s, κ_c are experimentally measured for the LiPc sample with $N = 2.2 \times 10^{14}$ (whose spectrum is shown in Figure 4.5), and the only adjustable parameter is κ_e. The computed spectrum reproduces well the experimental one.

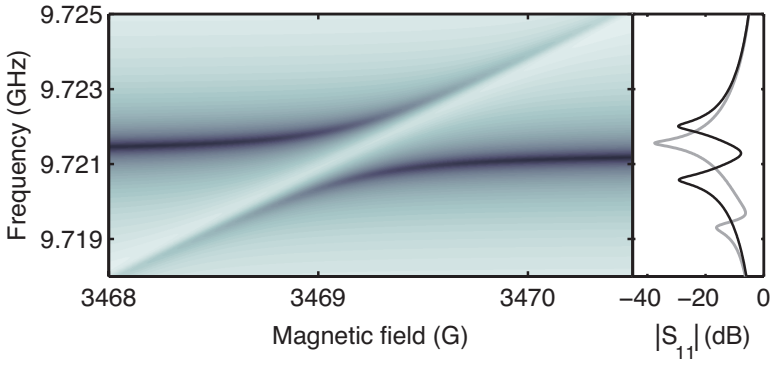

FIGURE 4.10: Simulation of the reflection spectra using Equation 4.14. Values for the parameters are $g_c/2\pi = 0.71$ MHz, $\gamma_s/2\pi = 0.12$ MHz, $\kappa_c/2\pi = 5.4$ MHz and $\kappa_e = 0.99\ \kappa_c$. Right plot: off-resonance (grey, $B_0 = 3468$ G) and on-resonance (black, $B_0 = 3469.15$ G) spectra.

Observing an anticrossing in the spectrum is equivalent to having two local minima in

$|S_{11}(\omega)|^2$ for Δ close to 0. Therefore, we can take the differential of Equation 4.14 with respect to ω at $\Delta = 0$ and if there exists more than one non-zero solution for the equation

$$\left.\frac{\partial|S_{11}|}{\partial\omega}\right|_{\Delta=0} = 0, \tag{4.15}$$

a splitting will appear in the spectrum. Taking the assumption that the cavity internal dissipation is small, i.e. $\kappa_c \approx \kappa_e$, Equation 4.15 is simplified to

$$\omega(\omega^4 + 2\gamma_s^2(2C+1)\omega^2 + \gamma_s^2(\gamma_s^2 - g_c^2)(2C+1) - g_c^4) = 0, \tag{4.16}$$

where $C = g_c^2/\gamma_s\kappa_c$, called the *cooperativity*, is a coefficient often used in the context of strong coupling ($C \gg 1$). Apart from the trivial solution $\omega = 0$, the other four solutions for Equation 4.16 are

$$\begin{aligned}\omega_{1,2}^2 &= -\gamma_s^2(2C+1) + \sqrt{\gamma_s^4(2C+1)^2 - \gamma_s^2(2C+1)(\gamma_s^2 - 2g_c^2) + g_c^4},\\ \omega_{3,4}^2 &= -\gamma_s^2(2C+1) - \sqrt{\gamma_s^4(2C+1)^2 - \gamma_s^2(2C+1)(\gamma_s^2 - 2g_c^2) + g_c^4}.\end{aligned} \tag{4.17}$$

Since C is always positive, $\omega_{3,4}$ are always imaginary. For the splitting to be observed, $\omega_{1,2}$ must be real, i.e. the condition

$$-\gamma_s^2(2C+1)(\gamma_s^2 - 2g_c^2) + g_c^4 > 0 \tag{4.18}$$

must be satisfied. This can be simplified to $g_c/\gamma_s > \sqrt{\sqrt{2}-1} \approx 0.64$ for κ_c large compared to g_c and γ_s, which is often the case for low Q 3D cavities. This implies that the splitting may be observable even if g_c is smaller than both γ_s and κ_c.

The condition is verified by the simulations shown in Figure 4.11. Here all parameters other than g_c have the same fixed value as used for Figure 4.10. By reducing g_c, we see that the two branches of $\omega_\pm$ (two red dashed curves in Figure 4.11 (a)) merge into one (red dashed curve in Figure 4.11 (b)) at $g_c/\gamma_s < 0.64$.

However, it is important to remember that the observation of anticrossing does not necessarily mean that the light-matter coherent information transfer is possible in this parameter regime. For the information transfer to be coherent, the condition $g_c \gg \gamma_s, \kappa_c$ remains a physical requirement.

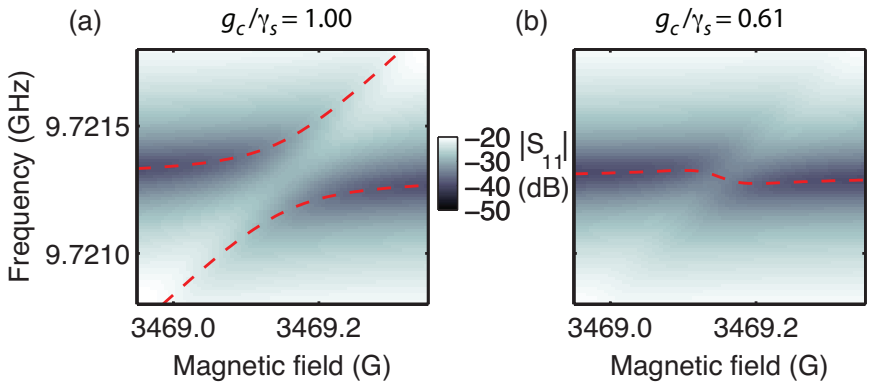

FIGURE 4.11: Simulation of reflection spectrum using $\gamma_s/2\pi = 0.12$ MHz, $\kappa_c/2\pi = 5.4$ MHz, $\kappa_e = 0.99\ \kappa_c$, and (a) $g_c = 0.12$ MHz, (b) $g_c = 0.085$ MHz. The dashed red curves are fits using Equation 4.13 and Equation 4.12a, respectively.

4.6 Conclusions

The coupling between an ensemble of electron spins and a three-dimensional microwave cavity is usually weak, where the variations in the magnetic susceptibility of the electron spins near resonance provide the necessary condition for conventional EPR measurements. By increasing the number of spins coupled to the cavity mode, it is possible to violate the conditions for weak coupling and get close enough to the strong coupling regime where the eigen modes of the electron spins and the cavity are mixed, and anticrossing can be observed in the cavity reflection spectrum. The coupling strengths, determined using the model of vacuum Rabi splitting, are found to depend on the square-root of the number of polarized spins, which is in agreement with the rule of collective enhancement. Numerical analysis shows that when cavity linewidth is broad, the level splitting is observable even if the coupling strength is smaller than the spin linewidth, which also agrees with the experimental data. These results provide possibilities for further studies on the spin-cavity dynamics on a macroscopic scale.

5

Adiabatic geometric phase gates

In EPR, the dynamic control of the electron spin states is realized by applying microwave pulses [Sch01], which usually contain non-negligible errors in both microwave amplitudes and phases [Mor05b]. Composite or shaped pulses are designed to correct these errors [Lev86, War88], among which BB1 pulse [Wim94, Mor05a] is a widely used composite pulse to compensate for the inhomogeneity in the microwave amplitude, and Knill pulse is another recently studied composite pulse scheme that is robust against off-resonance errors [Rya10, Sou11]. On the other hand, control of the electron spin states can also be achieved via adiabatic process where the eigenstates of the spin follow the evolution of the Hamiltonian of the system until reaching the target state [Jon00, Lee07, Fil09].

In this chapter, I demonstrate how to achieve single qubit operation — geometric phase gates — in electron spins via adiabatic control. In addition, comparisons between the adiabatic method and other phase gates using dynamic pulses are carried out in both simulation and experiment, which show that while the adiabatic geometric phase gate performs better than the dynamic phase gates, it has a comparable performance with the geometric phase gate realized with BB1 composite pulses.

5.1 Model

In this section, the model used for the adiabatic geometric phase gate is described. The Hamiltonian in the rotating frame and the driving microwave field are given, and the adiabatic condition is discussed.

5.1.1 Geometric phase

The model of the adiabatic geometric phase gate is constructed based on the idea of adiabatically driving a cyclic evolution of the electron spin, during which the spin will acquire a phase that depends only on the geometry of the curve traced out by the spin in the Bloch sphere [Ber84, Eke00].

Figure 5.1 illustrates the evolution of the spin eigenstate $|0\rangle$ (trace $\mathcal{C}_1$) and the effective

magnetic field B_{eff} (trace $\mathcal{C}_2$) during an adiabatic geometric phase gate of ϕ. The spin eigenstate $|0\rangle$ is initially aligned along the z-axis with the microwave detuned from resonance, then with the microwave slowly tuned onto resonance the instant eigenstate $|0(t)\rangle$ adiabatically follows the effective field B_{eff} and rotates into the xy plane; then the phase of the microwave is swept while keeping the spin on-resonance so that the spin eigenstate rotates in the xy plane to a certain angle ϕ; finally the microwave is tuned off-resonance again and the spin eigenstate goes back to its original position along the z-axis. The geometric phase acquired by the spin eigenstate $|0\rangle$ in this process is $\gamma_{|0\rangle} = \oint_{\mathcal{C}_1} \langle 0(t)|\mathrm{d}|0(t)\rangle$. For a spin-1/2 system, $\gamma_{|0\rangle}$ equals half of the solid angle enclosed by the curve $\mathcal{C}_1$, i.e. $\gamma_{|0\rangle} = \phi/2$. Similarly, the spin eigenstate $|1\rangle$ will trace out a curve in the opposite position to $\mathcal{C}_1$ on the Bloch sphere, which will result in a geometric phase $\gamma_{|1\rangle} = -\gamma_{|0\rangle} = -\phi/2$. Therefore, the geometric phase acquired by any superposition state will be the difference between the phases acquired by the two eigenstates, i.e. $\gamma = \gamma_{|0\rangle} - \gamma_{|1\rangle} = \phi$.

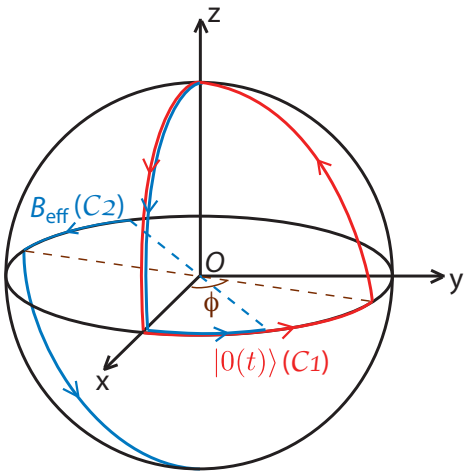

Figure 5.1: The effective magnetic field and the evolution of $|0\rangle$ during an adiabatic geometric phase gate in a Bloch sphere. The state $|0\rangle$ follows the red curve $\mathcal{C}_1$; the effective field follows the blue curve $\mathcal{C}_2$.

In addition to the geometric phase, the electron spin will also acquire a dynamic phase during the evolution, which is defined by

$$\delta = \int_0^{t_0} \frac{1}{\hbar} E(t)\mathrm{d}t = \int_0^{t_0} \frac{1}{\hbar} g\mu B(t) \cdot S\mathrm{d}t. \tag{5.1}$$

In order to remove this dynamic phase component from the phase of the final spin state, we introduce a π phase shift in the microwave field at the middle of the control sequence (indicated by the dashed blue line in Figure 5.1). When the spin has swept a phase of $\phi/2$ in the xy plane, B_{eff} is instantaneously flipped to the opposite direction, so that in the second half of the process the eigenstate of the spin is aligned in the opposite direction of B_{eff}. Therefore, the dynamic phases acquired by the spin state during the two halves of the adiabatic process have the same absolute value but opposite signs:

$$\begin{aligned} \delta_1 &= \int_0^{t_0/2} \frac{1}{\hbar} g\mu B_{\text{eff}}(t) S \mathrm{d}t, \\ \delta_2 &= -\int_{t_0/2}^{t_0} \frac{1}{\hbar} g\mu B_{\text{eff}}(t) S \mathrm{d}t = -\delta_1. \end{aligned} \tag{5.2}$$

By the end of the adiabatic process the dynamic phase will cancel out, i.e. $\delta = \delta_1 + \delta_2 = 0$.

5.1.2 Hamiltonian in the rotating frame

The off-resonance effect of the microwave, i.e. the z component in the effective field B_{eff} can be created either by adding an offset to the static field B_0 or by tuning the frequency of the microwave off-resonance. As the length of the adiabatic process is within a few microseconds, it is much easier to tune the microwave frequency via modulation than to vary the static field in this timescale.

When the microwave frequency $\omega(t)$ is time-dependent, the transformation of the Hamiltonian from the lab frame to the rotating frame can be done in two ways: using a rotating frame of constant frequency $\omega_{\text{rf}} = \omega_0$ at which the spin is on-resonance, or using a rotating frame that always keeps the same the frequency as the driving microwave field $\omega_{\text{rf}} = \omega(t)$. In the first case, the transformed Hamiltonian in the rotating frame is

$$\hat{H} = \begin{pmatrix} 0 & \frac{1}{2}e^{it\Delta}(\Omega_x - i\Omega_y) \\ \frac{1}{2}e^{-it\Delta}(\Omega_x + i\Omega_y) & 0 \end{pmatrix}, \tag{5.3}$$

where Ω_x, Ω_y are the amplitude of the microwave field along both directions, $\Delta(t) = \omega(t) - \omega_0$ is the time-dependent detuning. In the second case, the Hamiltonian in the rotating frame

is

$$\hat{H} = \begin{pmatrix} \frac{1}{2}(\Delta + t\dot{\Delta}) & \Omega_x - i\Omega_y \\ \Omega_x + i\Omega_y & -\frac{1}{2}(\Delta + t\dot{\Delta}) \end{pmatrix}. \tag{5.4}$$

The two Hamiltonians, though having different forms, are equivalent and will cause the same spin evolution. In our numerical simulation the second form is used, as in this case the measurement of spin magnetization is carried out automatically in the same reference frame as the one used for plotting Figure 5.1.

5.1.3 Driving microwave field

The microwave field that can drive the adiabatic geometric phase gate of the electron spin is not unique. Any field that evolves adiabatically along the curve $\mathcal{C}_2$ in Figure 5.1 will be able to induce a geometric phase ϕ to the spin. For the purpose of simplicity, we suppose that the whole adiabatic process is divided in four sections of the same duration τ: the frequency sweep from off-resonance to on-resonance, the phase sweep in the xy plane from 0 to $\phi/2$ before the π phase shift in B_{eff}, the phase sweep from $\phi/2$ to ϕ after the π phase shift, and the frequency sweep from on-resonance to off-resonance. Specifically, the conditions that the driving field must satisfy are:

$$\Omega_x(0) = \Omega_y(0) = 0,\ \Omega_x(4\tau) = \Omega_y(4\tau) = 0; \tag{5.5a}$$

$$\Delta(t) = 0,\ \text{for any } \tau \le t \le 3\tau; \tag{5.5b}$$

$$\Delta(t) + t\dot{\Delta}(t) = 0,\ \text{for } t = \tau \text{ and } 3\tau. \tag{5.5c}$$

Equation 5.5c comes from the requirement for adiabaticity that the Hamiltonian of the system should be continuous at the moment of $t = \tau, 3\tau$ and $\Delta + t\dot{\Delta} = 0$ for any $\tau < t < 3\tau$.

In addition, to realize the π phase shift of the driving field at $t = 2\tau$, there needs to be another constraint on the driving field

$$\Delta(t) = \Delta(4\tau - t),\ \text{for any } 2\tau \le t \le 4\tau. \tag{5.6}$$

Ω_x, Ω_y should also be defined in a similar way in order to make sure that the dynamic phase

acquired during $0 < t < 2\tau$ will be cancelled out during the period of $2\tau < t < 4\tau$ and Equation 5.2 is satisfied.

Frequency

One valid specification of the frequency of the driving microwave field that satisfies Equation 5.5b, 5.5c and 5.6 is

$$\omega_r(t) = \begin{cases} \omega_0 - \Delta_0 \cdot [t - \tau + \frac{\tau}{\pi}\sin(\pi\frac{t}{\tau})]/2(t+\delta) & 0 \le t < \tau, \\ \omega_0 & \tau \le t < 2\tau, \\ \omega_r(4\tau - t) & 2\tau \le t \le 4\tau. \end{cases} \tag{5.7}$$

Here $\Delta_0 = \omega_r(0) - \omega_0$ denotes the initial detuning at $t = 0$, δ is a shift in the time axis in order to avoid the divergence brought by the $1/t$ term around $t = 0$. Figure 5.2 shows $\Delta(t)/\Delta_0$ and $(\Delta(t) + t\dot{\Delta}(t))/\Delta_0$ (equivalent to the energy level splitting) for $\delta = \tau/2$.

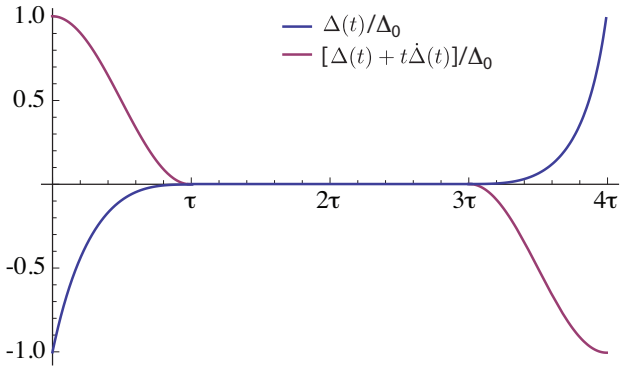

FIGURE 5.2: The detuning Δ and the energy level splitting $\Delta + t\dot{\Delta}$ as a function of time. The frequency of the microwave is specified by the detuning $\omega_r(t) = \omega_0 - \Delta(t)$ such that the energy splitting of the spin state (i.e. the diagonal elements of the Hamiltonian) is antisymmetric with respect to $t = 2\tau$.

Amplitude

Naïvely, one might attempt the following as the amplitude of the driving microwave field, in both x and y directions,

$$\Omega_x(t) = \begin{cases} \Omega_0 \frac{t}{\tau} & 0 \le t \le \tau, \\ \Omega_0(1 - \frac{t-\tau}{\tau}) & \tau < t < 2\tau, \\ \Omega_0 \frac{t-2\tau}{\tau} & 2\tau \le t \le 3\tau, \\ \Omega_0(1 - \frac{t-3\tau}{\tau}) & 3\tau < t < 4\tau; \end{cases} \tag{5.8}$$

$$\Omega_y(t) = \begin{cases} 0 & 0 \le t \le \tau, \\ \Omega_0 \frac{t-\tau}{\tau} & \tau < t < 2\tau, \\ -\Omega_0(1 - \frac{t-2\tau}{\tau}) & 2\tau \le t \le 3\tau, \\ 0 & 3\tau < t < 4\tau. \end{cases} \tag{5.9}$$

However, upon further consideration, the requirement for adiabaticity implies that apart from the Hamiltonian itself being continuous in time, the first derivative of the Hamiltonian with respect to time must also be continuous. Therefore, "smooth" functions should be used as the amplitude of the driving field:

$$\Omega_x(t) = \begin{cases} \Omega_0(1 - \cos(\frac{t}{\tau}\pi))/2 & 0 \le t \le \tau, \\ \Omega_0 \cos[\frac{\phi}{2} \cdot (1 + \cos(\frac{t}{\tau}\pi))/2] & \tau < t < 2\tau, \\ -\Omega_0 \cos[\frac{\phi}{2} \cdot (3 - \cos(\frac{t}{\tau}\pi))/2] & 2\tau \le t \le 3\tau, \\ -\Omega_0 \cos\phi \cdot (1 - \cos(\frac{t}{\tau}\pi))/2 & 3\tau < t < 4\tau; \end{cases} \tag{5.10}$$

$$\Omega_y(t) = \begin{cases} 0 & 0 \le t \le \tau, \\ \Omega_0 \sin[\frac{\phi}{2}(1 + \cos(\frac{t}{\tau}\pi))/2] & \tau < t < 2\tau, \\ -\Omega_0 \sin[\frac{\phi}{2}(3 - \cos(\frac{t}{\tau}\pi))/2] & 2\tau \le t \le 3\tau, \\ -\Omega_0 \sin\phi \cdot (1 - \cos(\frac{t}{\tau} \cdot \pi))/2 & 3\tau < t < 4\tau. \end{cases} \tag{5.11}$$

As will be demonstrated later by the numerical simulation, the adiabatic process using the driving field with continuous time derivative offers more accurate phase operation than

the non-continuous one. The two profiles of the amplitude of the driving field for a particular phase $\phi = \pi$ are plotted in the Figure 5.3.

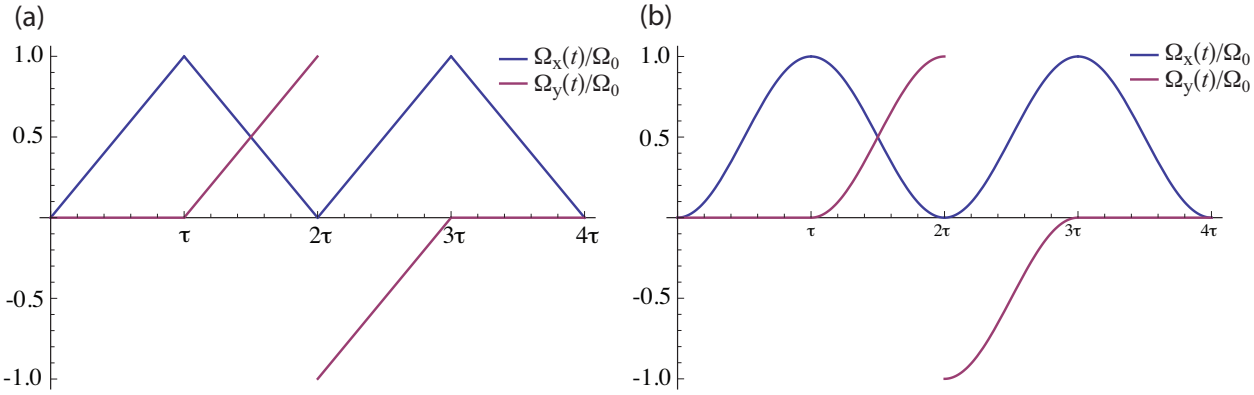

FIGURE 5.3: (a) The amplitude of the microwave field with discontinuous time derivative, defined by Equation 5.8 and 5.9. (b) The amplitude of the microwave field with continuous derivative, defined by Equation 5.10 and 5.11. Here $\phi = \pi$ for both plots.

Figure 5.4 shows an example of simulation for the time evolution of the spin magnetization during an adiabatic π phase gate. The initial spin state is $|0\rangle$, and its evolution follows the trace $\mathcal{C}_1$ in the Figure 5.1. The small wiggles in the simulated spectra are due to the non-adiabaticity of the driving field, and they grow smaller if the adiabatic phase gate is carried out more slowly or at a stronger microwave field.

5.1.4 Adiabatic conditions

To ensure adiabaticity, the evolution of the whole system should be slow enough such that the spin follows the effective magnetic field [Kat50], which means that each adiabatic passage should be much longer than the precession period of the spin, i.e. $\tau \gg \Delta_0^{-1}$. Although a longer τ helps to guarantee the adiabaticity, it also reduces the general effectiveness of the gate, for example when taking spin decoherence into account. Generally, $\tau \sim 10\Delta_0^{-1}$ is a reasonable compromise between the two constraints.

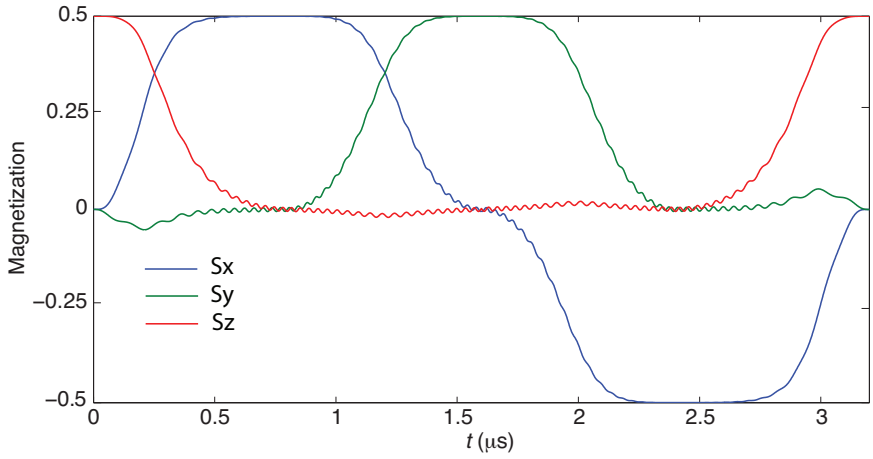

FIGURE 5.4: Spin magnetization during an adiabatic geometric phase gate of π. S_x, S_y, S_z are measured in a rotating frame that has the same frequency as the microwave field. The parameters used in this simulation are $\tau = 800$ ns, $\Omega_0 = 10$ G, $\Delta_0 = 10$ MHz.

An analytical study of the time evolution of the eigenstate of the Hamiltonian (Equation 5.4) gives the following requirement on the adiabatic condition:

$$\Delta(t) + t\dot{\Delta}(t) + \frac{-\Omega_y(t)\dot{\Omega}_x(t) + \Omega_x(t)\dot{\Omega}_y(t)}{\Omega_x^2(t) + \Omega_y^2(t)} \ll \sqrt{\Delta^2 + \Omega_x^2 + \Omega_y^2}. \tag{5.12}$$

This requires that the Rabi frequency of the adiabatic control field should be much larger than the detuning, i.e. $\Omega_0 \gg \Delta_0$. On the other hand, the left-hand side of Equation 5.12 contains the time-derivative of Ω_x and Ω_y, which means that the inequality holds on condition that Ω_x, Ω_y do not vary too fast with time. Therefore, for a certain τ, i.e. a reasonable length of the adiabatic control sequence, Ω_0/τ is limited by this requirement.

5.2 Numerical simulations

In this section, I show the results of the numerical simulation using the model described in the previous section. The robustness of the adiabatic geometric phase gate is tested under different circumstances, and its performance is compared with other dynamic phase operations.

5.2.1 Continuity of the driving field

Previously in the discussion about the profile of the driving microwave field we have stated that the adiabatic process should have a higher fidelity when the amplitude and frequency of the microwave field has a continuous first derivative with respect to time. This is verified in the simulation by comparing the performance of a π phase gate with the two different amplitude profiles of the microwave field shown in Figure 5.3.

In the simulation, assuming the initial spin state is σ_x, then the phase acquired by the spin after applying a Z phase gate can be calculated from the projection of the spin magnetization of the final state in the xy plane, i.e. $\gamma = \arctan(S_y/S_x)$.

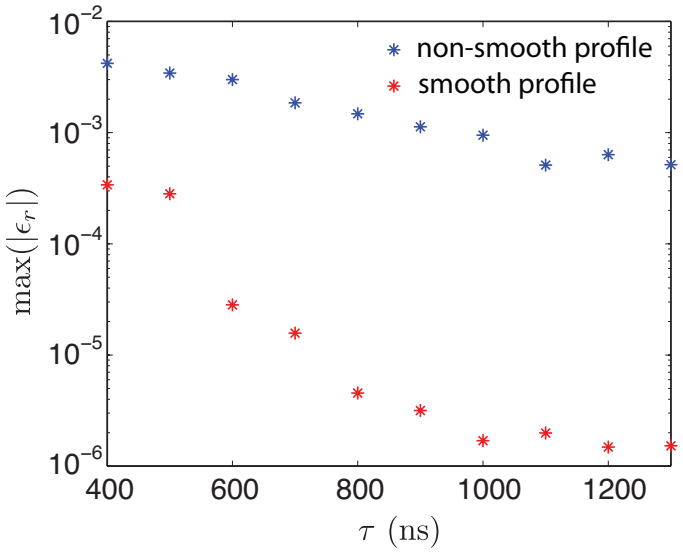

FIGURE 5.5: Maximum of the magnitude of relative phase errors for an adiabatic π phase gate simulated at Ω_0 between 4 G and 32 G as a function of the length of the adiabatic control sequence ($T_{\text{ad}} = 4\tau$). The non-smooth and smooth profiles of the driving microwave field are defined in Figure 5.3 (a) and (b).

Figure 5.5 shows the maximum of the relative errors in phase $\epsilon_r = (\gamma - \pi)/\pi$ against τ for both smooth and non-smooth amplitude. The length of the adiabatic passage is varied from $4\tau = 1600$ ns to 5200 ns, and for each τ the amplitude of the microwave Ω_0 is varied from 4 G to 32 G. The results show that using the smooth amplitude profile the relative phase error is always within 4×10^{-6} for all $\tau \geq 800$ ns. This falls below the generally tolerable error

rate for reliable quantum computing [Ste99, Bac06, Ali07]. Using the non-smooth amplitude ϵ_r reaches below 1×10^{-3} only for $\tau \geq 1000$ ns. Figure 5.5 also implies that with either profile of amplitude, the phase gate performs better with a longer τ. This agrees with the expectation because one gets closer to the adiabatic limit by applying a longer adiabatic operation.

Based on these considerations, the smooth profile of the microwave amplitude and $\tau \geq 800$ ns are always used in the following simulations to meet the requirement of the adiabatic condition.

5.2.2 Inhomogeneities in microwave field

Ideally, the geometric phase obtained in an adiabatic process should be immune to inhomogeneities in the amplitude of the microwave field, because variations in the amplitude of the microwave field will not affect the trajectory of the effective magnetic field during the adiabatic process, and this is the main advantage of the adiabatic operation over conventional dynamic spin operations. The simulations show that when the adiabatic condition is satisfied, i.e. τ and Ω_0 are large enough, the amplitude of the microwave field (Ω_0) has little effect on the final geometric phase obtained by the spin over a very broad range of Ω_0.

Figure 5.6 shows the relative error ϵ_r in the geometric phase γ acquired by the spin after a π phase gate. It can be seen that the maximum relative error is less than 2×10^{-6} for Ω_0 between 4 G and 32 G, which corresponds to an error in phase of less than $\pm 0.0004°$. Meanwhile, the variation in ϵ_r is smaller for longer τ and stronger Ω_0, which means that the phase operation is more accurate when the adiabatic phase operation is carried out more slowly and with a stronger driving microwave field. This tendency is consistent with the requirement of the adiabatic conditions.

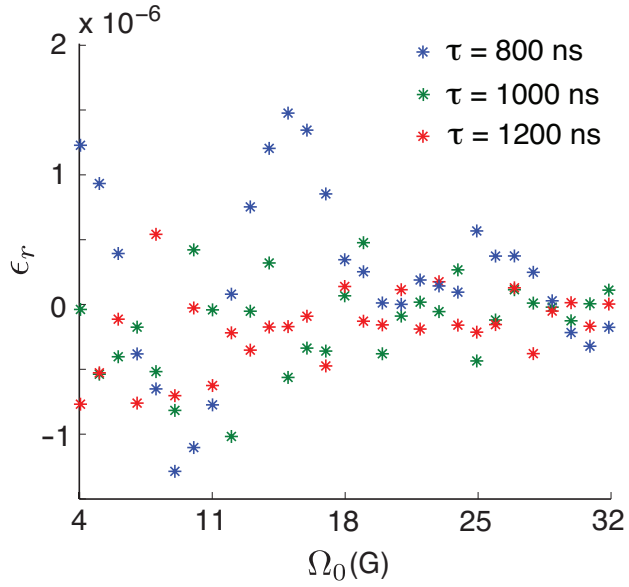

FIGURE 5.6: Relative phase error for an adiabatic geometric π phase gates simulated at different microwave amplitude. Ω_0 is varied from 4 G to 32 G.

5.2.3 Fast fluctuations in static field

The adiabatic geometric phase gate is predicted to be robust against high frequency noise ($\nu_{\mathrm{n}} \gg 1/\tau$) in the external static field [Lup09] because the phase of the gate depends only on the geometry of the cyclic evolution of the Hamiltonian which is a slow (adiabatic) process, while the effect of the high frequency noise in the static field will be averaged out over the whole process. In the simulation the noise is modelled as a fluctuation in the static field that varies for every Δt. Figure 5.7 shows the relative errors in the obtained geometric phases after an adiabatic π phase gate under noises of different frequency, i.e. different $\nu_{\mathrm{n}} = 1/\Delta t$.

When the fluctuation is varying more rapidly than every 10 ns ($\nu_{\mathrm{n}} \geq 100$ MHz), the relative error in the adiabatic phase remains lower than the threshold of quantum error correction 1.94×10^{-4} [Ali07]. This verifies that the geometric phase gate is robust against noises of high frequency.

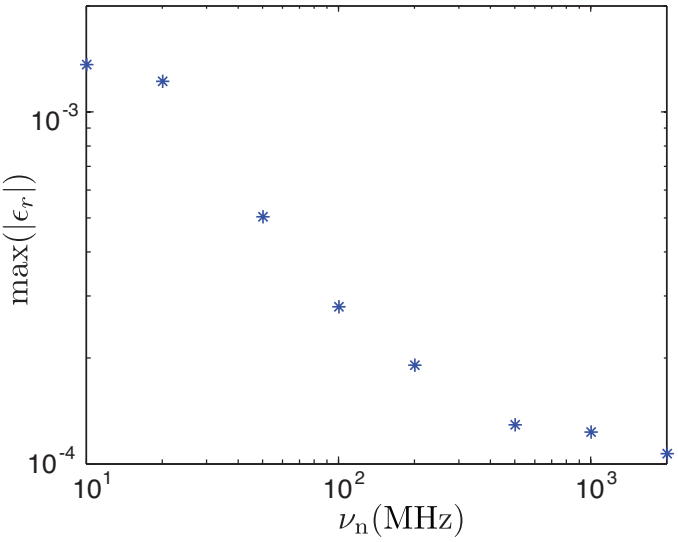

Figure 5.7: Error rate of the adiabatic phase gate under noises of different frequency. The parameters used in the simulation are $\Omega_0 = 5$ G, $\tau = 800$ ns. The amplitude of the fluctuation in Ω_0 is $\Delta\Omega_{0,\max} = 1$ mG.

5.2.4 Comparison with phase gates using dynamic pulses

Dynamic phase gates

The dynamic pulse sequence to realize a rotation of ϕ along the z-axis is

$$(\frac{\pi}{2})_x - (\phi)_y - (\frac{\pi}{2})_{-x}. \tag{5.13}$$

Each of the three dynamic pulses can be replaced by a BB1 composite pulse for better performance given an inhomogeneous microwave field. The general definition of a BB1 composite pulse for an arbitrary microwave pulse of flipping angle θ and phase ψ (noted as θ_ψ) is

$$(\theta)_\psi(\pi)_{\psi+\phi_1}(2\pi)_{\psi+\phi_2}(\pi)_{\psi+\phi_1}, \tag{5.14}$$

where $\phi_1 = \arccos(-\theta/4\pi), \phi_2 = 3\phi_1$. Therefore the complete BB1 composite pulse sequence for a π phase gate is

$$\begin{aligned} & (\frac{\pi}{2})_0(\pi)_{\phi_1}(2\pi)_{\phi_2}(\pi)_{\phi_1} \\ - \quad & (\pi)_{\frac{\pi}{2}}(\pi)_{\phi_3+\frac{\pi}{2}}(2\pi)_{\phi_4+\frac{\pi}{2}}(\pi)_{\phi_3+\frac{\pi}{2}} \\ - \quad & (\frac{\pi}{2})_{\pi}(\pi)_{\phi_1+\pi}(2\pi)_{\phi_2+\pi}(\pi)_{\phi_1+\pi}, \end{aligned} \tag{5.15}$$

where $\phi_1 = 1.70, \phi_2 = 5.09, \phi_3 = 1.82, \phi_4 = 5.47$.

Geometric phase gates

It is also possible to build a geometric phase gate by applying two π pulses of different phase successively

$$(\pi)_{\psi_1} - (\pi)_{\psi_2}. \tag{5.16}$$

During this pulse sequence the spin eigenstates invert along one of the lines of longitude of the Bloch sphere during the first π pulse, then invert again to return to their original position via another line of the longitude of the Bloch sphere. The phase acquired by the spin eigenstates is determined by the solid angle enclosed by the trace of the spin magnetization, i.e. the difference of the phase of the two π pulse. Therefore the geometric phase acquired by a spin superposition state during this geometric phase gate is $\gamma = 2(\psi_2 - \psi_1)$. Supposing the first π pulse to be along the x-axis, i.e. $\psi_1 = 0$, the geometric phase is then $\gamma = 2\psi_2$.

Replacing each π pulse in Equation 5.16 with a BB1 composite pulse, the BB1 pulse sequence for a geometric phase gate of phase γ is

$$(\pi)_0(\pi)_{\phi_1}(2\pi)_{\phi_2}(\pi)_{\phi_1} - (\pi)_{\gamma/2}(\pi)_{\phi_1+\gamma/2}(2\pi)_{\phi_2+\gamma/2}(\pi)_{\phi_1+\gamma/2}, \tag{5.17}$$

where $\phi_1 = 1.82, \phi_2 = 5.47$.

Comparison under microwave inhomogeneity

The phases obtained by the two different phase gates using dynamic pulses are compared with the adiabatic geometric phase gates for a π phase gate, as a function of the deviation

from a certain microwave amplitude $\Delta\Omega_0/\Omega_0$ (Figure 5.8 (a)). The maximum deviation of Ω_0 from its center value is set to $\pm 10\%$, which is the empirical value for the inhomogeneity of the microwave field in EPR spectrometers. The results show that the phase error in the BB1 pulsed dynamic phase gate is much larger than the other geometric phase gates. Actually, the relative phase error has a third order dependence on the error in microwave amplitude for the BB1 dynamic phase gate, i.e. $\epsilon_{r,\mathrm{dyn}} \sim O((\Delta\Omega_0/\Omega_0)^3)$, whereas it has a sixth order dependence for the BB1 geometric phase gate, i.e. $\epsilon_{r,\mathrm{geo}} \sim O((\Delta\Omega_0/\Omega_0)^6)$. The relative phase error in the adiabatic geometric phase gate is comparable with the BB1 geometric phase gate in this range of microwave inhomogeneity, as shown in the figure. On the other hand, we can see that if the microwave inhomogeneity is much worse than 10%, as is the case in most coplanar cavities, the adiabatic passage will have advantages over BB1 geometric phase gate in its robustness against such large inhomogeneities.

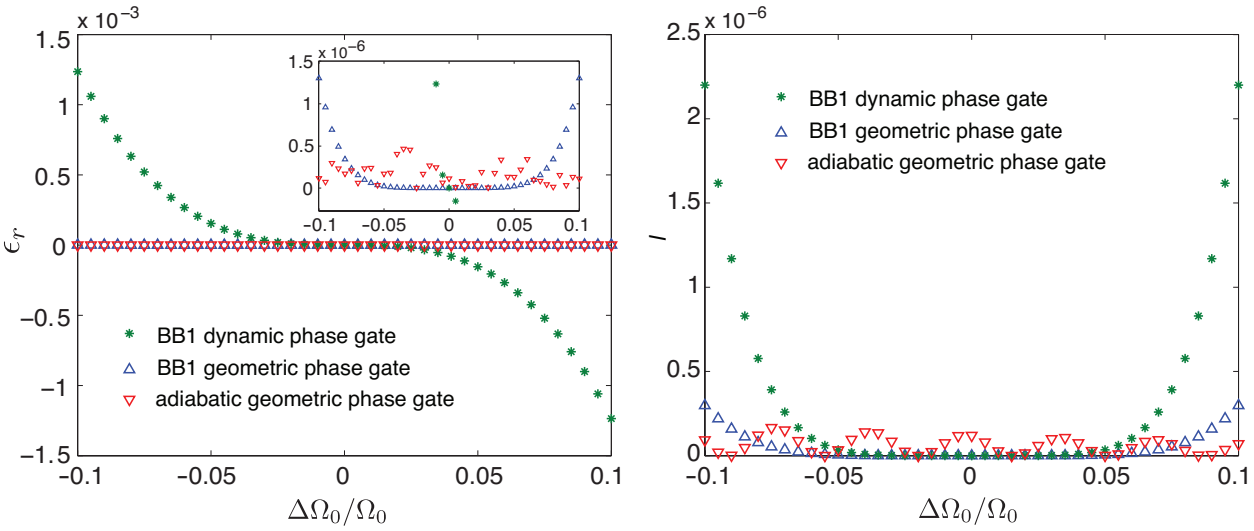

Figure 5.8: (a) The relative phase errors of an adiabatic geometric π phase gate, dynamic and geometric π phase gates using BB1 pulses as a function of the error in microwave amplitude $\Delta\Omega_0/\Omega_0$. (b) The infidelity of the phase gate operations as a function of $\Delta\Omega_0/\Omega_0$. The parameters used for the simulation are $\Omega_0 = 5$ G, $\tau = 1000$ ns. The length of the nominal π-pulse in the BB1 pulse sequence is 112 ns.

To describe the phase operation completely, the corresponding operator is studied. The

operator for an ideal rotation of θ along the z-axis is

$$U_0(\theta_z) = \begin{pmatrix} e^{i\theta/2} & 0 \\ 0 & e^{-i\theta/2} \end{pmatrix}. \tag{5.18}$$

Therefore, the operator for an ideal π phase gate is

$$U_0(\pi_z) = \begin{pmatrix} i & 0 \\ 0 & -i \end{pmatrix}. \tag{5.19}$$

The operator for a real, non-ideal phase gate is denoted as

$$U = \begin{pmatrix} u_{11} & u_{12} \\ u_{21} & u_{22} \end{pmatrix}, \tag{5.20}$$

where its elements can be determined by the final states of the phase operation starting from the two initial eigenstates $|0\rangle = (1,0)^{\mathrm{T}}, |1\rangle = (0,1)^{\mathrm{T}}$, using the relation

$$U|0\rangle = (u_{11}, u_{12})^{\mathrm{T}},\ U|1\rangle = (u_{21}, u_{22})^{\mathrm{T}}. \tag{5.21}$$

The quality of a phase gate U can also be described by the infidelity of the gate operation, defined as

$$I = 1 - F = 1 - \frac{|\mathrm{Tr}[UU_0^{-1}]|}{2} = 1 - \frac{|u_{11}\cdot(-i) + u_{22}\cdot i|}{2}. \tag{5.22}$$

The infidelity of the three different phase gates are plotted as a function of $\Delta\Omega_0/\Omega_0$ in Figure 5.8 (b). For the two phase gates using BB1 composite pulses, the infidelity increases as $O((\Delta\Omega_0/\Omega_0)^6)$. The difference in the infidelity between the BB1 dynamic phase gate and the other two phase gates is smaller than in the phase error, and this is because in the measurement of infidelity only the diagonal elements of U and U_0 are compared while the phase error ϵ_r is more directly related to the off-diagonal elements of U. The oscillations in the infidelity for the adiabatic phase gate are due to the non-adiabaticity of the operation, which is unavoidable but has little effect on the geometric phase we measured. Again, we see that the infidelity of the BB1 geometric phase gate is comparable with the adiabatic phase gate within $\pm 10\%$ microwave inhomogeneity, yet the adiabatic phase gate will have a better quality when the microwave inhomogeneity gets worse.

5.3 Experimental demonstration

In this section, I demonstrate the experimental implementation of the adiabatic geometric phase gates in electron spins, and how different parameters affect the performance of the phase gate. The comparison with some dynamic phase gates is also discussed.

The sample used in all the experiments is a ^{31}P doped ^{28}Si single crystal with P concentration of $\sim 10^{14}$ cm^{-3}, which has an electron spin relaxation time of approximately 10 ms and decoherence time of 450 μs at 8 K and 9.8 GHz.

5.3.1 Implementation of adiabatic geometric phase gate

The adiabatic control sequence applied in the experiment is described by Equations 5.7 – 5.11. The frequency and the amplitude of the microwave field is controlled via modulating a microwave source with an IQ mixer. Figure 5.9 shows a block diagram of the experimental setup for the microwave control. The two signal generators are phase locked and serve as the referenced microwave sources. The arbitrary waveform generator (AWG) creates the required I and Q components to feed in the IQ mixer integrated in the vector signal generator (VSG), such that the output of the VSG is modulated and have the required profile in the rotating frame. A solid-state amplifier is used in place of the conventional travelling wave tube amplifier because the solid-state amplifier provides a wider range of linear amplification of the microwave intensity, and the preservation of the amplitude modulation of the microwave field is the key in achieving accurate adiabatic control. Finally the detected signal is demodulated by the signal from the phase locked analog signal generator (PSG).

Figure 5.10 (a-c) shows an example of the frequency, amplitude and phase of the microwave field during the adiabatic control sequence for a π phase gate. In order to adjust the length of the adiabatic control sequence with more flexibility, two parameters t_d and t_s are introduced to replace the single parameter τ, where t_d denotes the time during which the microwave frequency is tuned between off-resonance and on-resonance, t_s denotes the time during which the microwave phase is swept from 0 to ϕ. Therefore the length of the

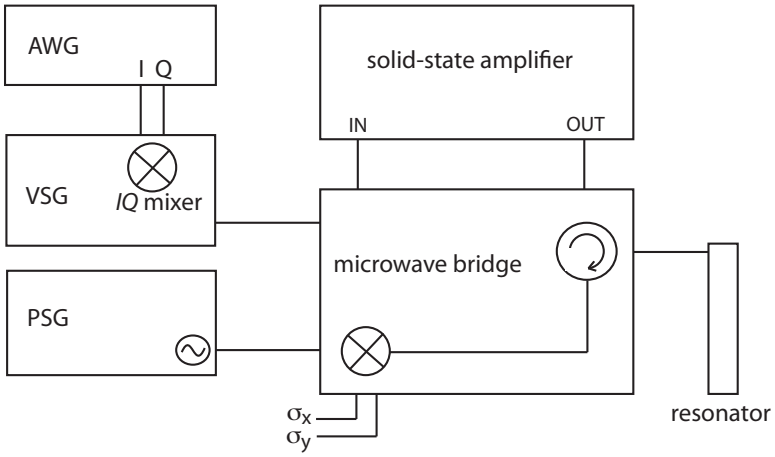

FIGURE 5.9: Block diagram of the experimental setup for the adiabatic geometric phase gate experiment.

whole adiabatic sequence is $2t_d + t_s$. Figure 5.10 (d) shows the I, Q components needed to modulate a sinusoidal microwave source in order to create this particular control sequence. It can be seen that the fast oscillations in the I, Q components at the beginning and the end of the sequence are due to the detuning Δ of the microwave, whereas during $t_d < t < t_d + t_s$ when the microwave is on-resonance, the variation in the I, Q components is purely due to the adiabatic phase change of the microwave. Besides, the π phase shift at $t_{\rm ad} = t_d + t_s/2$ is achieved by inverting the sign of the I, Q components instantaneously at the moment.

In order to detect the effect of the phase gate, it is necessary to rotate the electron spin into the xy plane, and measure the phase of the spin coherence before and after the phase gate. Therefore the full pulse sequence for measuring the geometric phase is composed of an initial $\pi/2$ pulse that creates the spin coherence in the xy plane, the adiabatic control sequence, and a π pulse that refocuses the random field inhomogeneities in the environment (Figure 5.11 (a)). The spin echo is detected and its phase is determined from the quadrature detection, from which the phase acquired during the adiabatic phase gate can be deduced.

According to the model, the geometric phase γ obtained after an adiabatic geometric phase gate equals to the phase ϕ swept by the microwave field in the xy plane (as defined in Figure 5.1), i.e. $\gamma = \phi$. Figure 5.11 (b) shows the experimentally measured γ against ϕ

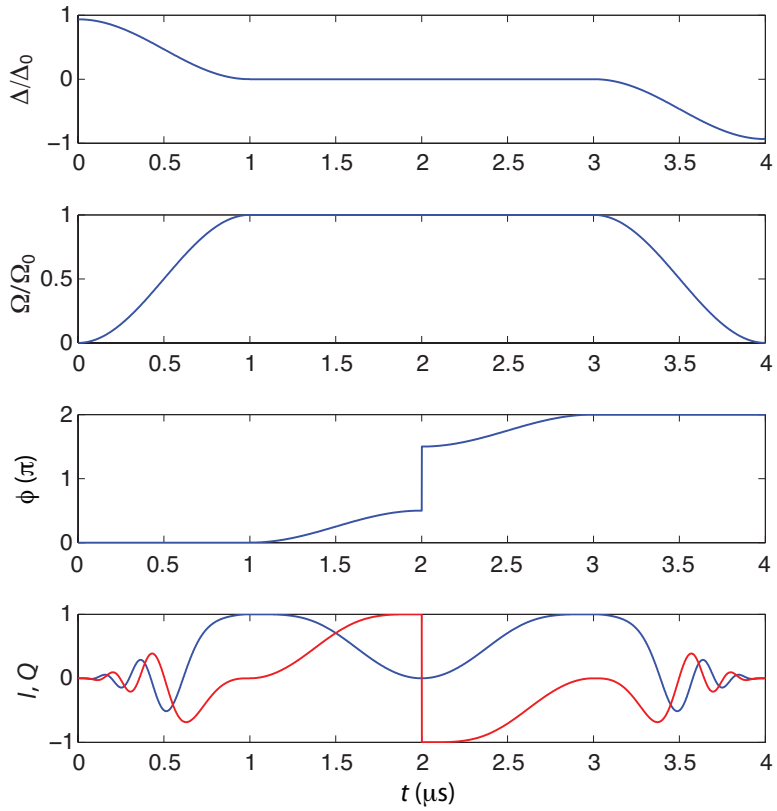

Figure 5.10: Detuning Δ, amplitude Ω, phase ϕ of the microwave field for an adiabatic geometric phase gate of π, and the corresponding I, Q components necessary to generate the required microwave field. $t_d = t_s/2 = 1$ μs, $\Delta_0 = 6$ MHz are used in this example.

(ϕ is predetermined and used for programming the AWG). The experimental data follows the relation very well over a broad range of ϕ — from 0 to 20π, which verifies that we have successfully applied the adiabatic geometric phase gate to the electron spins. Figure 5.11 (c) plots the error in phase $\epsilon_\gamma = \gamma - \phi$ for a narrower range of ϕ from 0 to 2π.

The intensity of the spin echo is also plotted against ϕ (Figure 5.11 (d)) as a measurement of the performance of the phase gate. The echo intensities are normalized to a Hahn echo detected at the same position. The fact that the echo intensities at $\phi = 0$ are less than 1 indicates that the adiabatic processes are not perfect, and implies a partial adiabatic following of the whole spin ensemble. This is partly due to the off-resonance error of the spins. However, since the EPR linewidth of the spins are narrower than the bandwidth of the adiabatic control sequence, the failure of adiabatic following is more generally due to

the non adiabaticity of the phase gate operation. This also explains why the echo intensity decreases for greater ϕ — for a fixed duration of the adiabatic control sequence, a greater ϕ means a faster phase variation in the xy plane during $t_d < t < t_d + t_s$, hence a less adiabatic operation. In addition, because of the off-resonance error and inhomogeneities in the microwave, the spins in different spin packets will not follow exactly the same path during the adiabatic operation, and by the end of the evolution they will exhibit a spread in the final phase. While the geometric phase γ is a measurement of the mean phase of all the spins, the spin echo intensity reflects the variance of phase of different spin packets, since the reduction of the echo intensity can be understood as due to the loss of phase coherence of the spins. Figure 5.11 (e) shows this spread (variance) in the phase σ as a function of ϕ, which is defined as inversely proportional to the echo intensity.

5.3.2 Exploring various parameters

There are several tunable parameters in the adiabatic control sequence: phase and frequency ramping durations t_s, t_d, amplitude of the microwave Ω_0, and initial detuning Δ_0. In the experiment, we varied all these parameters within reasonable ranges and looked for an optimized combination of them.

Ramping durations, t_s and t_d

The length of the π pulses applied in our experiment is around $t_\pi = 800$ ns or longer. This is longer than the π pulses in common EPR spectrometers because the amplitude of the microwave obtainable in our experiment is limited by the output power of the microwave source and the range of linear amplification of the solid-state amplifier. According to Equation 5.14, the length of a composite BB1 π pulse is not less than $t_{\pi,\mathrm{BB1}} = 5t_\pi = 4$ μs, a dynamic phase gate using BB1 pulses (Equation 5.15) and a geometric phase gate using BB1 pulses (Equation 5.17) will be no less than $t_{\mathrm{dyn,BB1}} = 11$ μs and $t_{\mathrm{geo,BB1}} = 8$ μs, respectively.

The adiabatic operation is in general slow in order to meet the requirement of adiabatic conditions. However, to be a practical gate operation in quantum information processing, it

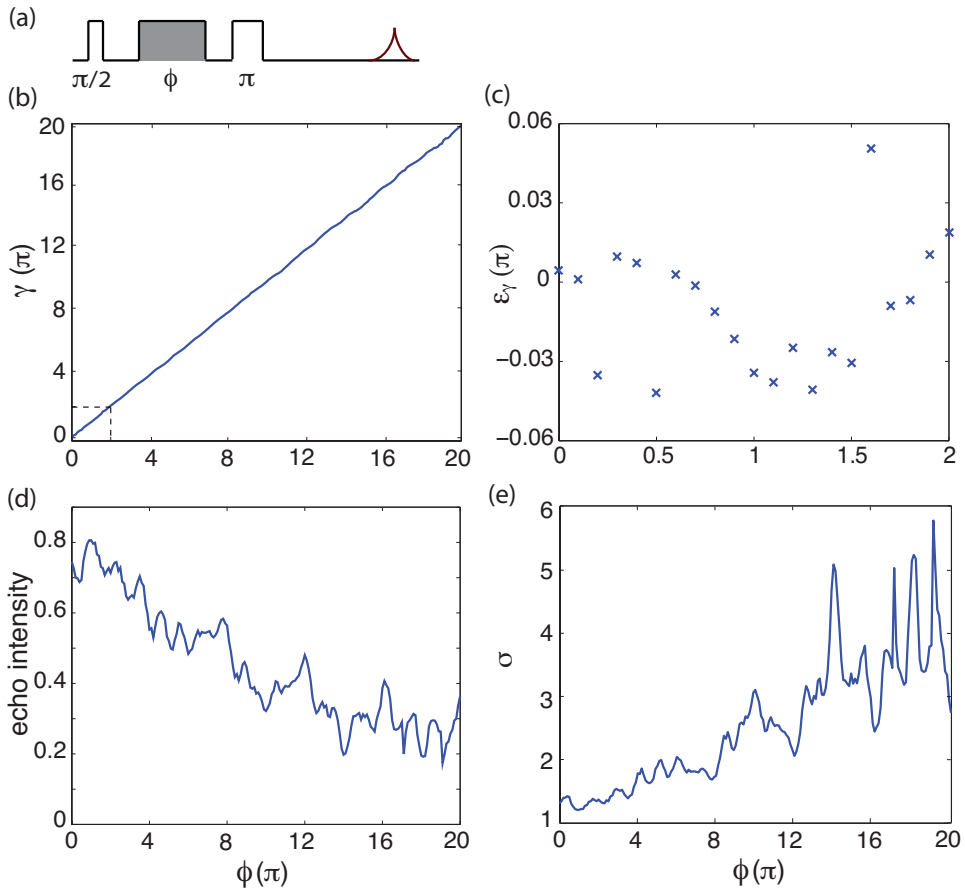

Figure 5.11: (a) Pulse sequence for measuring the adiabatic geometric phase gate. (b) Measured phase change of the spin γ as a function of ϕ. The dotted lines mark the region plotted in (c). (c) Error in the obtained phase $\epsilon_\gamma = \gamma - \phi$ for the range of $\phi = 0$ to 2π. (d) Spin echo intensity after the adiabatic geometric phase gate, normalized to the Hahn echo detected at the same position. (e) Variance in phase of the final states of the spin packet when we assume the distribution in γ is Gaussian.

is necessary that the adiabatic process is much shorter than the electron spin decoherence time, i.e. $t_{\mathrm{ad}} \ll T_{2\mathrm{e}}$. On the other hand, in order to compare the performance of different phase gates, it is preferable that the adiabatic control sequence has a similar length to the phase gates using dynamic pulses. Therefore, in our experiment t_{ad} is varied between 6 μs and 12 μs by varying t_s and t_d separately. The bandwidth of the adiabatic phase gate is no less than 80 kHz which is broader than the spin linewidth, and this ensures that the off-resonance errors in the spin ensemble can be neglected.

Figure 5.12 shows the results of the geometric phase γ acquired by the spin and the

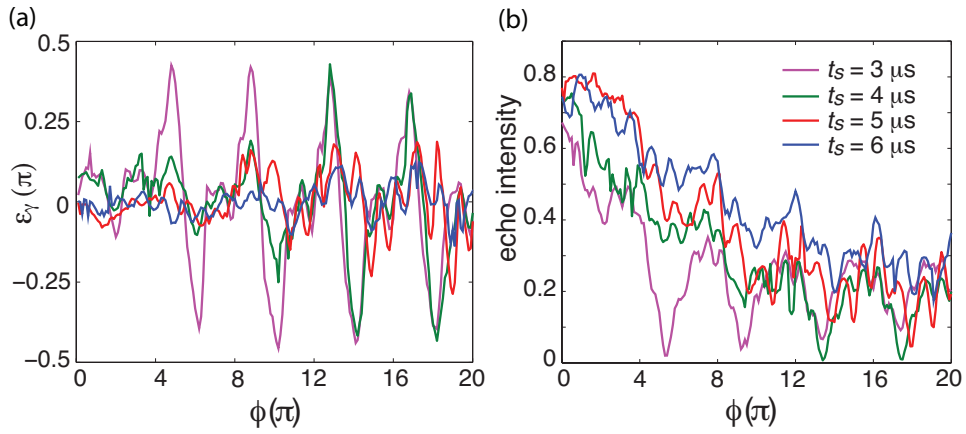

FIGURE 5.12: (a) Error in the obtained phase $\epsilon_\gamma = \gamma - \phi$, (b) echo intensity after adiabatic geometric phase gates of different t_s. (a) and (b) share the same legends.

intensity of spin echo as a function of ϕ where $t_d = 2$ μs is kept constant and t_s is varied from 3 μs to 6 μs. The geometric phase (Figure 5.12 (a)) follows well the speculated relation $\gamma = \phi$ for $t_s \geq 5$ μs, and the decrease in the spin echo intensity as a function of ϕ (Figure 5.12 (b)) is faster for shorter t_s. This is expected because a shorter t_s means a faster phase sweep in the xy plane (larger $\dot{\phi}$), which is detrimental to the adiabatic evolution of the spins following the microwave field. The dips in the echo intensity traces for $t_s = 3$ μs and $t_s = 4$ μs are due to the non-adiabaticity of the control sequence, and similar features have been observed in the simulations. Furthermore, it is natural that the dips in the traces of echo intensity are at the same positions as the ripples in the traces of geometric phase, because the calculation of the phase is less accurate when the signal to noise ratio is low.

Figure 5.13 shows the geometric phase γ and the spin echo intensity as a function of ϕ where $t_s = 6$ μs is kept constant and t_d is varied from 1 μs to 4 μs. Similar to Figure 5.12, the echo intensities tend to be higher for larger t_d. The traces for $t_d = 2$ μs, 3 μs, 4 μs are relatively close to each other, whereas the trace for $t_d = 1$ μs is more distinct from the other three, being much lower especially for large ϕ. This also agrees with the prediction from the adiabatic conditions, that a slower evolution of the Hamiltonian, which in this case refers to a smaller $\dot{\Delta}(t)$, will result in a better performance of the adiabatic process.

According to the above results, $t_s = 6$ μs and $t_d = 2$ μs is a reasonable combination for

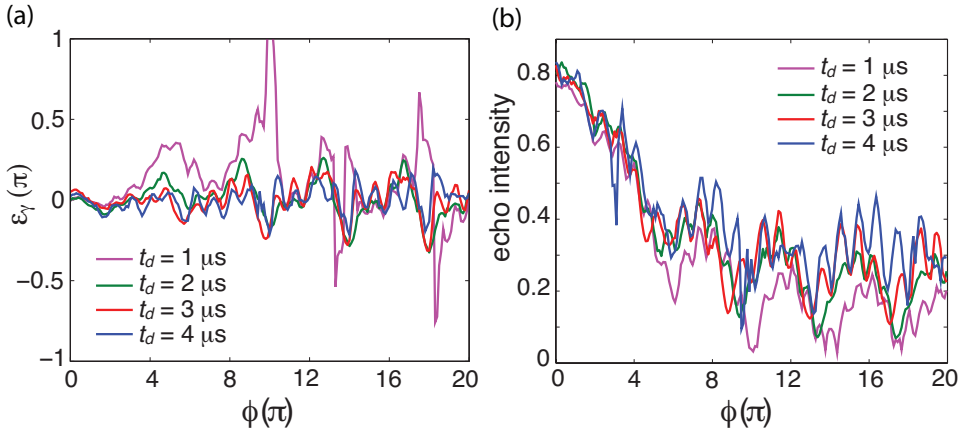

FIGURE 5.13: (a) Error in the obtained phase $\epsilon_\gamma = \gamma - \phi$, (b) echo intensity after adiabatic geometric phase gates of different t_d.

the timing of the adiabatic control sequence, and it gives a total length of $t_{\text{ad}} = 10\ \mu$s. These values are used for all the following experiments.

Amplitude of the control field, Ω_0

Ideally, the adiabatic control field Ω_0 should be strong enough to ensure the adiabatic following of the spins. In our experiment, however, the amplitude of the microwave Ω_0 is limited by our experimental setup, and the largest Ω_0 attainable is approximately 0.25 G, which corresponds to a Rabi frequency of approximately 0.83 MHz.

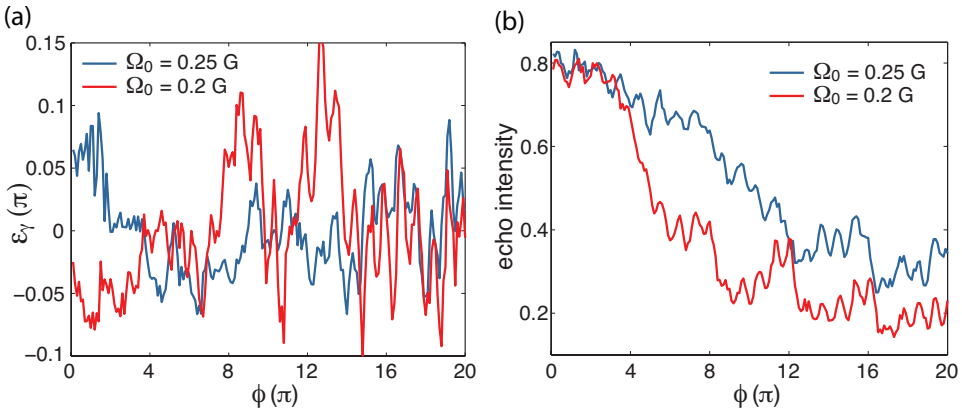

FIGURE 5.14: (a) Error in the obtained phase $\epsilon_\gamma = \gamma - \phi$, (b) echo intensity after adiabatic geometric phase gates of different Ω_0.

Figure 5.14 shows the geometric phase γ and the spin echo intensity as a function of ϕ for two different $\Omega_0 = 0.25$ G and 0.2 G, while the amplitude for the dynamic pulses (initial $\pi/2$ pulse and the refocusing pulse) are kept constant. As shown more obviously in the traces of the echo intensities, the performance of the adiabatic geometric phase gate worsens quickly as Ω_0 decreases. This is expected because in this parameter range where Ω_0/t_{ad} is still small enough to not violate the adiabatic condition, a larger Ω_0 will always mean a better adiabatic evolution of the spins. From this point of view, although the results discussed in this thesis are limited by our current experimental setup, a higher microwave power will be favorable in the performance of the adiabatic geometric phase gate and is worth investigating.

Microwave detuning, Δ_0

The adiabatic condition for the detuning of the microwave field Δ_0 requires it to be much stronger than the detuning of the spins in the static field, so that all the spins can be initially aligned along the z-axis by the effective field. This means that Δ_0 should be much larger than the spin linewidth. In addition, as discussed earlier, Δ_0 should not be too large because $\dot{\Delta}(t)$ needs to be small to conform with the adiabatic conditions. In the experiment Δ_0 is varied from 1 MHz to 10 MHz.

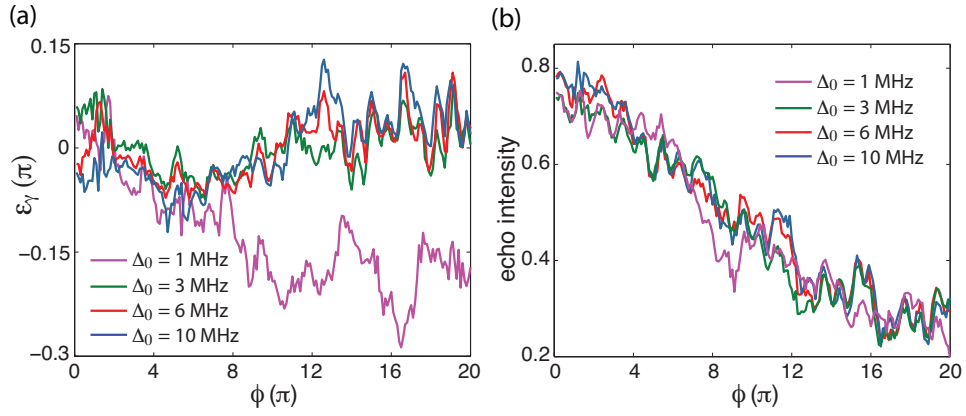

FIGURE 5.15: (a) Error in the obtained phase $\epsilon_\gamma = \gamma - \phi$, (b) echo intensity after adiabatic geometric phase gates of different Δ_0.

Figure 5.15 shows the geometric phase γ and the spin echo intensity as a function of ϕ

for different Δ_0. It can be seen that all the results are very close to each other except for $\Delta_0 = 1$ MHz in both phase and echo intensity. Therefore, for simplicity Δ_0 is kept to 6 MHz in all the following experiments.

5.3.3 Comparison with dynamic phase gates

To compare the adiabatic geometric phase gate with dynamic phase gates, we apply the phase gates of the same phase using both adiabatic control and dynamic pulse sequences defined in Equation 5.13 and 5.15. As discussed in the previous section, the parameters of the adiabatic control sequence are chosen as the following: $t_d = 2$ μs, $t_s = 6$ μs, $\Delta_0 = 6$ MHz, $\Omega_0 = 0.25$ G. The length of a dynamic π pulse is 700 ns.

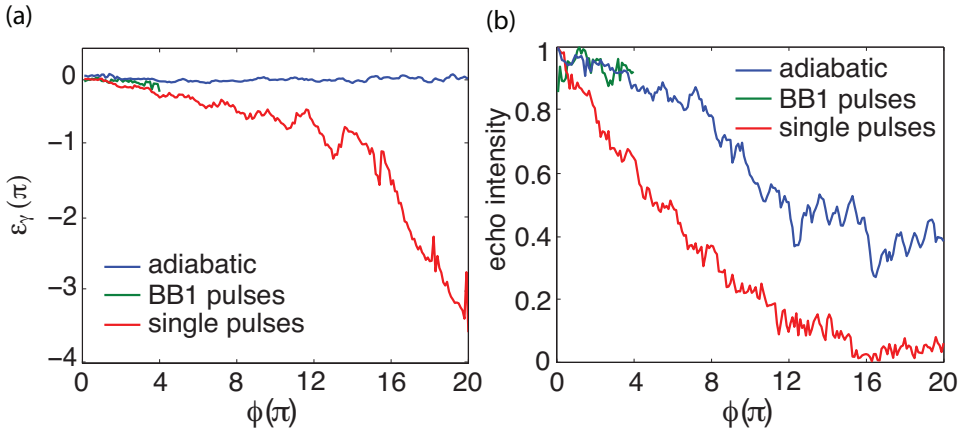

Figure 5.16: (a) Error in the obtained phase $\epsilon_\gamma = \gamma - \phi$, (b) echo intensity after an adiabatic geometric phase gate, a dynamic phase gate using single microwave pulses and a dynamic phase gate using BB1 composite pulses.

Figure 5.16 shows the measured phase as well as intensity of the spin echo signal. The spin echoes are detected at the same position after the initial $\pi/2$ pulse so that the spin decoherence will have the same effect in each situation. The measurement for BB1 composite pulse sequence is only valid up to $\phi = 4\pi$ because according to Equation 5.14 the BB1 pulses can only be defined for $|\phi| \leq 4\pi$. It can be seen that the adiabatic geometric phase gate works better than both the dynamic phase gate using single dynamic pulses and the one using BB1 composite pulses, and the difference is more marked when ϕ gets larger. Figure 5.16

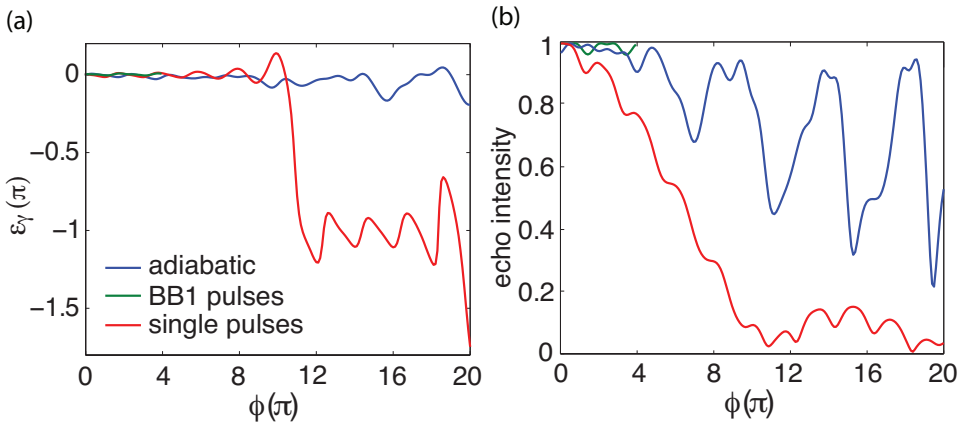

FIGURE 5.17: **Simulation**. (a) Error in the obtained phase $\epsilon_\gamma = \gamma - \phi$, (b) echo intensity after an adiabatic geometric phase gate, a dynamic phase gate using single microwave pulses and a dynamic phase gate using BB1 composite pulses. The parameters used in the simulation are: $t_s = 2t_d = 6$ μs, $\Omega_0 = 0.5$ G, $\Delta_0 = 6$ MHz.

(a) implies that the geometric phase obtained from the adiabatic phase gate closely follows the relation $\gamma = \phi$ whereas the phase obtained from the two dynamic phase gates deviates severely from this relation. Meanwhile, in Figure 5.16 (b) the echo intensity obtained after the adiabatic phase gate reduces more slowly than the other two phase gates. For the dynamic phase gate using single microwave pulses the spin echo intensities reduce to about 20% of their values at $\phi = 0$ when $\phi > 8\pi$. This reduction in echo intensity results in inaccuracies in the calculation of the phase of the final spin state, hence explains why there are large errors in the phase for $\phi > 8\pi$ for the corresponding dynamic phase gate.

The experimental data can be compared with the simulations shown in Figure 5.17. Similar to the experiment, the phase gate using BB1 pulses can only have definition for $|\phi| \leq 4\pi$. In the simulation we assume 10% inhomogeneity in microwave field and no off-resonance effect of the spin packets is considered. The simulation reproduces the main features in the echo intensities for the dynamic phase gate using single microwave pulses, which implies that the decreases in these echo intensities are mostly due to the B_1 inhomogeneity. The echo intensity for the adiabatic geometric phase gate measured in the experiment never recovers to close to 1 after $\phi = 8\pi$ as it does in the simulation. This means that the global decrease must result from other imperfections of the system than B_1 inhomogeneity, such as inhomogeneity

of the static field and the off-resonance effect of the spin packets.

5.3.4 Comparison with geometric phase gates with dynamic pulses

In this section, the adiabatic geometric phase gate is compared with the geometric phase gates using dynamic microwave pulses: single microwave pulses (Equation 5.16) and BB1 composite pulses (Equation 5.17). Since for the geometric phase gates using dynamic pulses the pulse sequences are determined only by the phase difference between the two π pulses, or more simply, with the phase of the first π pulse fixed, only by the phase of the second π pulse ψ_2, therefore the pulse sequence will repeat at every $\Delta\psi_2 = 2\pi$. This causes the resultant geometric phase to repeat at every $\Delta\gamma = 2\Delta\psi_2 = 4\pi$. Therefore, the comparison is carried out only in the range of $\gamma = 0 \sim 4\pi$.

The same values of the parameters are used for the adiabatic sequence here as in the previous experiment.

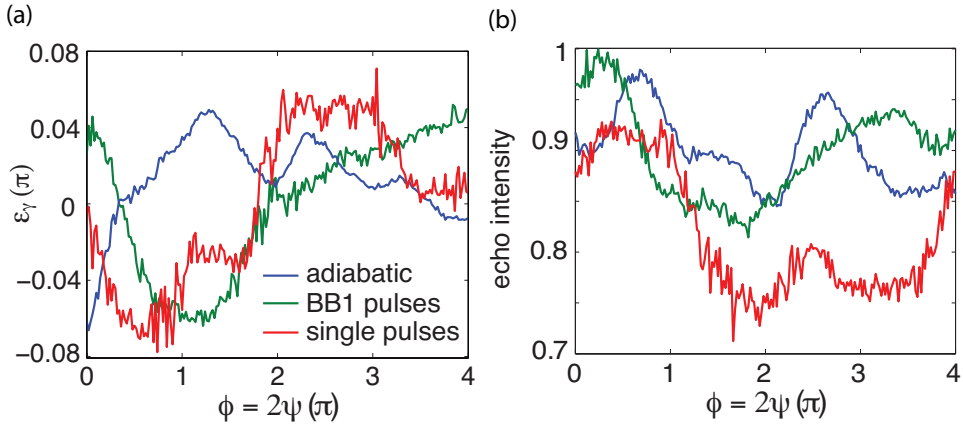

Figure 5.18: (a) Error in the obtained phase $\epsilon_\gamma = \gamma - \phi$, (b) echo intensity after an adiabatic geometric phase gate, a geometric phase gate using single microwave pulses and a geometric phase gate using BB1 composite pulses.

Figure 5.18 shows the measured geometric phase γ and the echo intensity for the three geometric phase gates. It can be seen that in both phase error and echo intensity, the adiabatic geometric phase gate has a similar performance to the geometric phase gate using BB1 composite pulses, although from the point of view of correcting the off-resonance effect

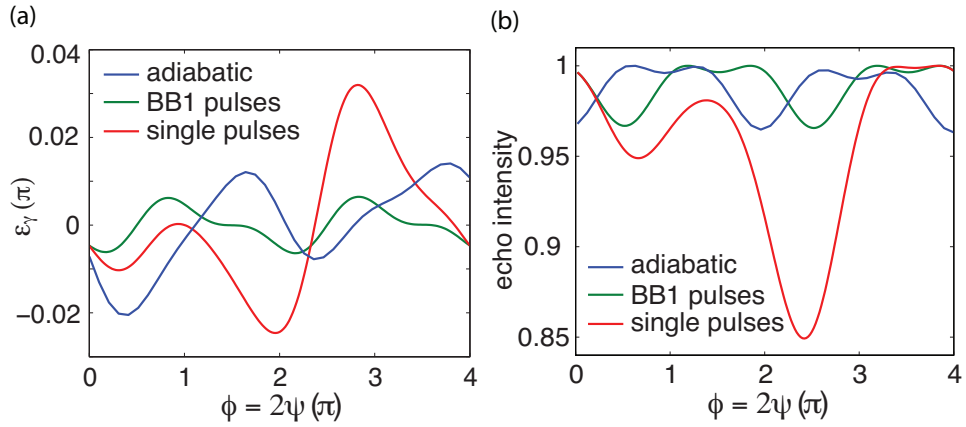

FIGURE 5.19: **Simulation**. (a) Error in the obtained phase $\epsilon_\gamma = \gamma - \phi$, (b) echo intensity after an adiabatic geometric phase gate, a geometric phase gate using single microwave pulses and a geometric phase gate using BB1 composite pulses. The parameters used in the simulation are: $t_s = 2t_d = 6$ μs, $\Omega_0 = 0.5$ G, $\Delta_0 = 6$ MHz

of the spin packets the adiabatic geometric phase gate indeed outperforms the geometric phase gate using single dynamic pulses.

The simulation shown in Figure 5.19 verifies the measurements from the experiment that the adiabatic and BB1 geometric phase gates have similar fidelities and are both better than the geometric phase gate using single dynamic pulses.

A previous theoretical study on the decoherence effect during an adiabatic geometric phase gate has shown similar conclusion, that the slow adiabatic process suffers more from the decoherence and thus does not exceed the dynamic gate operations [Naz02]. Although the gate time for the dynamic pulse sequences are close to the adiabatic gate time in our experiments, which are around 10 μs for both BB1 and adiabatic geometric phase gates, the fidelity of the adiabatic geometric phase gate is still limited by other imperfections of the equipments such as the amplitude of the microwave field.

5.4 Conclusions

Adiabatic manipulation is an alternative to the dynamic microwave pulses commonly used in pulsed EPR to control the state of the electron spins. A single qubit geometric phase gate

via adiabatic control is realized by creating an adiabatically varying effective magnetic field that evolves cyclically, and the phase acquired by the spin is only decided by the geometry of the evolution of the effective field. Simulations verify that the adiabatic geometric phase gate is robust against fast fluctuations in the external static field and inhomogeneities in the microwave field, which is an advantage of the adiabatic operation. On the other hand, the adiabatic condition requires that the phase gate is carried out slowly and the driving field is strong, whereas these two parameters are limited by the decoherence time of the electron spins and the microwave field attainable in an EPR spectrometer. The experiment shows that using current experimental setup the adiabatic geometric phase gate has comparable performance to the geometric phase gate using composite dynamic pulses such as BB1 pulse, though allowing a higher microwave power the adiabatic phase gate could perform better.

6

Simulation of pulsed EPR experiments

For a system of known spin Hamiltonian, it is in principle always possible to calculate its characteristic frequencies and track its dynamic evolution in an EPR experiment. However, with a spin system of unknown structure and parameters, it is not always easy to extract the desired information from the EPR spectra. One reason is that the parameters of the system under investigation cannot be uniquely determined from the experimental spectrum. Moreover, the imperfections of the experiment may suppress some features of the spin system in the experimental spectrum which otherwise should appear in an ideal spectrum. Therefore, it is important to utilize the simulated spectra with trial parameters to predict or fit the experimental spectra, and to extract accurate information of the spin system.

In this chapter, I present a method for simulating the time evolution of spin systems in pulsed EPR experiments, and give some example of applications of the simulation program.

6.1 Motivation for a new simulation toolbox

Currently there are only a few software packages for simulating EPR spectra. EasySpin [Sto03, Sto06] is a widely used toolbox running on Matlab that provides all necessary tools for basic data processing and spectra simulation including solid-state (both single crystals and powder) and solution, fast and slow-motion CW EPR. The simulation of pulsed EPR spectra, on the other hand, is more complicated as it involves following the evolution of the observables during the pulse sequence. It has been recently made possible for certain pulsed EPR experiments including ESEEM, HYSCORE and ENDOR in the software Molecular Sophe [Han09] and a newly developed feature of EasySpin [Sto09].

In the algorithms of the simulation software mentioned above, each microwave pulse, radio frequency pulse or free evolution period is treated as a single operation and is represented by a propagator. Therefore, the entire pulsed experiment is described by an array of propagators representing the whole pulse sequence and the free precessions intermediate between each two pulses. The density matrix and eigenstates of the spin system at the detection point are calculated, and the spectrum is constructed either by doing the calculation

for each component over the entire 1D or 2D time domain [Mad02], or by calculating a histogram in the frequency domain and performing an inverse Fourier transformation [Szo98]. The advantage of these algorithms, especially the frequency domain approach, is that the calculations can be carried out quickly. However, their disadvantage is as obvious — only the state of the spin system at the detection point is given, which is not convenient for simulating the evolution of the spin system during the pulse sequence.

The difference of the simulation program I present here to the ones mentioned above is that it allows the observation of the state of the spin system at any moment during the experiment by calculating the density matrix of the spin system by very short time steps. It also allows a more general definition of the microwave or radio frequency pulses, which provides more flexibility in defining the pulse sequences.

6.2 Realization

6.2.1 Pauli matrices for coupled spins

The Pauli matrices for a system of coupled spins are built based on the tensor product of the Pauli matrices of the comprising spins.

Firstly, for an isolated spin S the generalized Pauli matrices have dimension $(2S+1) \times (2S+1)$. The definitions of σ_z, raising and lowering operators $\sigma_\pm$ are given as: for any $1 \leq j \leq 2S+1$,

$$\sigma_{z,(j,j)} = S - j, \quad \sigma_{z,(j,k)} = 0 \text{ for all } j \neq k; \tag{6.1}$$

$$\sigma_{+,(j,j+1)} = \sqrt{j(2S-j+1)}, \quad \sigma_{+,(j,k)} = 0 \text{ for all } j \neq k-1; \tag{6.2}$$

$$\sigma_{-,(j,j-1)} = \sqrt{j(2S-j+1)}, \quad \sigma_{+,(j,k)} = 0 \text{ for all } j \neq k+1. \tag{6.3}$$

σ_x and σ_y are obtained using the relation

$$\sigma_x = \frac{\sigma_+ + \sigma_-}{2}, \quad \sigma_y = \frac{\sigma_+ - \sigma_-}{2i}. \tag{6.4}$$

When n spins form a coupled system, the dimension of the Hilbert space of the coupled system is $\prod(2S_k+1)$. Denoting the Pauli matrices of each comprising spin S_k as an isolated spin by $\sigma_{\alpha,k}(\alpha = x, y, z)$, then the new Pauli matrices of each coupled spin is generated by

$$\sigma_\alpha^{(k)} = \bigotimes_{j<k} I_j \otimes \sigma_{\alpha,k} \otimes \bigotimes_{m>k} I_m. \tag{6.5}$$

Here I_j is the identity matrix of dimension $(2S_j+1)\times(2S_j+1)$.

If we take an example of a couple electron spin $S = 1/2$ and a nuclear spin $I = 1/2$, from Equation 6.5 we obtain the Pauli matrices for the coupled spins

$$\sigma_x^{(S)} = \frac{1}{2}\begin{pmatrix} 0 & 0 & 1 & 0 \\ 0 & 0 & 0 & 1 \\ 1 & 0 & 0 & 0 \\ 0 & 1 & 0 & 0 \end{pmatrix},\ \sigma_y^{(S)} = \frac{1}{2}\begin{pmatrix} 0 & 0 & -i & 0 \\ 0 & 0 & 0 & -i \\ i & 0 & 0 & 0 \\ 0 & i & 0 & 0 \end{pmatrix},\ \sigma_z^{(S)} = \frac{1}{2}\begin{pmatrix} 1 & 0 & 0 & 0 \\ 0 & 1 & 0 & 0 \\ 0 & 0 & -1 & 0 \\ 0 & 0 & 0 & -1 \end{pmatrix},$$
$$\sigma_x^{(I)} = \frac{1}{2}\begin{pmatrix} 0 & 1 & 0 & 0 \\ 1 & 0 & 0 & 0 \\ 0 & 0 & 0 & 1 \\ 0 & 0 & 1 & 0 \end{pmatrix},\ \sigma_y^{(I)} = \frac{1}{2}\begin{pmatrix} 0 & -i & 0 & 0 \\ i & 0 & 0 & 0 \\ 0 & 0 & 0 & -i \\ 0 & 0 & i & 0 \end{pmatrix},\ \sigma_z^{(I)} = \frac{1}{2}\begin{pmatrix} 1 & 0 & 0 & 0 \\ 0 & -1 & 0 & 0 \\ 0 & 0 & 1 & 0 \\ 0 & 0 & 0 & -1 \end{pmatrix}. \tag{6.6}$$

6.2.2 Hamiltonians and pulses

The spin Hamiltonian used for the simulation is defined by Equation 2.11. When only one electron spin $\boldsymbol{S}$ and one coupled nuclear spin $\boldsymbol{I}$ are concerned, Equation 2.11 reduces to

$$\begin{aligned} H_0 &= H_{EZ} + H_{NZ} + H_{ZF} + H_{NQ} + H_{HF} \\ &= \mu_B \boldsymbol{B}_0^{\mathrm{T}} \boldsymbol{g} \boldsymbol{S} - \mu_{\mathrm{n}} \boldsymbol{B}_0^{\mathrm{T}} \boldsymbol{g}_{\mathrm{n}} \boldsymbol{I} + h \boldsymbol{S}^{\mathrm{T}} \boldsymbol{D} \boldsymbol{S} + h \boldsymbol{I}^{\mathrm{T}} \boldsymbol{Q} \boldsymbol{I} + h \boldsymbol{S}^{\mathrm{T}} \boldsymbol{A} \boldsymbol{I}. \end{aligned} \tag{6.7}$$

Here $\boldsymbol{S} = \sigma_x^{(S)}\hat{x} + \sigma_y^{(S)}\hat{y} + \sigma_z^{(S)}\hat{z}, \boldsymbol{I} = \sigma_x^{(I)}\hat{x} + \sigma_y^{(I)}\hat{y} + \sigma_z^{(I)}\hat{z}$ are the spin vectors, with $\sigma_\alpha^{(k)}(\alpha = x, y, z; k = S, I)$ the Pauli matrices for the electron and nuclear spin of the coupled system as defined by Equation 6.5.

The microwave or radio frequency pulses are described by the Hamiltonian as defined in Equation 2.12. Specifically, when the frequency and phase of the microwave (radio frequency)

pulse are ω_{mw} (ω_{rf}) and ϕ_{mw} (ϕ_{rf}), the time-dependent Hamiltonians are

$$H_{1,\mathrm{mw}}(t) = 2\mu_B g_e B_{\mathrm{mw}} \cos(\omega_{\mathrm{mw}} t + \phi_1)\sigma_x^{(S)}, \quad H_{1,\mathrm{rf}}(t) = -2\mu_{\mathrm{n}} g_{\mathrm{n}} B_{\mathrm{rf}} \cos(\omega_{\mathrm{rf}} t + \phi_2)\sigma_x^{(I)}. \quad (6.8)$$

The total Hamiltonian $H(t) = H_0 + H_{1,\mathrm{mw}}(t) + H_{1,\mathrm{rf}}(t)$ is a complete description of the dynamics of the spin system in an ideal pulsed EPR experiment, where the pulses have a constant amplitude and frequency. In order to be able to describe more complicated pulse sequences such as shaped pulses or time-dependent detunings, the amplitude and frequency of the pulses in Equation 6.8 need to be defined as functions of time, $B_{\mathrm{mw/rf}}(t)$ and $\omega_{\mathrm{mw/rf}}(t)$. Although the variation in the frequency of an electromagnetic field can be created via the modulation of its amplitude, it is easier and more direct to define the frequency as a function of time than to convert it into amplitude modulation.

6.2.3 Time evolution

In most cases, the microwave pulses applied in EPR experiments are on resonance or near resonance with the transition frequencies (ω_0) of the electron spin, so we can transform $H(t)$ into a rotating frame and remove the fast oscillating component of the Hamiltonian. The principle of the transformation is the same as described in Section 2.5. The difference is that now $\omega_{\mathrm{mw}}(t)$ is time-dependent, so it is necessary to define another frequency of the rotating frame ω_R which is constant. Now the transformation operator as defined in Equation 2.21 becomes

$$U(t) = e^{i\frac{\omega_R t}{2}\sigma_z^{(S)}}, \quad (6.9)$$

and the Hamiltonian in the rotating frame is

$$H_R = H_{0,R} + \gamma B_{\mathrm{mw}}(t) \cos(\Delta(t)t + \phi_{\mathrm{mw}})\sigma_x^{(S)}, \quad (6.10)$$

where $\Delta(t) = \omega_{\mathrm{mw}}(t) - \omega_R$ is a function of time; $H_{0,R} = U^{-1}H_0U - \frac{\hbar}{2}\omega_R\sigma_z^{(S)}$ is the time-independent Hamiltonian in the rotating frame which can be complicated if H_0 contains $\sigma_{x,y}^{(S)}$. When H_0 contains only the terms with $\sigma_z^{(S)}$ (the nuclear Zeeman and nuclear quadrupole terms do not affect the transformation as the operators in the nuclear degrees of freedom

commute with $\sigma_z^{(S)}$), we can write H_0 as $H_0 = -\hbar\omega_0\sigma_z^{(S)}/2$. By defining $\Delta_0 = \omega_0 - \omega_R$ as the detuning of the rotating frame from resonance, Equation 6.10 becomes similar to Equation 2.25

$$H_R = -\frac{\hbar}{2}\Delta_0\sigma_z^{(S)} + \gamma B_{\mathrm{mw}}(t)\cos(\Delta(t)t + \phi_{\mathrm{mw}})\sigma_x^{(S)}. \tag{6.11}$$

One assumption made about the simulation is that the duration of the experiments are short compared to the relaxation time of the spins, so that the evolution of the system is always unitary. In this case the evolution of the density matrix of the spin system should obey the von Neumann equation (Equation 2.14).

As H_R is explicitly time-dependent, the calculation of the evolution propagator (using Equation 2.15) will become difficult. The solution is to carry out integrations for each small time step δt and assuming during each δt the time-dependent part of H_R is constant, with δt being usually a few nanoseconds for the calculations in the rotating frame. The elementary propagator for a time step δt at the moment t is

$$\delta U_R(t) = e^{-i\frac{H_R(t)}{\hbar}\delta t}. \tag{6.12}$$

The evolution of the density matrix in the rotating frame will then be calculated step by step as

$$\rho_R(t+\delta t) = \delta U_R(t)\rho_R(t)\delta U_R^{\dagger}(t) = e^{-i\frac{H_R(t)}{\hbar}\delta t}\rho_R(t)e^{i\frac{H_R(t)}{\hbar}\delta t}. \tag{6.13}$$

In typical EPR experiments, the rotating wave approximation is always valid. But in some other cases, the driving field is very strong and the rotating wave approximation breaks down [Oli05, Fuc09]. When this happens it is possible to extend the validity of our model by staying in the lab frame and using the lab frame Hamiltonian $H(t)$ instead of $H_R(t)$ in Equation 6.12 and 6.13. The elementary time evolution propagator and density matrix in the lab frame can be calculated similarly

$$\delta U(t) = e^{-i\frac{H(t)}{\hbar}\delta t}, \tag{6.14}$$

$$\rho(t+\delta t) = e^{-i\frac{H(t)}{\hbar}\delta t}\rho(t)e^{i\frac{H(t)}{\hbar}\delta t}. \tag{6.15}$$

However, in this case, δt must be chosen much shorter than the one used in the rotating frame, usually in the order of picosecond, because now the time-dependent part of the lab

frame Hamiltonian $H(t)$ oscillates much faster than in $H_R(t)$. Understandably, the reduction in δt will increase the complexity of the computation and thus reduce the efficiency of the simulation.

6.2.4 Spin packets and inhomogeneities

In EPR experiments, spins in different spin packet often experience different environmental fields due to the inhomogeneities in B_0 and in the distribution of environmental spins. In the simulation, this effect is modelled by attributing a set of parameters to each spin packet describing the characteristic interactions of the spin with its environment such as B_0 inhomogeneity (ΔB_0), hyperfine tensor ($\boldsymbol{A}$), zero-field tensor ($\boldsymbol{D}$) etc. Each one of the parameters is varied in turn, thus simulating each individual spin packet. The time evolution of the whole ensemble is the sum of the time evolution of all the spin packets

$$\rho_{\text{ensemble}}(t) = \sum_{\mathcal{P}} p(\mathcal{P})\rho_{\text{packet}}(t;\mathcal{P}), \tag{6.16}$$

where $\mathcal{P}$ denotes a set of values for the parameters $\Delta B_0, \boldsymbol{A}, \boldsymbol{D}, \ldots$. $\rho(t;\mathcal{P})$ and $p(\mathcal{P})$ are the time evolution and population of the spins described by this set of parameters $\mathcal{P}$.

One direct example is the effect of B_0 inhomogeneity. With only one spin packet in the ensemble, the spin magnetization will always keep the same magnitude because the evolution considered in our model is unitary, whereas with many spin packets and a reasonable distribution of B_0 inhomogeneity over the ensemble, the sum of the horizontal magnetization will decay due to the dephasing of the spins. This decay of the horizontal magnetization is the simulated FID.

6.2.5 Measurement of transients

The quantum state of a spin system is observed by measuring $\langle \sigma_\alpha^{(k)} \rangle$. In EPR spectroscopy, the magnetization of the electron spin in the horizontal plane is detected with quadrature detection; when the phase of the signal is tuned correctly, the real and imaginary parts of

the signal represent the measurement of the spin magnetization along the x- and y-axis in the rotating frame, i.e. $S_{x,y}(t) = \langle \sigma_{x,y}^{(S)} \rangle$.

In the simulation, the transients $S_{x,y}(t)$ (also $S_z(t)$) are calculated using Equation 2.9,

$$S_\alpha(t) = \langle \sigma_\alpha^{(S)} \rangle = \mathrm{Tr}[\rho_R(t)\sigma_\alpha^{(S)}]. \tag{6.17}$$

Here $\rho_R(t)$ is the density matrix in the rotating frame. If the density matrix is calculated in the lab frame, then it is necessary to transform it into the rotating frame before the measurement using the transformation operator U defined in Equation 6.9

$$\rho_R(t) = U(t)\rho(t)U^\dagger(t). \tag{6.18}$$

6.3 Examples of application

6.3.1 Storage of two microwave pulses

The experiment of storing two microwave pulses of different phases and retrieving them in a reversed order using pulsed magnetic field gradients (Figure 3.9 (b")) is simulated, as shown in Figure 6.1. By comparing the two figures, it can be seen that the simulation predicts well the experimental transients and verifies the principle of multimode storage.

Here we assume a Gaussian distribution of the B_0 inhomogeneity over the ensemble of spins. Each spin is associated with a parameter that marks its z coordinate, and the field gradient pulse G is simulated by adding the term $\mu_B g_e G z$ to the spin Hamiltonian when the gradient pulse is applied. The number of distinct spin packets in the ensemble is set to 150: not comparable to the actual number of spins in the sample, but enough to show the effect of field inhomogeneities. This also explains the difference in the shape of echoes (T_2^*) between the simulation and the experimental data.

6.3.2 Adiabatic geometric phase gate

In Chapter 5 we saw some results from the simulation of the adiabatic geometric phase gate. Figure 5.4 showed an example of the evolution of the spin magnetization during a π phase

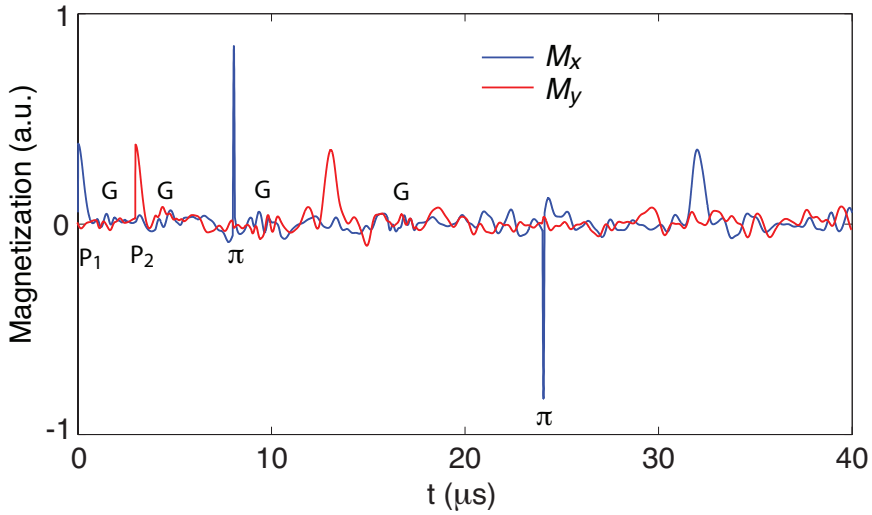

Figure 6.1: Simulated storage and retrieval of two microwave pulses using a pulsed field gradient. The parameters used in the simulation are: length of the two microwave pulses P_1, P_2 $t_P = 14$ ns, length of the π pulses $t_\pi = 112$ ns, length of the gradient pulses $t_G = 1.5$ μs; variance of the static field $\sigma(B_0) = 300$ mG, amplitude of the gradient pulses $G = 0.5$ G/mm.

gate measured in a special rotating frame — a rotating frame that has the same frequency as the driving microwave field at any time, hence the same reference frame as the Bloch sphere.

In EPR experiments, the detection is carried out in the rotating frame of a constant frequency ω_R, which is the frequency of the reference microwave. Figure 6.2 shows the simulated evolution of spin magnetization during the same adiabatic phase gate measured in this rotating frame of frequency ω_R. The initial state is $|0\rangle$. We can see the similarity between the simulated M_x, M_y and the I, Q signals in Figure 5.10, which illustrates the adiabatic following of the spin magnetization to the driving field. The π phase shift in the I, Q signals does not affect the direction of the spin magnetization, therefore it does not appear in the simulated transient signals.

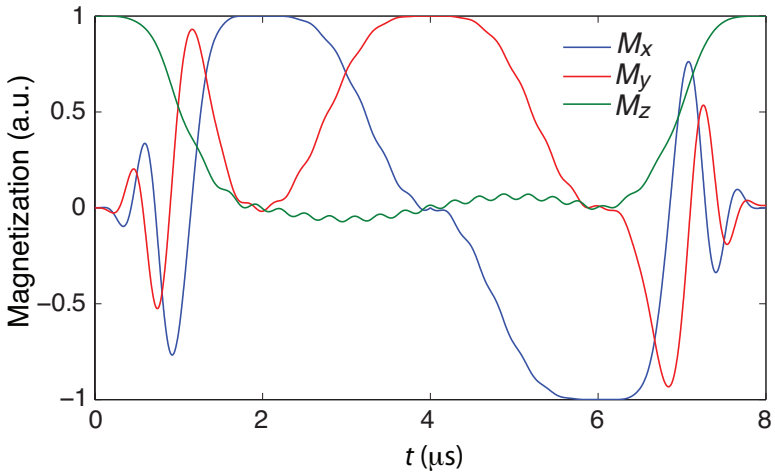

FIGURE 6.2: Simulated evolution of spin magnetization during an adiabatic geometric phase gate of π, measured in the rotating frame of constant frequency ω_R. The parameters used are $\Delta_0 = 2.5$ MHz $\Omega_0 = 1.2$ G, $t_d = 2$ μs, $t_s = 4$ μs.

6.3.3 Strongly driven two-level system

When an electron spin in a static magnetic field B_0 is driven by a weak microwave field B_1 on-resonance with its Zeeman splitting, the population of the two energy levels of the spin will oscillate at the *Rabi frequency*. However, in the regime where B_1 is large enough that the counter-rotating component of the oscillating field cannot be neglected, the rotating wave approximation is no longer valid. The dynamics of such strongly driven two-level system have been studied in some physical systems, such as a superconducting qubit [Oli05] and quantum dot formed by an NV center in diamond [Fuc09].

Figure 6.3 shows the simulated Rabi oscillation of an electron spin 1/2 under weak and strong driving field. Both simulations are carried out in the lab frame without the rotating wave approximation. It is clear that in Figure 6.3 (a) M_z oscillates following a sinusoidal function of t, whereas in Figure 6.3 (b) under the nonlinear driving field the evolution of M_z deviates severely from the sinusoidal oscillation.

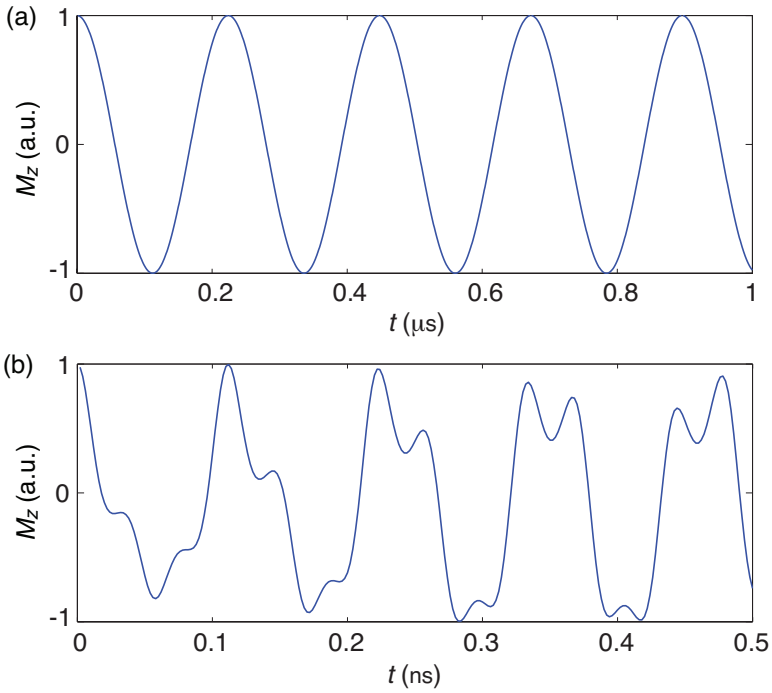

Figure 6.3: Simulated Rabi oscillation of a spin 1/2 under (a) weak and (b) strong driving field. The static field is $B_0 = 3300$ G; the two microwave fields are $B_1 = 1.5$ G and 3000 G, respectively.

6.4 Prospects

The examples given in the previous section show the potential of using the simulation program in various conditions, which provides a more flexible toolbox for simulating pulsed EPR experiments. On the other hand, the fewer constraints on the application of the simulation program usually lead to a higher complexity in the computation, for example the calculation in the lab frame is much slower than that in the rotating frame. Therefore, it is necessary to make a good combination between flexibility and efficiency.

In further development of the simulation program, it would also be useful to include the relaxation effect in the model. This means to introduce the Lindblad operators describing the relaxation processes, and to solve the Lindblad equation (Equation 2.17) instead of von Neumann equation.

7

Conclusions

In this thesis, studies on the hybrid quantum computing scheme with electron spins were presented focusing on the interface between microwave photons and ensembles of electron spins in EPR.

Firstly, I experimentally demonstrated the multimode storage of microwave excitations in a single electron spin ensemble in the form of collective excitation of the spins using magnetic field gradients. Taking the advantage of the large number of spins in the ensemble, multiple microwave pulses are stored in different collective modes of the ensemble created by different magnetic field gradients. The stored microwave pulses can be retrieved later on-demand, therefore the spin ensemble constitutes a holographic quantum RAM of the microwave excitations. I also demonstrate the transfer of the collective coherence between the electron spins and nuclear spins, which can extend the lifetime of the quantum memory from $T_{2\mathrm{e}}$ to $T_{2\mathrm{n}}$. The same principle of the holographic memory can be applied in the hybrid quantum computing scheme where the electron spins are coupled to a superconducting cavity and serve as the long-lived quantum memory.

In order to extend the above experiments towards coherent state transfer between quantum systems, it is interesting to explore strong coupling using the same pulsed EPR cavity. I therefore studied the coupling between an electron spin ensemble and a three-dimensional microwave cavity under different parameters, such as linewidth of the spins, volume of the cavity mode, number of spins coupled to the cavity mode, power of the microwave field. The collective coupling strength is shown to be $\sqrt{N}$-dependent. Even though it is possible to observe the splitting in the reflection spectrum of the cavity at resonance, similar to the vacuum Rabi splitting observed when an atom is strongly coupled to a light field, the couplings achieved in these experiments are not strong enough to guarantee a coherent state transfer between the electron spins and the cavity, limited either by a high decay rate of the cavity (low Q) or by a broad EPR linewidth of the spins (short T_2^*).

In order to look for a more robust gate operation and solve the compatibility problem between pulsed EPR and circuit QED, I studied the control of electron spin states via adiabatic processes in place of dynamic pulses. I established a model for the adiabatic geometric

phase gate based on the concept of Berry phase, and carried out numerical simulations to show that the adiabatic phase operation is robust and immune to the inhomogeneity in the driving microwave field and high frequency fluctuations in the external static field. When the adiabatic condition is well satisfied, the fidelity of the adiabatic geometric phase gate is higher than the dynamic phase gates and similar to the geometric phase gate using composite pulses. In the experiment, however, limited by the amplitude of the microwave field available in the current setup, the adiabatic processes are less ideal. In practise, the adiabatic geometric phase gate shows a similar performance to the geometric phase gate using BB1 composite dynamic pulses.

In a superconducting cavity of much higher Q and smaller cavity mode volume, the adiabatic condition can be achieved at a much lower microwave power than in X-band EPR without introducing extra heating to the superconducting circuit. Therefore, in the proposed hybrid quantum computing scheme, it is possible to apply the adiabatic gates instead of microwave pulses to manipulate the state of the electron spins once the excitations are stored in the spins — the refocusing π pulses can be replaced by adiabatic inversions to achieve the on-demand readout; furthermore, additional decoupling sequences can be applied adiabatically analogous to the dynamic decoupling sequences to fight decoherence of the spins.

Some of the experiments presented in this thesis were also simulated using a program specially designed for pulsed EPR simulation, which provides a way of testing the pulse sequence used in the experiments and analyzing the model of the spin systems. Together with the experimental studies, the results in this thesis showed that the electron spin ensemble is a promising candidate for the long-lived and high capacity memory in the hybrid quantum computing scheme. Further researches in the technique of manipulating the spin state at mK temperature range and the intermediated quantum state transfer between superconducting qubits and spin ensembles at a single photon level are still needed for the implementation of a hybrid quantum processor.

References

[Abe66] Abella, I. D., Kurnit, N. A., Hartmann, S. R., *Phys. Rev.*, **141**, 391 (1966).

[Abr85] Abragam, A., *The Principles of Nuclear Magnetism*, Oxford : Clarendon Press (1985).

[Afz09] Afzelius, M., Simon, C., de Riedmatten, H., Gisin, N., *Phys. Rev. A*, **79**, 052329 (2009).

[Afz10] Afzelius, M., Usmani, I., Amari, A., Lauritzen, B., Walther, A., Simon, C., Sangouard, N., Jiří, M., de Riedmatten, H., Gisin, N., Kröll, S., *Phys. Rev. Lett.*, **104**, 040503 (2010).

[Ale06] Alexander, A. L., Longdell, J. J., Sellars, M. J., Manson, N. B., *Phys. Rev. Lett.*, **96**, 043602 (2006).

[Ale07] Alexander, A., Longdell, J., Sellars, M., Manson, N., *J. Lumin.*, **127**, 94 (2007).

[Ali07] Aliferis, P., Cross, A. W., *Phys. Rev. Lett.*, **98**, 220502 (2007).

[Ams11] Amsüss, R., Koller, C., Nöbauer, T., Putz, S., Rotter, S., Sandner, K., Schneider, S., Schramböck, M., Steinhauser, G., Ritsch, H., Schmiedmayer, J., Majer, J., *Phys. Rev. Lett.*, **107**, 060502 (2011).

[And06] Andre, A., DeMille, D., Doyle, J. M., Lukin, M. D., Maxwell, S. E., Rabl, P., Schoelkopf, R. J., Zoller, P., *Nat. Phys.*, **2**, 636 (2006).

[Bac06] Bacon, D., *Phys. Rev. A*, **73**, 012340 (2006).

[Ben80] Benioff, P., *J. Stat. Phys.*, **22**, 563 (1980).

[Ber84] Berry, M. V., *Proc. R. Soc. London. A*, **392**, 45 (1984).

[Ber03] Berkley, A. J., Xu, H., Ramos, R. C., Gubrud, M. A., Strauch, F. W., Johnson, P. R., Anderson, J. R., Dragt, A. J., Lobb, C. J., Wellstood, F. C., *Science*, **300**, 1548 (2003).

[Bla04] Blais, A., Huang, R.-S., Wallraff, A., Girvin, S. M., Schoelkopf, R. J., *Phys. Rev. A*, **69**, 062320 (2004).

[Bla09] Blakestad, R. B., Ospelkaus, C., VanDevender, A. P., Amini, J. M., Britton, J., Leibfried, D., Wineland, D. J., *Phys. Rev. Lett.*, **102**, 153002 (2009).

[Boc04] Boca, A., Miller, R., Birnbaum, K. M., Boozer, A. D., McKeever, J., Kimble, H. J., *Phys. Rev. Lett.*, **93**, 233603 (2004).

[Boo07] Boozer, A. D., Boca, A., Miller, R., Northup, T. E., Kimble, H. J., *Phys. Rev. Lett.*, **98**, 193601 (2007).

[Bri98a] Briegel, H.-J., Dür, W., Cirac, J. I., Zoller, P., *Phys. Rev. Lett.*, **81**, 5932 (1998).

[Bri98b] Brinkmann, M., Turek, P., Andre, J.-j., *J. Mater. Chem.*, **8**, 675 (1998).

[Bri07] Brion, E., Molmer, K., Saffman, M., *Phys. Rev. Lett.*, **99**, 260501 (2007).

[Bru96] Brune, M., Schmidt-Kaler, F., Maali, A., Dreyer, J., Hagley, E., Raimond, J. M., Haroche, S., *Phys. Rev. Lett.*, **76**, 1800 (1996).

[Bud99] Budker, D., Kimball, D. F., Rochester, S. M., Yashchuk, V. V., *Phys. Rev. Lett.*, **83**, 1767 (1999).

[Bus11] Bushev, P., Feofanov, A. K., Rotzinger, H., Protopopov, I., Cole, J. H., Wilson, C. M., Fischer, G., Lukashenko, A., Ustinov, A. V., *Phys. Rev. B*, **84**, 060501 (2011).

[Car54] Carr, H. Y., Purcell, E. M., *Phys. Rev.*, **94**, 630 (1954).

[Cha05] Chaneliere, T., Matsukevich, D. N., Jenkins, S. D., Lan, S.-Y., Kennedy, T. A. B., Kuzmich, A., *Nature*, **438**, 833 (2005).

[Che06] Chen, S., Chen, Y.-A., Strassel, T., Yuan, Z.-S., Zhao, B., Schmiedmayer, J., Pan, J.-W., *Phys. Rev. Lett.*, **97**, 173004 (2006).

[Che07] Chen, Z.-B., Zhao, B., Chen, Y.-A., Schmiedmayer, J., Pan, J.-W., *Phys. Rev. A*, **76**, 022329 (2007).

[Che08] Chen, Y.-A., Chen, S., Yuan, Z.-S., Zhao, B., Chuu, C.-S., Schmiedmayer, J., Pan, J.-W., *Nat. Phys.*, **4**, 103 (2008).

[Chi01] Childs, A. M., Farhi, E., Preskill, J., *Phys. Rev. A*, **65**, 012322 (2001).

[Chi10] Chiorescu, I., Groll, N., Bertaina, S., Mori, T., Miyashita, S., *Phys. Rev. B*, **82**, 024413 (2010).

[Cho04] Chou, C. W., Polyakov, S. V., Kuzmich, A., Kimble, H. J., *Phys. Rev. Lett.*, **92**, 213601 (2004).

[Cho05] Chou, C. W., de Riedmatten, H., Felinto, D., Polyakov, S. V., van Enk, S. J., Kimble, H. J., *Nature*, **438**, 409 (2005).

[Cho07] Chou, C.-W., Laurat, J., Deng, H., Choi, K. S., de Riedmatten, H., Felinto, D., Kimble, H. J., *Science*, **316**, 1316 (2007).

[Cho08] Choi, K. S., Deng, H., Laurat, J., Kimble, H. J., *Nature*, **452**, 67 (2008).

[Chu95] Chuang, I. L., Yamamoto, Y., *Phys. Rev. A*, **52**, 3489 (1995).

[Chu08] Chuu, C.-S., Strassel, T., Zhao, B., Koch, M., Chen, Y.-A., Chen, S., Yuan, Z.-S., Schmiedmayer, J., Pan, J.-W., *Phys. Rev. Lett.*, **101**, 120501 (2008).

[Cir95] Cirac, J. I., Zoller, P., *Phys. Rev. Lett.*, **74**, 4091 (1995).

[Cir97] Cirac, J. I., Zoller, P., Kimble, H. J., Mabuchi, H., *Phys. Rev. Lett.*, **78**, 3221 (1997).

[Cla08] Clarke, J., Wilhelm, F. K., *Nature*, **453**, 1031 (2008).

[Cla11] Clausen, C., Usmani, I., Bussieres, F., Sangouard, N., Afzelius, M., de Riedmatten, H., Gisin, N., *Nature*, **469**, 508 (2011).

[Cor97] Cory, D. G., Fahmy, A. F., Havel, T. F., *Proc. Natl. Acad. Sci. USA*, **94**, 1634 (1997).

[DAr00] D'Ariano, G., Macchiavello, C., Maccone, L., *Fortschr. Phys.*, **48**, 573 (2000).

[Deu85] Deutsch, D., *Proc. R. Soc. London, Ser. A*, **400**, 97 (1985).

[Dic54] Dicke, R. H., *Phys. Rev.*, **93**, 99 (1954).

[DiC09] DiCarlo, L., Chow, J. M., Gambetta, J. M., Bishop, L. S., Johnson, B. R., Schuster, D. I., Majer, J., Blais, A., Frunzio, L., Girvin, S. M., Schoelkopf, R. J., *Nature*, **460**, 240 (2009).

[DiC10] DiCarlo, L., Reed, M. D., Sun, L., Johnson, B. R., Chow, J. M., Gambetta, J. M., Frunzio, L., Girvin, S. M., Devoret, M. H., Schoelkopf, R. J., *Nature*, **467**, 574 (2010).

[DiV00] DiVincenzo, D. P., *Fortschr. Phys.*, **48**, 771 (2000).

[Dua00] Duan, L.-M., Cirac, J. I., Zoller, P., Polzik, E. S., *Phys. Rev. Lett.*, **85**, 5643 (2000).

[Dua01] Duan, L.-M., Lukin, M. D., Cirac, J. I., Zoller, P., *Nature*, **414**, 413 (2001).

[Dur00] Dür, W., Vidal, G., Cirac, J. I., *Phys. Rev. A*, **62**, 062314 (2000).

[Dut07] Dutt, M. V. G., Childress, L., Jiang, L., Togan, E., Maze, J., Jelezko, F., Zibrov, A. S., Hemmer, P. R., Lukin, M. D., *Science*, **316**, 1312 (2007).

[Eis05] Eisaman, M. D., Andre, A., Massou, F., Fleischhauer, M., Zibrov, A. S., Lukin, M. D., *Nature*, **438**, 837 (2005).

[Eke00] Ekert, A., Ericsson, M., Hayden, P., Inamori, H., Jones, J. A., Oi, D. K. L., Vedral, V., *J. Mod. Opt.*, **47**, 2501 (2000).

[Feh59] Feher, G., *Phys. Rev.*, **114**, 1219 (1959).

[Fey82] Feynman, R. P., *Intl. J. Theo. Phys.*, **21**, 467 (1982).

[Fil09] Filipp, S., Klepp, J., Hasegawa, Y., Plonka-Spehr, C., Schmidt, U., Geltenbort, P., Rauch, H., *Phys. Rev. Lett.*, **102**, 030404 (2009).

[Fin09] Fink, J. M., Bianchetti, R., Baur, M., Göppl, M., Steffen, L., Filipp, S., Leek, P. J., Blais, A., Wallraff, A., *Phys. Rev. Lett.*, **103**, 083601 (2009).

[Fle00] Fleischhauer, M., Lukin, M. D., *Phys. Rev. Lett.*, **84**, 5094 (2000).

[Fle05] Fleischhauer, M., Imamoglu, A., Marangos, J. P., *Rev. Mod. Phys.*, **77**, 633 (2005).

[Fri00] Friedman, J. R., Patel, V., Chen, W., Tolpygo, S. K., Lukens, J. E., *Nature*, **406**, 43 (2000).

[Fru05] Frunzio, L., Wallraff, A., Schuster, D., Majer, J., Schoelkopf, R., *Applied Superconductivity, IEEE Transactions on*, **15**, 860 (2005).

[Fuc09] Fuchs, G. D., Dobrovitski, V. V., Toyli, D. M., Heremans, F. J., Awschalom, D. D., *Science*, **326**, 1520 (2009).

[Gau90] Gaubatz, U., Rudecki, P., Schiemann, S., Bergmann, K., *J. Chem. Phys.*, **92**, 5363 (1990).

[Ger97] Gershenfeld, N. A., Chuang, I. L., *Science*, **275**, 350 (1997).

[Gor07a] Gorshkov, A. V., Andre, A., Fleischhauer, M., Sorensen, A. S., Lukin, M. D., *Phys. Rev. Lett.*, **98**, 123601 (2007).

[Gor07b] Gorshkov, A. V., Andre, A., Lukin, M. D., Sorensen, A. S., *Phys. Rev. A*, **76**, 033806 (2007).

[Gor08] Gorshkov, A. V., Calarco, T., Lukin, M. D., Sorensen, A. S., *Phys. Rev. A*, **77**, 043806 (2008).

[Gos10] Gossuin, Y., Hocq, A., Gillis, P., Vuong, Q. L., *J. Phys. D: Appl. Phys.*, **43**, 213001 (2010).

[Gou09] Gouet, J.-L. L., Berman, P. R., *Phys. Rev. A*, **80**, 012320 (2009).

[Gro96] Grover, L. K., in *Proceedings of 28th annual ACM symposium onTheory of computing*, 212, New York, USA (1996).

[Gro97] Grover, L. K., *Phys. Rev. Lett.*, **79**, 4709 (1997).

[Hah50] Hahn, E. L., *Phys. Rev.*, **80**, 580 (1950).

[Hal99] Hald, J., Sørensen, J. L., Schori, C., Polzik, E. S., *Phys. Rev. Lett.*, **83**, 1319 (1999).

[Ham97] Ham, B., Hemmer, P., Shahriar, M., *Opt. Commun.*, **144**, 227 (1997).

[Ham04] Hammerer, K., Mølmer, K., Polzik, E. S., Cirac, J. I., *Phys. Rev. A*, **70**, 044304 (2004).

[Ham09] Ham, B. S., *Nat. Photonics*, **3**, 518 (2009).

[Han09] Hanson, G. R., Noble, C. J., Benson, S., *High Resolution EPR*, p.105–173, Biological Magnetic Resonance, Springer New York (2009).

[Har92] Harris, S. E., Field, J. E., Kasapi, A., *Phys. Rev. A*, **46**, R29 (1992).

[Har97] Harris, S. E., *Physics Today*, **50**, 36 (1997).

[Har02] Harneit, W., *Phys. Rev. A*, **65**, 032322 (2002).

[Hau99] Hau, L. V., Harris, S. E., Dutton, Z., Behroozi, C. H., *Nature*, **397**, 594 (1999).

[Hen00] Hennrich, M., Legero, T., Kuhn, A., Rempe, G., *Phys. Rev. Lett.*, **85**, 4872 (2000).

[Her09] Herskind, P. F., Dantan, A., Marler, J. P., Albert, M., Drewsen, M., *Nat. Phys.*, **5**, 494 (2009).

[Het08a] Hétet, G., Longdell, J. J., Alexander, A. L., Lam, P. K., Sellars, M. J., *Phys. Rev. Lett.*, **100**, 023601 (2008).

[Het08b] Hétet, G., Hosseini, M., Sparkes, B. M., Oblak, D., Lam, P. K., Buchler, B. C., *Opt. Lett.*, **33**, 2323 (2008).

[Hof09] Hofheinz, M., Wang, H., Ansmann, M., Bialczak, R. C., Lucero, E., Neeley, M., O'Connell, A. D., Sank, D., Wenner, J., Martinis, J. M., Cleland, A. N., *Nature*, **459**, 546 (2009).

[Hom09] Home, J. P., Hanneke, D., Jost, J. D., Amini, J. M., Leibfried, D., Wineland, D. J., *Science*, **325**, 1227 (2009).

[Hoo00] Hood, C. J., Lynn, T. W., Doherty, A. C., Parkins, A. S., Kimble, H. J., *Science*, **287**, 1447 (2000).

[Hos09] Hosseini, M., Sparkes, B. M., Hetet, G., Longdell, J. J., Lam, P. K., Buchler, B. C., *Nature*, **461**, 241 (2009).

[Ila00] Ilangovan, G., Zweier, J. L., Kuppusamy, P., *J. Phys. Chem. B*, **104**, 4047 (2000).

[Ima09] Imamoglu, A., *Phys. Rev. Lett.*, **102**, 083602 (2009).

[Jon00] Jones, J. A., Vedral, V., Ekert, A., Castagnoli, G., *Nature*, **403**, 869 (2000).

[Jon01] Jones, J. A., *Prog. Nucl. Magn. Reson. Spectrosc.*, **38**, 325 (2001).

[Jul04] Julsgaard, B., Sherson, J., Cirac, J. I., Fiurasek, J., Polzik, E. S., *Nature*, **432**, 482 (2004).

[Kan98] Kane, B. E., *Nature*, **393**, 133 (1998).

[Kas95] Kasapi, A., Jain, M., Yin, G. Y., Harris, S. E., *Phys. Rev. Lett.*, **74**, 2447 (1995).

[Kas99] Kash, M. M., Sautenkov, V. A., Zibrov, A. S., Hollberg, L., Welch, G. R., Lukin, M. D., Rostovtsev, Y., Fry, E. S., Scully, M. O., *Phys. Rev. Lett.*, **82**, 5229 (1999).

[Kat50] Kato, T., *Journal of the Physical Society of Japan*, **5**, 435 (1950).

[Kel04] Keller, M., Lange, B., Hayasaka, K., Lange, W., Walther, H., *Nature*, **431**, 1075 (2004).

[Kho05] Khodjasteh, K., Lidar, D. A., *Phys. Rev. Lett.*, **95**, 180501 (2005).

[Kim98] Kimble, H. J., *Phys. Scr.*, **T76**, 127 (1998).

[Kim08] Kimble, H. J., *Nature*, **453**, 1023 (2008).

[Kni01] Knill, E., Laflamme, R., Milburn, G. J., *Nature*, **409**, 46 (2001).

[Koc01] Kocharovskaya, O., Rostovtsev, Y., Scully, M. O., *Phys. Rev. Lett.*, **86**, 628 (2001).

[Koz00] Kozhekin, A. E., Mølmer, K., Polzik, E., *Phys. Rev. A*, **62**, 033809 (2000).

[Kra06] Kraus, B., Tittel, W., Gisin, N., Nilsson, M., Kroll, S., Cirac, J. I., *Phys. Rev. A*, **73**, 020302 (2006).

[Kub10] Kubo, Y., Ong, F. R., Bertet, P., Vion, D., Jacques, V., Zheng, D., Dréau, A., Roch, J.-F., Auffeves, A., Jelezko, F., Wrachtrup, J., Barthe, M. F., Bergonzo, P., Esteve, D., *Phys. Rev. Lett.*, **105**, 140502 (2010).

[Kub11] Kubo, Y., Grezes, C., Dewes, A., Umeda, T., Isoya, J., Sumiya, H., Morishita, N., Abe, H., Onoda, S., Ohshima, Jacques, V., Dréau, A., Roch, J.-F., Diniz, I., Auffeves, A., Vion, D., Esteve, D., Bertet, P., arXiv:1110.2978v1 (2011).

[Kuh02] Kuhn, A., Hennrich, M., Rempe, G., *Phys. Rev. Lett.*, **89**, 067901 (2002).

[Kuk89] Kuklinski, J. R., Gaubatz, U., Hioe, F. T., Bergmann, K., *Phys. Rev. A*, **40**, 6741 (1989).

[Kuz97] Kuzmich, A., Mølmer, K., Polzik, E. S., *Phys. Rev. Lett.*, **79**, 4782 (1997).

[Kuz03] Kuzmich, A., Bowen, W. P., Boozer, A. D., Boca, A., Chou, C. W., Duan, L.-M., Kimble, H. J., *Nature*, **423**, 731 (2003).

[Lad10] Ladd, T. D., Jelezko, F., Laflamme, R., Nakamura, Y., Monroe, C., O'Brien, J. L., *Nature*, **464**, 45 (2010).

[Lau09] Laurat, J., *Physics*, **2**, 62 (2009).

[Lau10] Lauritzen, B., Minář, J. c. v., de Riedmatten, H., Afzelius, M., Sangouard, N., Simon, C., Gisin, N., *Phys. Rev. Lett.*, **104**, 080502 (2010).

[Lee07] Leek, P. J., Fink, J. M., Blais, A., Bianchetti, R., Goppl, M., Gambetta, J. M., Schuster, D. I., Frunzio, L., Schoelkopf, R. J., Wallraff, A., *Science*, **318**, 1889 (2007).

[Lee08] Lee, J., Park, J., Lee, S. M., Lee, H.-W., Khosa, A. H., *Phys. Rev. A*, **77**, 032327 (2008).

[Lev86] Levitt, M. H., *Prog. Nucl. Magn. Reson. Spectrosc.*, **18**, 61 (1986).

[Liu01] Liu, C., Dutton, Z., Behroozi, C. H., Hau, L. V., *Nature*, **409**, 490 (2001).

[Llo93] Lloyd, S., *Science*, **261**, 1569 (1993).

[Lon05] Longdell, J. J., Fraval, E., Sellars, M. J., Manson, N. B., *Phys. Rev. Lett.*, **95**, 063601 (2005).

[Lon08] Longdell, J. J., Hetet, G., Lam, P. K., Sellars, M. J., *Phys. Rev. A*, **78**, 032337 (2008).

[Loo10] van Loock, P., *Laser & Photon. Rev.*, **5**, 167 (2010).

[Los98] Loss, D., DiVincenzo, D. P., *Phys. Rev. A*, **57**, 120 (1998).

[Luk00] Lukin, M. D., Yelin, S. F., Fleischhauer, M., *Phys. Rev. Lett.*, **84**, 4232 (2000).

[Luk01] Lukin, M. D., Imamoglu, A., *Nature*, **413**, 273 (2001).

[Luk03] Lukin, M. D., *Rev. Mod. Phys.*, **75**, 457 (2003).

[Lup09] Lupo, C., Aniello, P., *Phys. Scr.*, **79**, 065012 (5pp) (2009).

[Mad02] Madi, Z., Van Doorslaer, S., Schweiger, A., *J. Magn. Reson.*, **154**, 181 (2002).

[Mai02] Mair, A., Hager, J., Phillips, D. F., Walsworth, R. L., Lukin, M. D., *Phys. Rev. A*, **65**, 031802 (2002).

[Maj07] Majer, J., Chow, J. M., Gambetta, J. M., Koch, J., Johnson, B. R., Schreier, J. A., Frunzio, L., Schuster, D. I., Houck, A. A., Wallraff, A., Blais, A., Devoret, M. H., Girvin, S. M., Schoelkopf, R. J., *Nature*, **449**, 443 (2007).

[Mak01] Makhlin, Y., Schön, G., Shnirman, A., *Rev. Mod. Phys.*, **73**, 357 (2001).

[Mar02] Martinis, J. M., Nam, S., Aumentado, J., Urbina, C., *Phys. Rev. Lett.*, **89**, 117901 (2002).

[Mat06] Matsukevich, D. N., Chaneliere, T., Jenkins, S. D., Lan, S.-Y., Kennedy, T. A. B., Kuzmich, A., *Phys. Rev. Lett.*, **97**, 013601 (2006).

[Mau09] Maunz, P., Olmschenk, S., Hayes, D., Matsukevich, D. N., Duan, L.-M., Monroe, C., *Phys. Rev. Lett.*, **102**, 250502 (2009).

[McK03] McKeever, J., Buck, J. R., Boozer, A. D., Kuzmich, A., Nägerl, H.-C., Stamper-Kurn, D. M., Kimble, H. J., *Phys. Rev. Lett.*, **90**, 133602 (2003).

[McK04] McKeever, J., Boca, A., Boozer, A. D., Miller, R., Buck, J. R., Kuzmich, A., Kimble, H. J., *Science*, **303**, 1992 (2004).

[Mei58] Meiboom, S., *Rev. Sci. Instrum.*, **29**, 688 (1958).

[Mil05] Miller, R., Northup, T. E., Birnbaum, K. M., Boca, A., Boozer, A. D., Kimble, H. J., *J. Phys. B: At. Mol. Opt. Phys.*, **38**, S551 (2005).

[Mis08] Mishina, O. S., Larionov, N. V., Sheremet, A. S., Sokolov, I. M., Kupriyanov, D. V., *Phys. Rev. A*, **78**, 042313 (2008).

[Mit92] Mitsunaga, M., *Opt. Quantum Electron.*, **24**, 1137 (1992).

[Moe07] Moehring, D. L., Maunz, P., Olmschenk, S., Younge, K. C., Matsukevich, D. N., Duan, L.-M., Monroe, C., *Nature*, **449**, 68 (2007).

[Moi01] Moiseev, S. A., Kröll, S., *Phys. Rev. Lett.*, **87**, 173601 (2001).

[Moi03] Moiseev, S. A., Tarasov, V. F., Ham, B. S., *J. Opt. B: Quantum Semiclassical Opt.*, **5**, S497 (2003).

[Moi08] Moiseev, S. A., Arslanov, N. M., *Phys. Rev. A*, **78**, 023803 (2008).

[Mol99] Mølmer, K., Sørensen, A., *Phys. Rev. Lett.*, **82**, 1835 (1999).

[Mon95] Monroe, C., Meekhof, D. M., King, B. E., Itano, W. M., Wineland, D. J., *Phys. Rev. Lett.*, **75**, 4714 (1995).

[Mor05a] Morton, J. J. L., Tyryshkin, A. M., Ardavan, A., Porfyrakis, K., Lyon, S. A., Briggs, G. A. D., *Phys. Rev. Lett.*, **95**, 200501 (2005).

[Mor05b] Morton, J. J. L., Tyryshkin, A. M., Ardavan, A., Porfyrakis, K., Lyon, S. A., Briggs, G. A. D., *Phys. Rev. A*, **71**, 012332 (2005).

[Mor06] Morton, J. J. L., Tyryshkin, A. M., Ardavan, A., Porfyrakis, K., Lyon, S. A., Briggs, G. A. D., *J. Chem. Phys.*, **124**, 014508 (2006).

[Mor08] Morton, J. J. L., Tyryshkin, A. M., Brown, R. M., Shankar, S., Lovett, B. W., Ardavan, A., Schenkel, T., Haller, E. E., Ager, J. W., Lyon, S. A., *Nature*, **455**, 1085 (2008).

[Mor11] Morton, J. J., Lovett, B. W., *Annual Review of Condensed Matter Physics*, **2**, 189 (2011).

[Mos82] Mossberg, T. W., *Opt. Lett.*, **7**, 77 (1982).

[Naz02] Nazir, A., Spiller, T. P., Munro, W. J., *Phys. Rev. A*, **65**, 042303 (2002).

[Nee10] Neeley, M., Bialczak, R. C., Lenander, M., Lucero, E., Mariantoni, M., O/'Connell, A. D., Sank, D., Wang, H., Weides, M., Wenner, J., Yin, Y., Yamamoto, T., Cleland, A. N., Martinis, J. M., *Nature*, **467**, 570 (2010).

[Nil05] Nilsson, M., Kröll, S., *Opt. Commun.*, **247**, 393 (2005).

[Nov07] Novikova, I., Gorshkov, A. V., Phillips, D. F., Sorensen, A. S., Lukin, M. D., Walsworth, R. L., *Phys. Rev. Lett.*, **98**, 243602 (2007).

[Nov08] Novikova, I., Phillips, N. B., Gorshkov, A. V., *Phys. Rev. A*, **78**, 021802 (2008).

[Nun07] Nunn, J., Walmsley, I. A., Raymer, M. G., Surmacz, K., Waldermann, F. C., Wang, Z., Jaksch, D., *Phys. Rev. A*, **75**, 011401 (2007).

[Nun08] Nunn, J., Reim, K., Lee, K. C., Lorenz, V. O., Sussman, B. J., Walmsley, I. A., Jaksch, D., *Phys. Rev. Lett.*, **101**, 260502 (2008).

[OBr03] O'Brien, J. L., Pryde, G. J., White, A. G., Ralph, T. C., Branning, D., *Nature*, **426**, 264 (2003).

[Oli05] Oliver, W. D., Yu, Y., Lee, J. C., Berggren, K. K., Levitov, L. S., Orlando, T. P., *Science*, **310**, 1653 (2005).

[Olm09] Olmschenk, S., Matsukevich, D. N., Maunz, P., Hayes, D., Duan, L.-M., Monroe, C., *Science*, **323**, 486 (2009).

[Pas03] Pashkin, Y. A., Yamamoto, T., Astafiev, O., Nakamura, Y., Averin, D. V., Tsai, J. S., *Nature*, **421**, 823 (2003).

[Pet08] Petrosyan, D., Fleischhauer, M., *Phys. Rev. Lett.*, **100**, 170501 (2008).

[Pet09] Petrosyan, D., Bensky, G., Kurizki, G., Mazets, I., Majer, J., Schmiedmayer, J., *Phys. Rev. A*, **79**, 040304 (2009).

[Phi01] Phillips, D. F., Fleischhauer, A., Mair, A., Walsworth, R. L., Lukin, M. D., *Phys. Rev. Lett.*, **86**, 783 (2001).

[Pir11] Piro, N., Rohde, F., Schuck, C., Almendros, M., Huwer, J., Ghosh, J., Haase, A., Hennrich, M., Dubin, F., Eschner, J., *Nat Phys*, **7**, 17 (2011).

[Pla07] Plantenberg, J. H., de Groot, P. C., Harmans, C. J. P. M., Mooij, J. E., *Nature*, **447**, 836 (2007).

[Rab06] Rabl, P., DeMille, D., Doyle, J. M., Lukin, M. D., Schoelkopf, R. J., Zoller, P., *Phys. Rev. Lett.*, **97**, 033003 (2006).

[Ray81] Raymer, M. G., Mostowski, J., *Phys. Rev. A*, **24**, 1980 (1981).

[Rei10] Reim, K. F., Nunn, J., Lorenz, V. O., Sussman, B. J., Lee, K. C., Langford, N. K., Jaksch, D., Walmsley, I. A., *Nat. Photonics*, **4**, 218 (2010).

[Rei11] Reim, K. F., Michelberger, P., Lee, K. C., Nunn, J., Langford, N. K., Walmsley, I. A., *Phys. Rev. Lett.*, **107**, 053603 (2011).

[Rie08] de Riedmatten, H., Afzelius, M., Staudt, M. U., Simon, C., Gisin, N., *Nature*, **456**, 773 (2008).

[Rya10] Ryan, C. A., Hodges, J. S., Cory, D. G., *Phys. Rev. Lett.*, **105**, 200402 (2010).

[San07] Sangouard, N., Simon, C., Afzelius, M., Gisin, N., *Phys. Rev. A*, **75**, 032327 (2007).

[San11] Sangouard, N., Simon, C., de Riedmatten, H., Gisin, N., *Rev. Mod. Phys.*, **83**, 33 (2011).

[Sch01] Schweiger, A., Jeschke, G., *Principles of Pulse Electron Paramagnetic Resonance*, Oxford University Press (2001).

[Sch02] Schori, C., Julsgaard, B., Sørensen, J. L., Polzik, E. S., *Phys. Rev. Lett.*, **89**, 057903 (2002).

[Sch07] Schuster, D. I., Houck, A. A., Schreier, J. A., Wallraff, A., Gambetta, J. M., Blais, A., Frunzio, L., Majer, J., Johnson, B., Devoret, M. H., Girvin, S. M., Schoelkopf, R. J., *Nature*, **445**, 515 (2007).

[Sch09] Schnorrberger, U., Thompson, J. D., Trotzky, S., Pugatch, R., Davidson, N., Kuhr, S., Bloch, I., *Phys. Rev. Lett.*, **103**, 033003 (2009).

[Sch10] Schuster, D. I., Sears, A. P., Ginossar, E., DiCarlo, L., Frunzio, L., Morton, J. J. L., Wu, H., Briggs, G. A. D., Buckley, B. B., Awschalom, D. D., Schoelkopf, R. J., *Phys. Rev. Lett.*, **105**, 140501 (2010).

[Scu97] Scully, M. O., Zubairy, M. S., *Quantum Optics*, Cambridge : Cambridge University Press (1997).

[She06] Sherson, J. F., Krauter, H., Olsson, R. K., Julsgaard, B., Hammerer, K., Cirac, I., Polzik, E. S., *Nature*, **443**, 557 (2006).

[Sho94] Shor, P. W., in *Proceedings of 35th Annual ACM Symposium on Foundations of Computer Science* (1994).

[Sil07] Sillanpaa, M. A., Park, J. I., Simmonds, R. W., *Nature*, **449**, 438 (2007).

[Sim07a] Simon, C., de Riedmatten, H., Afzelius, M., Sangouard, N., Zbinden, H., Gisin, N., *Phys. Rev. Lett.*, **98**, 190503 (2007).

[Sim07b] Simon, J., Tanji, H., Ghosh, S., Vuletic, V., *Nat. Phys.*, **3**, 765 (2007).

[Sor84] Sørensen, O., Eich, G., Levitt, M., Bodenhausen, G., Ernst, R., *Prog. Nucl. Magn. Reson. Spectrosc.*, **16**, 163 (1984).

[Sor04] Sørensen, A. S., van der Wal, C. H., Childress, L. I., Lukin, M. D., *Phys. Rev. Lett.*, **92**, 063601 (2004).

[Sou11] Souza, A. M., Álvarez, G. A., Suter, D., *Phys. Rev. Lett.*, **106**, 240501 (2011).

[Spe11] Specht, H. P., Nolleke, C., Reiserer, A., Uphoff, M., Figueroa, E., Ritter, S., Rempe, G., *Nature*, **473**, 190 (2011).

[Sta07a] Staudt, M. U., Afzelius, M., de Riedmatten, H., Hastings-Simon, S. R., Simon, C., Ricken, R., Suche, H., Sohler, W., Gisin, N., *Phys. Rev. Lett.*, **99**, 173602 (2007).

[Sta07b] Staudt, M. U., Hastings-Simon, S. R., Nilsson, M., Afzelius, M., Scarani, V., Ricken, R., Suche, H., Sohler, W., Tittel, W., Gisin, N., *Phys. Rev. Lett.*, **98**, 113601 (2007).

[Ste99] Steane, A. M., *Nature*, **399**, 124 (1999).

[Ste10] Steffen, M., Kumar, S., DiVincenzo, D. P., Rozen, J. R., Keefe, G. A., Rothwell, M. B., Ketchen, M. B., *Phys. Rev. Lett.*, **105**, 100502 (2010).

[Sto03] Stoll, S., Schweiger, A., *Chem. Phys. Lett.*, **380**, 464 (2003).

[Sto06] Stoll, S., Schweiger, A., *J. Magn. Reson.*, **178**, 42 (2006).

[Sto09] Stoll, S., Britt, R. D., *Phys. Chem. Chem. Phys.*, **11**, 6614 (2009).

[Sur08] Surmacz, K., Nunn, J., Reim, K., Lee, K. C., Lorenz, V. O., Sussman, B., Walmsley, I. A., Jaksch, D., *Phys. Rev. A*, **78**, 033806 (2008).

[Szo98] Szosenfogel, R., Goldfarb, D., *Mol. Phys.*, **95**, 1295 (1998).

[Tan09] Tanji, H., Ghosh, S., Simon, J., Bloom, B., Vuletic, V., *Phys. Rev. Lett.*, **103**, 043601 (2009).

[Tav68] Tavis, M., Cummings, F. W., *Phys. Rev.*, **170**, 379 (1968).

[Tay03] Taylor, J. M., Marcus, C. M., Lukin, M. D., *Phys. Rev. Lett.*, **90**, 206803 (2003).

[Tia04] Tian, L., Rabl, P., Blatt, R., Zoller, P., *Phys. Rev. Lett.*, **92**, 247902 (2004).

[Tor08a] Tordrup, K., Molmer, K., *Phys. Rev. A*, **77**, 020301 (2008).

[Tor08b] Tordrup, K., Negretti, A., Molmer, K., *Phys. Rev. Lett.*, **101**, 040501 (2008).

[Tur01] Turukhin, A. V., Sudarshanam, V. S., Shahriar, M. S., Musser, J. A., Ham, B. S., Hemmer, P. R., *Phys. Rev. Lett.*, **88**, 023602 (2001).

[Tyr06] Tyryshkin, A. M., Morton, J. J. L., Benjamin, S. C., Ardavan, A., Briggs, G. A. D., Ager, J. W., Lyon, S. A., *J. Phys. Condens. Matter*, **18**, S783 (2006).

[Tyr10] Tyryshkin, A. M., Wang, Z.-H., Zhang, W., Haller, E. E., Ager, J. W., Dobrovitski, V. V., Lyon, S. A., arXiv:1011.1903v2 (2010).

[Usm10] Usmani, I., Afzelius, M., de Riedmatten, H., Gisin, N., *Nat. Commun.*, **1**, 1 (2010).

[Vio99] Viola, L., Knill, E., Lloyd, S., *Phys. Rev. Lett.*, **82**, 2417 (1999).

[Vio02] Vion, D., Aassime, A., Cottet, A., Joyez, P., Pothier, H., Urbina, C., Esteve, D., Devoret, M. H., *Science*, **296**, 886 (2002).

[Vri00] Vrijen, R., Yablonovitch, E., Wang, K., Jiang, H. W., Balandin, A., Roychowdhury, V., Mor, T., DiVincenzo, D., *Phys. Rev. A*, **62**, 012306 (2000).

[Wal00] van der Wal, C. H., ter Haar, A. C. J., Wilhelm, F. K., Schouten, R. N., Harmans, C. J. P. M., Orlando, T. P., Lloyd, S., Mooij, J. E., *Science*, **290**, 773 (2000).

[Wal03] van der Wal, C. H., Eisaman, M. D., Andre, A., Walsworth, R. L., Phillips, D. F., Zibrov, A. S., Lukin, M. D., *Science*, **301**, 196 (2003).

[Wal04] Wallraff, A., Schuster, D. I., Blais, A., Frunzio, L., Huang, R.-S., Majer, J., Kumar, S., Girvin, S. M., Schoelkopf, R. J., *Nature*, **431**, 162 (2004).

[Wal06] Walther, H., Varcoe, B. T. H., Englert, B.-G., Becker, T., *Rep. Prog. Phys.*, **69**, 1325 (2006).

[Wal09] Wallquist, M., Hammerer, K., Rabl, P., Lukin, M., Zoller, P., *Phys. Scr.*, **2009**, 014001 (2009).

[Wan11] Wang, H., Mariantoni, M., Bialczak, R. C., Lenander, M., Lucero, E., Neeley, M., O'Connell, A. D., Sank, D., Weides, M., Wenner, J., Yamamoto, T., Yin, Y., Zhao, J., Martinis, J. M., Cleland, A. N., *Phys. Rev. Lett.*, **106**, 060401 (2011).

[War88] Warren, W., *Science*, **242**, 878 (1988).

[Wei07] Weil, J. A., Bolton, J. R., *Electron Paramagnetic Resonance : Elementary Theory and Practical Applications*, Hoboken, N.J. : Wiley (2007).

[Wes09] Wesenberg, J. H., Ardavan, A., Briggs, G. A. D., Morton, J. J. L., Schoelkopf, R. J., Schuster, D. I., Molmer, K., *Phys. Rev. Lett.*, **103**, 070502 (2009).

[Wil07] Wilk, T., Webster, S. C., Kuhn, A., Rempe, G., *Science*, **317**, 488 (2007).

[Wim94] Wimperis, S., *J. Magn. Reson., Ser. A*, **109**, 221 (1994).

[Xia95] Xiao, M., Li, Y.-q., Jin, S.-z., Gea-Banacloche, J., *Phys. Rev. Lett.*, **74**, 666 (1995).

[Yam03] Yamamoto, T., Pashkin, Y. A., Astafiev, O., Nakamura, Y., Tsai, J. S., *Nature*, **425**, 941 (2003).

[Ye99] Ye, J., Vernooy, D. W., Kimble, H. J., *Phys. Rev. Lett.*, **83**, 4987 (1999).

[Zha07] Zhao, B., Chen, Z.-B., Chen, Y.-A., Schmiedmayer, J., Pan, J.-W., *Phys. Rev. Lett.*, **98**, 240502 (2007).

[Zha09a] Zhao, B., Chen, Y.-A., Bao, X.-H., Strassel, T., Chuu, C.-S., Jin, X.-M., Schmiedmayer, J., Yuan, Z.-S., Chen, S., Pan, J.-W., *Nat. Phys.*, **5**, 95 (2009).

[Zha09b] Zhao, R., Dudin, Y. O., Jenkins, S. D., Campbell, C. J., Matsukevich, D. N., Kennedy, T. A. B., Kuzmich, A., *Nat. Phys.*, **5**, 100 (2009).